UAB
Universitat Autònoma de Barcelona

Boosting magneto-ionic effects in Co-oxide films by electrolyte-gating

Tesi Doctoral

Sofia Martins
Programa de Doctorat en Ciència de Materials

Directors:
Jordi Sort Viñas
Enric Menéndez Dalmau
Eva Pellicer Vilà

Departament de Física
Facultat de Ciències
2023

UAB
Universitat Autònoma de Barcelona

Memòria presentada per aspirar al Grau de Doctor per
Sofia Martins

Vist i plau

Jordi Sort Viñas
Enric Menéndez Dalmau
Eva Pellicer Vilà

Bellaterra, 16 de Febrer de 2023

UAB

El **Dr. Jordi Sort Viñas**, Professor ICREA del Departament de Física de la Universitat Autònoma de Barcelona,

el **Dr. Enric Menéndez Dalmau**, Professor Lector Serra Húnter del Departament de Física de la Universitat Autònoma de Barcelona,

i la **Dra. Eva Pellicer Vilà**, Professora Agregada del Departament de Física de la Universitat Autònoma de Barcelona,

CERTIFIQUEN:

Que **Sofia Martins** ha realitzat sota la seva direcció el treball d'investigació que s'exposa a la memòria titulada «Boosting magneto-ionic effects in Co-oxide films by electrolyte-gating» per optar al grau de **Doctora per la Universitat Autònoma de Barcelona**.

Que el disseny dels experiments, síntesi de mostres, llur caracterització, l'anàlisi dels resultats, la redacción dels articles i d'aquesta memòria són fruit del treball d'investigació realitzat per Sofia Martins.

I perquè així consti, signen el present certificat,

Jordi Sort   Enric Menéndez   Eva Pellicer

Abstract

This Thesis is aimed at boosting oxygen ion motion and the concomitant magneto-ionic effects in electrolyte-gated paramagnetic cobalt oxide (Co-oxide) films using three different approaches: thickness reduction of the Co-oxide films, variation of electrolyte composition, and defect engineering in the films.

Voltage control of magnetism (VCM) by magneto-ionics is a cutting-edge research topic since it has the potential to enhance the energy efficiency of magnetically actuated systems. Magneto-ionics is a VCM mechanism in which the magnetic properties of a material are toggled by voltage-driven ion motion. However, room temperature oxygen motion has shown to be too slow for relevant applications.

Here we present several approaches to boost oxygen motion by electrolyte-gating. Thickness reduction from > 200 nm down to 5 nm results in sub-10 s ON-OFF transitions in the initially paramagnetic Co-oxide films. By applying voltage pulses, we have shown spike-rate-dependent plasticity, which is a sign of potential learning capabilities.

In a second approach, the addition of salts to propylene carbonate (PC) has been used to increase the strength of the electric double layer built at the Co-oxide / electrolyte interface. For KI-containing PC, a 35-fold increase of the magneto-ionic rate has been observed as compared to

plain PC, under a low voltage of −1.5 V. *Ab initio* molecular dynamics simulations attribute this fast magneto-ionic response to the preferential location of K^+ ions on the Co-oxide surface when using KI (compared to KCl).

Moreover, we have demonstrated the potential of ion implantation to engineer depth-resolved defect density to control the magneto-ionic behavior of Co-oxide films. In terms of rate and amount of generated magnetization, the short-, mid-, and long-term voltage actuation has been controlled by varying the generated collisional damage through ion fluence.

These results turn magneto-ionics into a potential technology for brain inspired hardware for neuromorphic computing.

Resumen

Esta tesis tiene como objetivo mejorar la migración de iones oxígeno y los efectos magneto-iónicos concomitantes en películas de óxido de cobalto paramagnéticas, cuya actuación se lleva a cabo en un electrolito mediante la aplicación de un voltaje externo (puerta). Estas mejoras se han llevado a cabo mediante la reducción del espesor de las capas de óxido de cobalto, la modificación del electrolito y el diseño "a la carta" de los defectos en las capas.

El control del magnetismo mediante voltaje por vía magneto-iónica es un tema de investigación de vanguardia ya que tiene el potencial de mejorar la eficiencia energética de los sistemas actuados magnéticamente. En magneto-iónica se consigue manipular las propiedades magnéticas del material gracias a la migración de iones inducida por voltaje. Sin embargo, la migración de oxígeno a temperatura ambiente ha demostrado ser demasiado lenta para aplicaciones relevantes.

En esta tesis proponemos varias estrategias para favorecer el movimiento de iones oxígeno en capas de óxido de cobalto sumergidas en un electrolito que son actuadas externamente con voltaje. La reducción de su espesor de > 200 nm a 5 nm da como resultado transiciones ON-OFF de duración inferior a 10 s en capas inicialmente

paramagnéticas. Al aplicar pulsos de voltaje, hemos demostrado una plasticidad dependiente de la velocidad pico, lo que constituye un signo de capacidad de aprendizaje.

Como segunda estrategia, se han añadido sales al carbonato de propileno (PC) para aumentar la fuerza de la doble capa eléctrica creada en la interfaz capa de óxido de cobalto / electrolito. En la solución de PC con KI se ha conseguido una velocidad magneto-iónica 35 veces superior a la observada en el electrolito de PC sin sales, bajo un voltaje aplicado de −1.5 V. Las simulaciones de dinámica molecular *ab initio* han permitido atribuir esta rápida respuesta magneto-iónica a la ubicación preferencial de iones K^+ en la superficie del óxido de cobalto cuando se usa KI (en comparación con KCl).

Además, hemos demostrado el potencial que tiene la implantación de iones a la hora de crear un perfil definido de densidad de defectos en profundidad para controlar el comportamiento magneto-iónico de las películas de óxido de cobalto. En términos de velocidad y cantidad de magnetización generada, la activación de voltaje a corto, medio y largo plazo se ha controlado variando el daño por colisión generado a través de la fluencia de iones.

Estos resultados convierten a la magneto-iónica en una tecnología con potencial para ser implementada en hardware inspirado en el funcionamiento del cerebro para computación neuromórfica.

Resum

Aquesta tesi té com a objectiu millorar la migració d'ions oxigen i els efectes magneto-iònics concomitants en pel·lícules d'òxid de cobalt paramagnètiques, l'actuació de les quals es duu a terme en un electròlit mitjançant l'aplicació d'un voltatge extern (porta). Aquestes millores s'han dut a terme mitjançant la reducció del gruix de les capes d'òxid de cobalt, la modificació de l'electròlit i el disseny "a la carta" dels defectes a les capes.

El control del magnetisme mitjançant voltatge per via magneto-iònica és un tema de recerca d'avantguarda, ja que té el potencial de millorar l'eficiència energètica dels sistemes actuats magnèticament. En magneto-iònica s'aconsegueix manipular les propietats magnètiques del material gràcies a la migració d'ions induïda per voltatge. Tot i això, la migració d'oxigen a temperatura ambient ha demostrat ser massa lenta per a aplicacions rellevants.

En aquesta tesi proposem l'ús de diverses estratègies per afavorir el moviment d'ions oxigen en capes d'òxid de cobalt submergides en un electròlit, les quals són actuades externament amb voltatge. La reducció del seu gruix de > 200 nm a 5 nm dona com a resultat transicions ON-OFF de durada inferior a 10 s en capes inicialment paramagnètiques. En aplicar polsos de voltatge, hem demostrat una plasticitat que depèn de

la velocitat pic, cosa que constitueix un signe de capacitat d'aprenentatge.

Com a segona estratègia, s'han afegit sals al carbonat de propilè (PC) per augmentar la força de la doble capa elèctrica creada a la interfície capa d'òxid de cobalt/electròlit. A la solució de PC amb KI s'ha aconseguit una velocitat magneto-iònica 35 vegades superior a l'observada a l'electròlit de PC sense sals, sota un voltatge aplicat de −1.5 V. Les simulacions de dinàmica molecular ab initio han permès atribuir aquesta ràpida resposta magneto-iònica a la ubicació preferencial d'ions K^+ a la superfície de l'òxid de cobalt quan es fa servir KI (en comparació amb KCl).

A més, hem demostrat el potencial que té la implantació d'ions a l'hora de crear un perfil definit de densitat de defectes en profunditat per controlar el comportament magneto-iònic de les pel·lícules d'òxid de cobalt. En termes de velocitat i quantitat de magnetització generada, l'activació de voltatge a curt, mitjà i llarg termini s'ha controlat variant el dany per col·lisió generat a través de la fluència d'ions.

Aquests resultats converteixen la magneto-iònica en una tecnologia amb potencial per ser implementada en maquinari inspirat en el funcionament del cervell per a computació neuromòrfica.

Preface

This thesis is structured in the following chapters:

1 Introduction The fundamentals of magnetism and magnetoelectric phenomena are presented in this chapter. The state-of-the-art of the existing mechanisms to control magnetism by voltage is overviewed. A summary of recent advances and limitations of the magneto-ionic approach is shown as well.

2 Objectives The main objectives of this work are listed in this chapter.

3 Results and Discussion In this chapter, the results derived from this Thesis are gathered under the 'compilation of articles' format, in adherence to the rules of the official UAB PhD programme in Materials Science. The subchapter of control of magneto-ionics by defect engineering through light ion implantation is not published at the time of thesis submission.

4 General Discussion A general discussion of the results obtained throughout this Thesis.

5	**Conclusions**	The most important conclusions of this Thesis are presented.
6	**Future Perspectives**	This chapter outlines the research that could be done in the future as a direct continuation of this Thesis.
7	**Curriculum Vitae**	The *Curriculum Vitae* is included at the end of the dissertation.

Glossary

Ab initio molecular dynamics (AIMD)

Antiferromagnetic material (AFM)

Applied magnetic field ($H_{applied}$)

$BaTiO_3$ (BTO)

$BiFeO_3$ (BFO)

Calcium tetrafluoroborate ($Ca(BF_4)_2$)

$CoFe_2O_4$ (CFO)

Converse magnetoelectric effect (CME)

Composite multiferroics (c-MFs)

Counter Electrode (CE)

Curie temperature (T_C)

Current (I)

Demagnetizing field (H_d)

Dzyaloshinskii-Moriya interaction (DMI)

Diluted magnetic semiconductor (DMS)

Displacement per atom (dpa)

Electric double layer (EDL)

Electric polarization (P)

Ferrimagnetic material (FiM)

Ferroelectric material (FE)

Ferromagnetic material (FM)

Hard disks drives (HDDs)

Information and Communication Technology (ICT)

Internal magnetic field (H)

$La_{1-x}Ca_xMnO_3$ (LCMO)

$La_{1-x}Sr_xMnO_3$ (LSMO)

Magnetic flux density (B)

Magnetic moment (m)

Magnetic susceptibility (χ)

Magnetization (M)

Magnetoelectric (ME)

Magnetoresistive random-access memories (MRAMs)

Magnetostriction coefficient (λ)

Multiferroics (MFs)

Néel temperature (T_N)

$NiFe_2O_4$ (NFO)

$Pb(Mg_{1/3}Nb_{2/3})O_3$–$PbTiO_3$ (PMN–PT)

$Pb(Zr,Ti)O_3$ (PZT)

$Pb(Zn_{1/3}Nb_{2/3})O_3$-$PbTiO_3$ (PZN-PT)

Permeability of free space (μ_0)

Perpendicular magnetic anisotropy (PMA)

Piezoelectric coefficient (d_{ij})

Polyimide (PI)

Polyvinylidene fluoride (PVDF)

Potassium chloride (KCl)

Potassium iodide (KI)

Power dissipated (J)

Propylene carbonate (PC)

Pseudo-reference electrode (Ref)

Remanent magnetization (M_R)

Resistance (R)

Saturation magnetization (M_S)

Single phase multiferroics (s-MFs)

$Tb_xDy_{1-x}Fe_2$ (Terfenol-D)
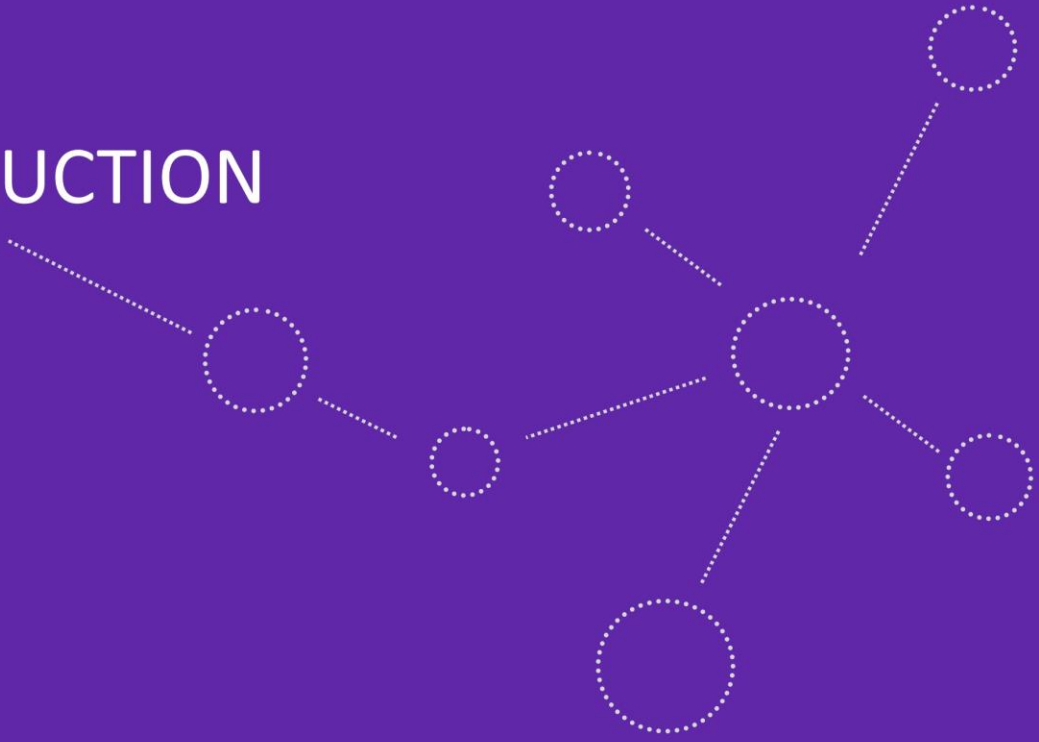
Voltage control of magnetism (VCM)

Working Electrode (WE)

Contents

INTRODUCTION

1.1.   Facing the large energy consumption in magnetic systems

An efficient use of electric power is essential for the Information and Communication Technology (ICT) business to further progress. About 3-5% of the generated energy is wasted in form of heat. Magnetism and spintronics have largely contributed to the digital revolution by dramatically enhancing the hard disk capacity and the data processing speed. Magnetic actuation is also at the heart of many micro/nano-electro-mechanical systems and other engineering applications. However, power consumption in magneto-electronic devices still poses a challenge.[1] Conventionally, localized magnetic fields (generated by electromagnetic induction, Figure 1 a) or spin-polarized electric currents (spin-transfer torque) are used for magnetization switching in devices.[2] However, both principles involve substantial energy loss by Joule effect, since relatively high electric currents are required (Figure 1 b). For example, the currents needed to operate conventional magnetoresistive random-access memories (MRAMs) are of the order of 10 mA, whereas the spin-transfer torque variant of MRAMs requires currents of at least 0.5 mA. This is still a factor five times larger than the output currents delivered by highly miniaturized metal-oxide-semiconductor field-effect transistors.[3]
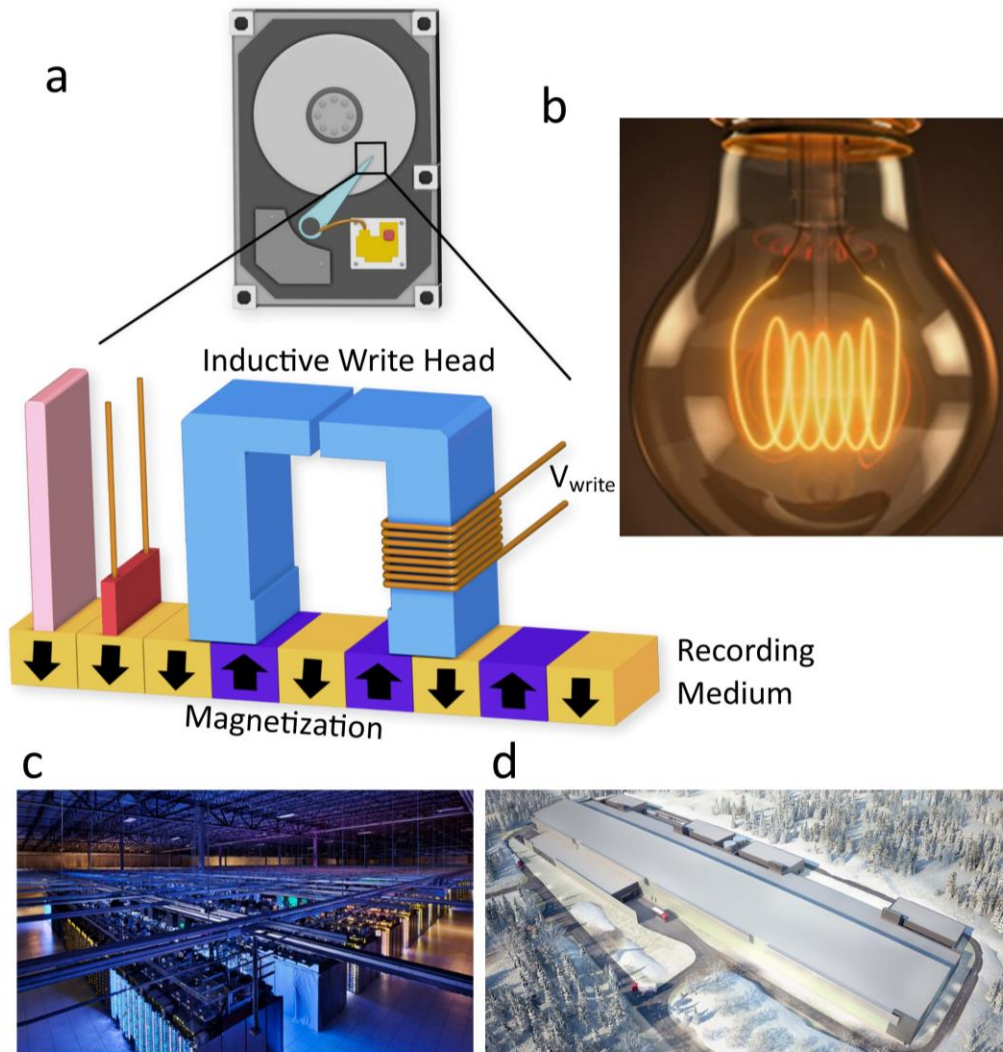
Figure 1: (a) Schematic drawing of the writing process of information in a magnetic media, where bits of different orientation are generated by flowing currents (in one or another direction) in the electromagnet of the writing head of a hard disk. Courtesy of A. Abrantes. (b) shows an in incandescent filament, illustrating the Joule heating effect. (c) Refrigerating system in a Google server. (d) Facebook server located in Sweden (which takes advantage of natural refrigeration).

Around 250 terawatt-hours of electricity were used by data centers throughout the whole world in 2019.[4] These ever-increasing power demands will undoubtedly become a serious issue, not only from an

economic standpoint but also for the environment, as 80% of the world's energy is still produced by fossil fuels.

Additionally, overheating in data servers can affect the memories and result in the loss of recorded data. Data center providers are therefore working hard to come up with solutions to this issue, deploying expensive and sophisticated cooling equipment or placing their servers under the ocean or in cold countries, like Sweden (Figure 1 c and 1 d). In a typical data center, the cooling infrastructure consumes 50% of the energy, followed by servers and storage devices (26%), which are the next major energy consumers.[5]

Use of voltage instead of electric currents for the storing and processing of magnetic data is a promising alternative to lower the power consumption of these devices. The so-called converse magnetoelectric effect (CME) is the name given to relate changes in magnetism in response to externally applied voltages. By exploiting the CME, energy losses due to Joule resistive heating can be greatly reduced.[6] This area is also called voltage control of magnetism (VCM). This is at the core of the thesis presented herein.

1.2.   Fundamentals of Magnetism

In nature, many objects possess a magnetic moment (m) like permanent magnets, elementary particles (*e.g.,* electrons), loops of electric wires (*e.g.,* electromagnets), several molecules, and many astronomical

entities. At the most fundamental level, the magnetic moment arises from the intrinsic spin motion and the orbital movement of the electrons around the nucleus of the atoms.[7] In the presence of an applied external magnetic field ($H_{applied}$), the materials can suffer a reorganization/reorientation of electrons' spin, inducing a response called magnetic induction or magnetic flux density (B) calculated from Ampere's law or Biot-Savart Law. The following equations holds (Eq. 1.1):

$$B = \mu_0 H_{applied} \qquad (1.1)$$

where $\mu_0 = 4\pi \times 10^{-7} N\ A^{-2}$ (SI units) $or\ \mu_0 = 1$ (cgs units) is the permeability of free space, and $H_{applied}$ the applied magnetic field strength.

When vacuum is replaced by a material or, in other words, when the generated fields pass through magnetic materials which themselves contribute with internal magnetic fields, Eq. 1.1 is written as:

$$B = \mu_0(H + M) \ \text{(SI units)} \qquad (1.2)$$

$$B = H + 4\pi M \quad \text{(csg units)} \qquad (1.3)$$

or

$$B = \mu_m M \ \text{(SI units)} \qquad (1.4)$$

where μ_m is the permeability of the material and relates to that of the free space through the so-called relative permeability, μ_r (Eq. 1.5):

$$\mu_r = \frac{\mu_m}{\mu_0} \tag{1.5}$$

To avoid misunderstandings in the designation of *H* and *B*, the former is typically referred to as magnetic field, and *B* is called magnetic flux density or magnetic induction. If the material does not respond to an external magnetic field by producing any magnetization, then μ_r = 1. The magnetization of the material (*M*) is defined as the sum of magnetic moments divided by volume. While in the free space *M*=0 obviously,[7] in the presence of a magnetic material *B* and *H* can change in magnitude and direction due to the *M*.

Strictly speaking, *H* is the sum of the $H_{applied}$ and the demagnetizing field (*Hd*) produced by magnetization redistribution of the sample itself, which is dependent on the shape of the specimen.[7,8]

$$H = H_{applied} + H_d \tag{1.6}$$

The magnetic characterization of materials involves studying how *M* varies with *H*. The ratio between these quantities is the susceptibility (*χ*):

$$\chi = \frac{M}{H} \tag{1.7}$$

χ indicates how easy it is to magnetize a material. In general, permeability and susceptibility are tensors because they relate two vector quantities that do no need to be parallel:

$$\mu_r = 1 + \chi \qquad (1.8)$$

According to the magnitude and sign of χ and μ_r, materials are classified into five groups: [9]

- **Diamagnetic:** χ is small and negative, and μ_r is slightly less than 1.

- **Paramagnetic/ antiferromagnetic:** χ is small and positive, and μ_r is slightly greater than 1.

- **Ferromagnetic/ ferrimagnetic:** χ and μ_r are large and positive.

Diamagnetic materials have no net magnetic moment without the presence of an $H_{applied}$. However, under an $H_{applied}$, the spin of electrons experiences a motion (Larmor precession), generating a tiny magnetic moment in the opposite direction of $H_{applied}$ (Figure 2 a). Diamagnetism arises from bounded electrons and is present in all materials. It opposes to $H_{applied}$, but it is very weak compared with other magnetic effects. The susceptibility of diamagnetic materials is independent of temperature.

In the case of **ferromagnetic** (FM) **materials**, the exchange interaction between the atomic moments is positive and extends over a long-range order even without $H_{applied}$. Upon $H_{applied}$, the magnetic moments tend

to align along this field (Figure 2 a). Due to this strong and positive interaction between spins, the alignment is retained when the magnetic field is removed, showing a hysteresis loop behavior. Many relevant quantities of a ferromagnetic material can be obtained by studying its hysteresis loop (Figure 2 c). The following parameters can be extracted from hysteresis loops:
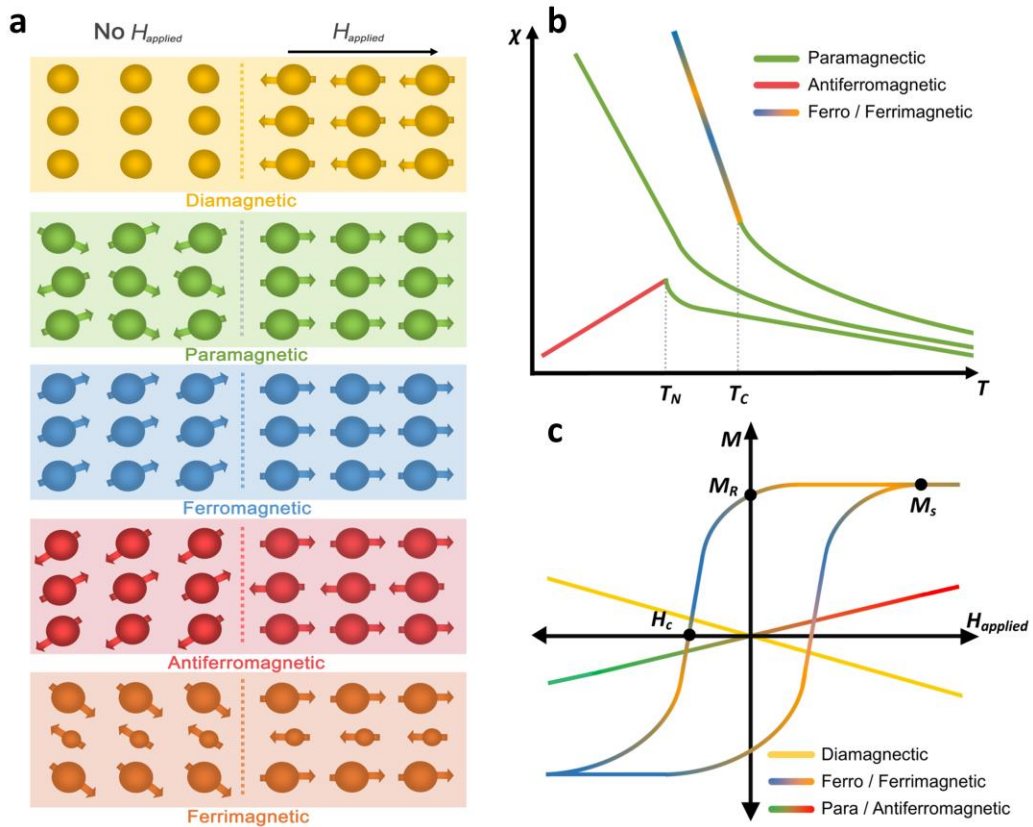
Figure 2: (a) Schematic illustration of the magnetic moment arrangement in different magnetic materials against an $H_{applied}$. (b) Susceptibility temperature dependence for paramagnetic, antiferromagnetic and ferro/ferrimagnetic materials (c) Slopes of M versus $H_{applied}$ in different magnetic materials, and magnetic parameters points such as M_S, M_R and H_C in a typical hysteresis loop of a ferro/ferrimagnetic material. Courtesy of M. Rahmann.

Saturation magnetization (M_S): Value of magnetization beyond the point where all magnetic moments are aligned along $H_{applied}$ and the material reaches the maximum M.

Remanent magnetization (M_R): residual magnetization left behind in a FM material after $H_{applied}$ is removed.

Coercivity (H_C): the applied magnetic field necessary to suppress the net remaining magnetization. Soft magnetic materials are characterized by low energy to suppress the remanent magnetization (low H_C), as opposed to hard magnetic materials (high H_C). The spontaneous magnetization of a ferromagnet vanishes above the Curie temperature (T_C) where the spins in FM materials become disordered, in a paramagnetic state (Figure 2 b).

Antiferromagnetic (AFM) **materials** comprise a crystal lattice subdivided into two or more sublattices arranged in an antiparallel manner, providing a total zero net moment in the absence of $H_{applied}$ (Figure 2 a). In this case the exchange interaction is negative. The magnetic dependence with $H_{applied}$ is positive and linear, as for a paramagnetic material (Figure 2 c). The antiferromagnetic transition to paramagnetic state happens at the Néel Temperature (T_N) which is marked by a small peak in χ (Figure 2 b).

Ferrimagnetic (FiM) **materials** are like antiferromagnets, presenting sublattices aligned in antiparallel fashion but in this case with dissimilar

strengths, (Figure 2 a) thereby providing a macroscopic behavior similar to ferromagnetic materials upon $H_{applied}$, showing a hysteresis loop (Figure 2 c).

Finally, **paramagnetic materials** show magnetic moments randomly oriented in the absence of $H_{applied}$, due to thermal agitation prevailing over exchange interactions between the spins. Once under $H_{applied}$, spins tend to align with it, resulting in a positive and linear slope of M as a function of $H_{applied}$ (Figure 2 a). As $H_{applied}$ is removed, no retention of net magnetic moment is observed.

1.3.   Magnetoelectric phenomena

Electricity and magnetism are closely related. In 1960, Astrov[10] showed the first experimental results of the linear correlation between electric and magnetic fields in certain materials, proving the magnetoelectric phenomena conjectured by Curie[11] already in 1894. The term "magnetoelectric effect" (ME) was coined by P. Debye[12] in 1926 and it refers to the appearance of magnetization due to an externally applied electric field (CME) or the induction of electric polarization under an externally applied magnetic field (direct magnetoelectric effect).[13]

The industry of electrical devices has taken a big effort to develop smaller and faster memories. Magnetic storage in computer hard disks drives (HDDs) and magnetoresistive random-access memories (MRAMs) are still mainly using electric currents to encode information.

However, the heat generated is an unavoidable energy loss limiting the density of devices, and consequently the performance of chips. This problem can be explained by the Joule's law (eq. 1.9), which indicates that heat is generated by passing an electrical current through a conductor:

$$J = IV = I^2 R \qquad (1.9)$$

Where J is the power (energy per time) converted from electrical to thermal energy, I the current travelling through the conductor, V is the voltage drop across the conductor, and R the resistance of the conductor.

In parallel to the development of current-based magnetically controlled systems with better energy efficiency, alternative strategies are being studied to produce even more efficient magnetic devices. VCM has a great potential to give rise to ultra-low power devices by completely suppressing the use of electric currents. Concisely, VCM is based on the replacement of electric currents by electric fields.

By definition, the **direct ME effect** takes place when an electric polarization P is induced as a result of $H_{applied}$ in accordance with:

$$\Delta P = \alpha_D \Delta H_{applied} \qquad (1.10)$$

where α_D is the direct ME coupling coefficient. The **converse ME effect** is realized when a magnetization M is generated in response to an electric field E:

$$\Delta M = \alpha_C \Delta E_{applied} \tag{1.11}$$

where α_C represents the converse ME coupling coefficient.[14]

1.4.   Device configurations for electric field application. Electrolyte-gated magnetoelectric actuation

Two main device configurations can be adopted to modulate the magnetic properties of a FM material under voltage actuation. The first one is the **field effect transistor (FET) configuration**, which consists of three electrodes (source, drain and gate), in which changes in magnetic properties are frequently assessed through changes in (magneto)resistance measured by Hall effect (Figure 3 a). In this case,
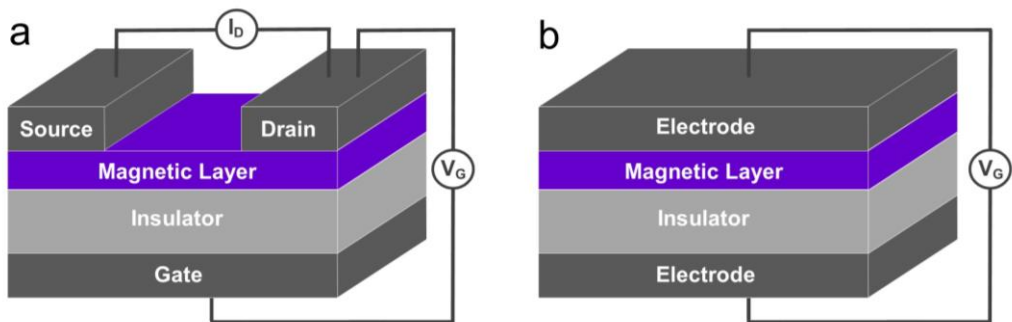
Figure 3: Device configurations for VCM: (a) field-effect transistor and (b) capacitor.

the gate voltage is responsible for the change in the magnetic properties of the magnetic layer. Tracking of the magnetic changes is realized through the current flow from source to drain. The **capacitor configuration** is another very convenient geometry (Figure 3 b). In this scenario, one of the electrodes is the FM material and the counter-electrode is grown on the other side, separated by an insulating layer.

The electric field strength required to change a material's magnetic properties is typically between 0.01 V/Å and 5 V/Å. Unless the electrical insulator layers are made very thin, quite high voltages (sometimes in the range of tens or hundreds of V) must be applied to produce these fields, which is not particularly useful for practical applications. The production of solid-state devices with high-quality ultra-thin dielectric layers (*e.g.*, 1-2 nm thick Al_2O_3, SiO_2, HfO_2, or MgO) is still a challenge, despite recent advancements in deposition techniques like sputtering, molecular beam epitaxy, or atomic layer deposition. This is because structural defects easily result in pinholes and consequent leakage of the accumulated electric charges. Numerous strategies have been developed to overcome this issue: (i) using insulating polymers (*e.g.* polyimide (PI) and polyvinyl difluoride (PVDF); however, it is difficult to make these polymers particularly thin by spin coating, and (ii) implement liquid electrolytes, such as polar aprotic organic solvents (*e.g.* propylene carbonate (PC)), ion liquids (*e.g.* 1-ethyl-3-methylimidazolium bis(trifluoromethylsulfonyl)imide (EMIM- TFSI)), or aqueous electrolytes (with dissolved KOH or NaOH).

In the last years, intensive research on electrolyte-gating (*i.e.* liquid-gating) has proven to be a convenient means to avoid the application of high voltages, as often required in solid-state devices. By taking advantage of liquid electrolytes, low or moderate voltages can produce reasonable strong electric fields of the order of hundreds of MV/cm, as a result of the formation of extremely thin electric double layers (EDLs).

1.5.   Mechanisms under voltage control of magnetism

There are different mechanisms to accomplish the CME effect. These rely on the use of distinct materials and/or ways of exploiting the related phenomena behind: multiferroics, strain-mediated coupling in piezoelectric/magnetostrictive heterostructures, charge carrier doping,
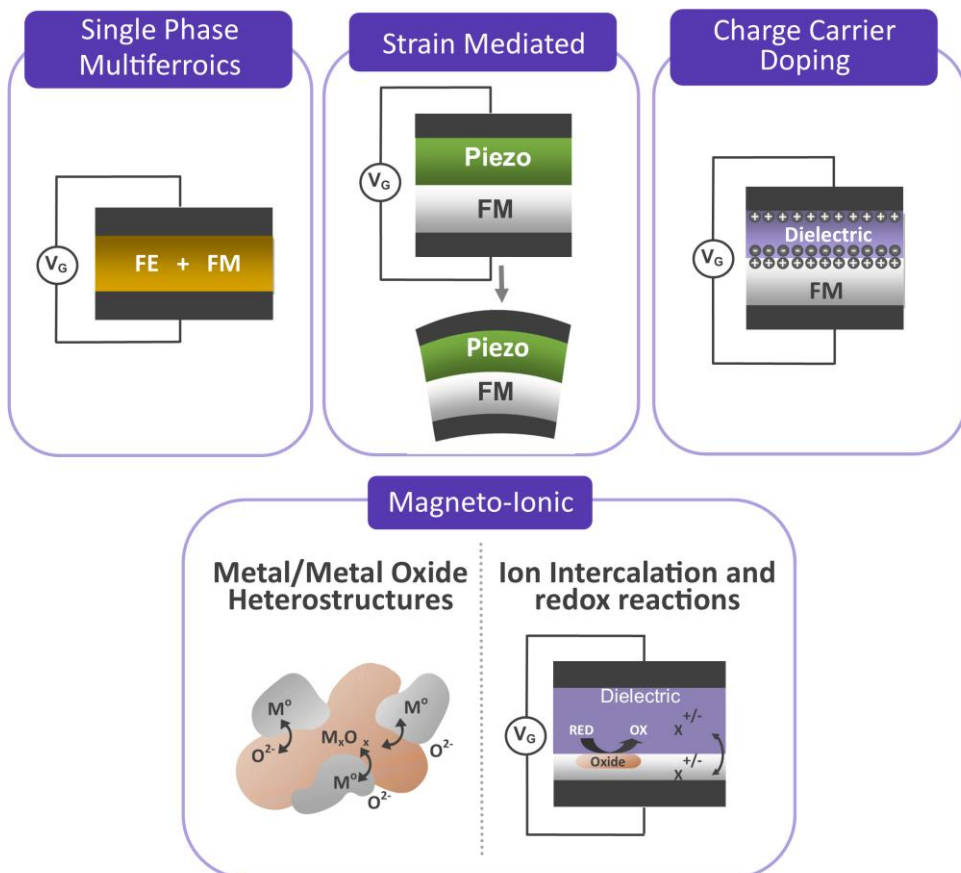
Figure 4 Main mechanisms of ME effect. Schematics illustrating the underlying physical/physicochemical concepts for each mechanism.

and magneto-ionics (Figure 4). The basics of each approach are overviewed in the following subsections.

1.5.1. Multiferroic materials

Multiferroics (MFs), first coined by Schmid in 1994, are one of the most appealing materials for VCM devices. These are a big class of materials which exhibit more than one ferroic ordering – (anti)ferromagnetism, ferroelectricity and/or ferroelasticity.[15] In the case of the subgroup of MFs considered as ME materials (ME MFs), these display ferromagnetism and ferroelectricity orders coexisting and influencing each other through a ME coupling effect. ME MFs can be broadly divided into two categories: single phase (s-MFs) and composite (or biphasic) multiferroics (c-MFs). s-MFs can be classified as type I, with different transition temperatures for each phase, or type II with similar transition temperatures.

Cr_2O_3 was the first experimentally ME coupling material observed below its T_N transition.[16,17] However, this material presents antiferromagnet and paraelectric coupling (*i.e.*, it is not MF), and it does not meet the requirements to be used in microelectronic applications. After the discovery of Cr_2O_3, many different MF materials were explored, such as $BiFeO_3$ (BFO)[18] and $TbMnO_3$[19], which are s-MFs manifesting an intrinsic ME coupling between FM/FE orders.

Despite the potential of s-MFs as ideal candidates in VCM systems, the scarcity of s-MFs and their low coupling coefficient at room temperature, prompted the scientific community to explore other materials and mechanisms. Composite multiferroics emerged as an alternative to overcome the fundamental problems of s-MFs. c-MFs are artificially produced by combining FM and FE materials assembled in granular or layered arrangements. In theory, the coupling in c-MFs can be 10^8 times larger than for s-MFs.[20] Intrinsic coupling is achieved in s-MFs by direct interaction between electric field and magnetization. In contrast, for c-MFs, a ME coupling occurs extrinsically by any of the three following mechanisms: strain, charge carrier or spin exchange. The approach of cross-coupled ME interaction in c-MFs depends upon microstructure and quality of the interface between phases.

1.5.2.   ME coupling via strain

Strain-mediated ME coupling mechanism has been the most successfully used mechanism to produce strong ME coupling at room temperature. In composites, this mechanism arises from the elastic coupling between magnetostrictive and piezoelectric (or ferroelectric) phases. A direct ME effect can be observed by applying a magnetic field to a c-MF material, which will induce strain in the magnetic phase through the magnetostrictive effect. This strain will be transferred to the piezoelectric phase giving rise to an electrical displacement caused by piezoelectric effect. A converse ME effect also exists when an electric

field is applied to the FE phase, thereby generating strain which is transferred to the FM adjacent material, inducing changes in its magnetic properties thanks to the inverse magnetostriction effect (Villari effect).[7,21]

A significant ME effect by the strain mediated mechanism requires large piezoelectric coefficient (d_{ii}) from the FE phase and large magnetostriction coefficient (λ) from the FM phase. The most suitable piezoelectric materials used in the fabrication of composite ME materials are ceramic oxide $Pb(Zr,Ti)O_3$-based compositions (PZT), because of the good combination between their d_{33} and the electromechanical coupling coefficient (k_{33}). The k_{33} is related to the conversion rate between electrical energy and mechanical energy. $Pb(Zn_{1/3}Nb_{2/3})O_3$-$PbTiO_3$ (PZN-PT) and $Pb(Mg_{1/3}Nb_{2/3})O_3$–$PbTiO_3$ (PMN–PT) exhibit even better k_{33}, but lower T_c and inferior mechanical properties. PVDF is another piezoelectric candidate offering some advantages in terms of elastic constant but presents a low melting point. With respect to the FM phase, ferrites are commonly used but metallic alloys are the most promising magnetostrictive materials. $Tb_xDy_{1-x}Fe_2$ (Terfenol-D) exhibits the highest λ of any known material but it is rather fragile and costly. [20]

The ME response in c-MFs depends also on the chemical compatibility, elastic coupling, phase compatibility and interfacial bonding between phases. Indeed, c-MFs can have a variety of connectivity schemes,

through a choice of shape, phase properties, volume fraction, but the most common are: (1) the **0-3 type** of connectivity scheme, in which FM particles are embedded on a FE matrix; (2) **2-2 type**, where laminates of FM material alternate with laminates of FE; and (3) **1-3 type**: FM fibers are embedded on a FE matrix. (Figure 5)

A pioneering work of strain-mediated ME coupling between $CoFe_2O_4$: $BaTiO_3$ (CFO:BTO) was carried out in 1972.[22] Many attempts were done to isolate the ferrite phase to reduce leakage currents, and thanks to the synthesis of core-shell CFO:BFO nanocomposites it was possible to enhance α_C (35 times higher) compared to their bulk counterparts. [23] The highest $\alpha_C \sim 195$ mV cm^{-1} Oe^{-1} was observed in core-shell particles having a PZT core and a $NiFe_2O_4$ (NFO) shell surface.[24]

In the last decades, several other c-MFs **oxide heterostructures** have been investigated: PZT:$La_{1-x}Sr_xMnO_3$ (LSMO),[25] PMN-PT:$La_{1-x}Ca_xMnO_3$ (LCMO)[26,27], PMN-PT:LSMO[28] and Fe_3O_4:BTO[29]. Moreover, systems
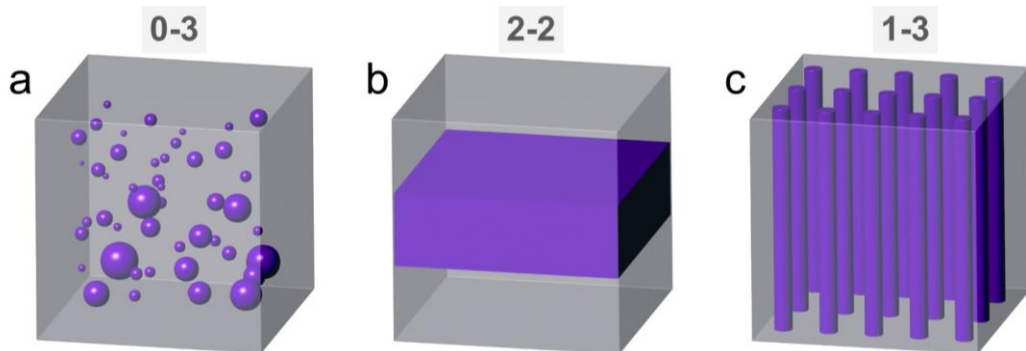
Figure 5: Schematic illustration for different connectivity types of two-phase c-MFs. (a) 0-3 type structure, (b) 2-2 type laminate structure, (c) 1-3 type. Courtesy of André A.

combining FM **metal films** (Fe:BTO)[30–32], **alloys** (FeGaB:PZN-PT,[33] CoPd:PZT,[34] PZT:Fe$_{0.5}$Co$_{0.5}$[35], PZT/Terfenol-D[36]) and **multilayers** of Ni:BTO[37], Cu/Ni multilayers:BTO[38], Co$_{40}$Fe$_{40}$B$_{20}$/Co/Pd:PMN-PT)[39] have been tackeld.

1.5.3. ME coupling via charge carrier doping

In the charge carrier doping mechanism, the application of an external voltage ΔV between electrodes can induce electrostatic doping in the FM/dielectric interface, caused by the accumulation of charge carriers at the interface. The change of electrons (or holes) density in ferromagnets alters not only their electronic properties, but also their intrinsic magnetic properties.[40,41] In semiconductors, electric charges may provide the possibility to modify the magnetic behavior of these materials through controlled and reversible changes in the carrier concentration. Pioneering studies in diluted magnetic semiconductors (DMS) succeeded to switch a thin film of (In,Mn)As from ferromagnetic to paramagnetic state by applying an electric field. This magnetic change was possible through T_C modulation by hole-induced ferromagnetism[42]. Later, the same group demonstrated the magnetization reversal in a ferromagnetic semiconductor film with similar composition by manipulating H_C via modifying carrier density through voltage actuation.[43] Following the same idea, other DMS

systems (($(Ga, Mn)As^{44}$, $Mn_{0.05}Ge_{0.95}$,[45] and (In, Fe)Sb[46]) also showed control of magnetic properties by charge voltage actuation. Despite the remarkable results, only Yamada *et al.* could demonstrate the manipulation of magnetic properties by charge carrier doping through electron mediated of DMS (Co-doped TiO_2) with T_C close to room temperature. [47]

Different from DMS, magnetic transition metals (*e.g.* Co, Fe, Ni) and metallic alloys (e.g. Fe-Pt, Fe-Pd, Co-Pd and Co-Pt) present a higher T_C temperature, but feature a strong electric field screening effect, with a screening length of a few unit cells. [48] The first observations of VCM in thin film metals were reported in 2007 when Weisheit *et al.* [49] could alter the H_C in -4.4% and +1% for FePt and FePd, respectively, by charge carrier doping. Changes of up to 40% of magnetic anisotropy energy (MAE) were reported by Maruyama *et al.*[50] in about four monolayers of Fe. Larger effects were observed by our group in electrolyte-gated nanoporous magnetic alloys (Ni-Cu, Co-Pt).[51,52]

1.5.4.   ME coupling via magneto-ionics

Contrary to charge carrier doping which is primarily a surface effect, magneto-ionics is a mechanism based on voltage-driven transport of ions which can modulate magnetic properties beyond the surface, reaching the bulk of materials. The evolution of VCM and some important milestones are presented in Figure 6,[53] where magneto-ionics
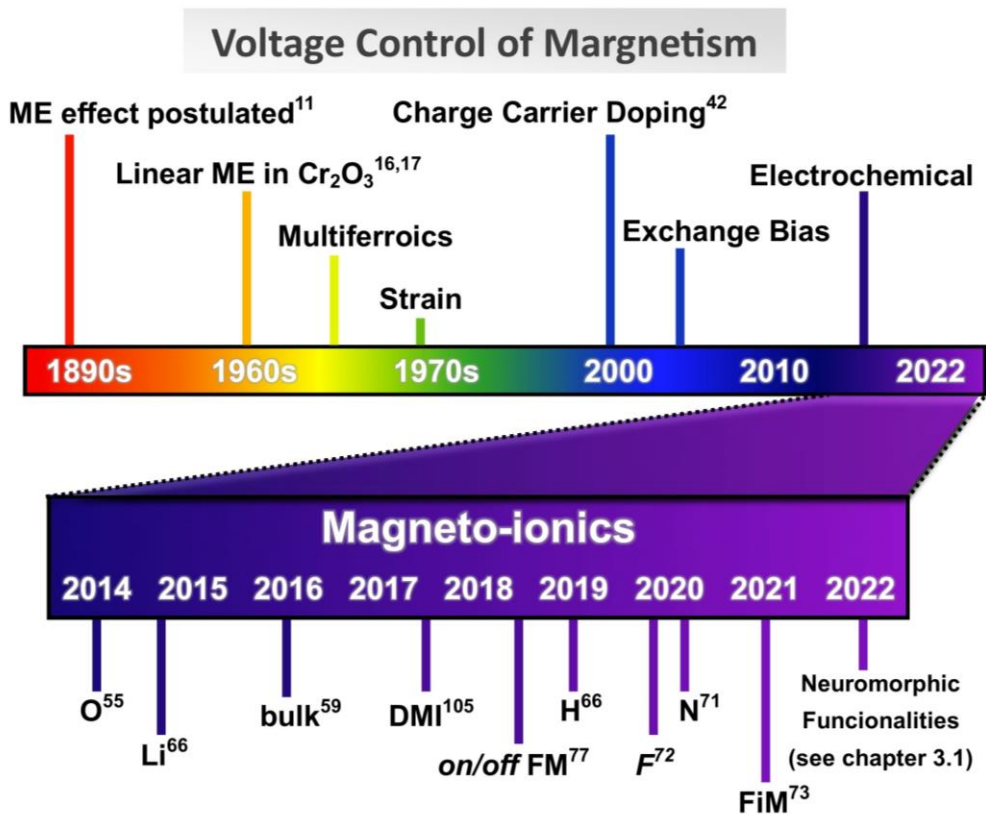
Figure 6: Representative milestones in VCM and recent advances in magneto-ionics. Adapted from Appl. Phys. Lett. 2022, 120, 070501.

only emerged in the last decade. It should be noted that a diversity of materials/electrolytes systems have been studied so far, and that magneto-ionics has received different denominations and categorizations, such as ion intercalation/exchange, redox-based, or electrochemical reactions. This mechanism has generated a flurry of research activities in the last years, based on the idea of mimicking the behavior of electrochemical batteries or fuel cells.
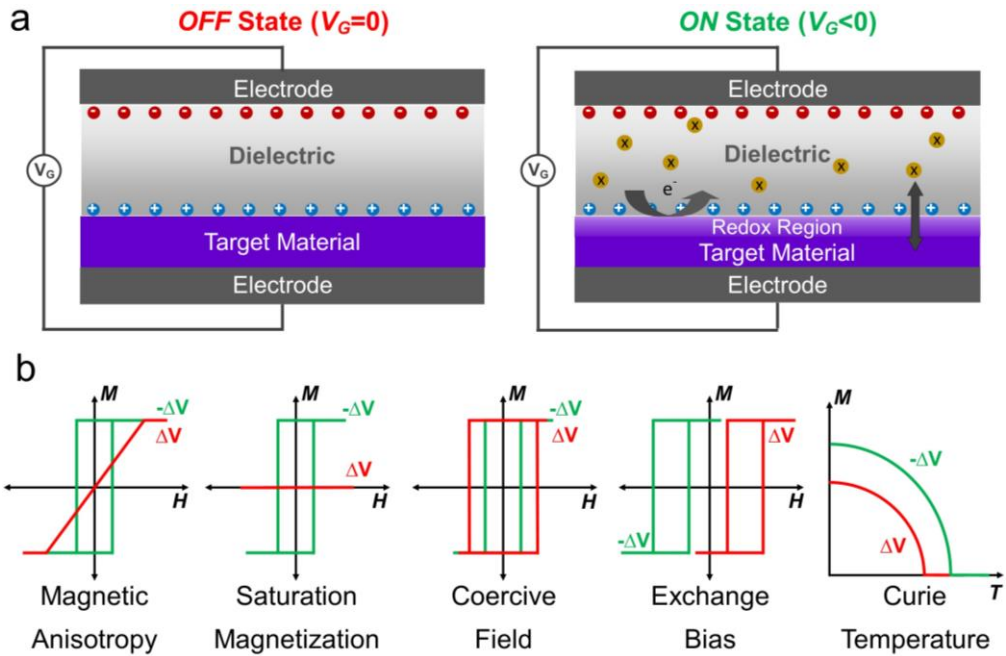
Figure 7: (a) Schematics of magneto-ionic phenomenon in capacitor-like configuration, with the gate voltage V_G setting ON/OFF the magnetic state via redox and ion diffusion. (b) Example of magnetic properties that can be controlled by voltage actuation in magneto-ionic systems.

Magneto-ionics refers to the voltage-driven ion motion across a target material in contact with a solid or liquid electrolyte. By the application of an external electric field, ions are inserted or removed from a target material, undergoing changes in oxidation state, crystalline structure, and stoichiometry, and consequently changes in magnetic properties, such as magnetic anisotropy, coercive field, saturation magnetization, exchange bias, and Curie temperature (Figure 7). Since chemical changes are involved in magneto-ionics, no voltage is required to maintain a set state (*i.e.,* non-volatile effect) and a reversible manipulation of magnetic properties is possible upon applying

electrical voltage of opposite polarity. The main advantage of magneto-ionics, in contrast with other ME mechanisms, is that it can operate at room temperature and at relatively low voltages.

Magneto-ionic effects were first successfully demonstrated in metal/metal-oxide heterostructures by oxygen motion to tailor the oxidation state of the atoms in the magnetic material. Metal oxides with large mobility of oxygen ions have been used as solid state oxygen reservoirs (*e.g.* GdO_x[54,55] or HfO_x[56–58]) in combination with different magnetic metals (*e.g.*, Fe, Co or Ni).

Bauer *et al.*[54] was the first at employing the term "magneto-ionic control" to describe the voltage-induced oxygen migration in a Co/GdO_x bilayer. In this work, the ionic transport was used to modulate the easy axis of magnetization from out-of-plane to in-plane by changing the interfacial oxidation state in a few monolayers of Co. Bi *et al.*[55] and Gilbert *et al.*[59] obtained similar results tuning the perpendicular magnetic anisotropy (PMA) in Co/GdO_x and $Co/AlO_x/GdO_x$ heterostructures, respectively. The modulation of PMA is often requested for applications, since it allows a larger magnetic density packing (*i.e.* enhanced density of information in magnetic memories). HfO_2 proved to be another good candidate as ion reservoir to donate and receive oxygen in magneto-ionic systems. In the works of Yan *et al.*[56] and Zhou *et al.*[57], PMA, T_C, H_C, M_S and exchange bias were

modulated via oxygen migration in Co/Ni/HfO$_2$ films gated by an ionic liquid.

Apart from oxygen, alternative mobile ions have shown successful performance in magneto-ionics, such as hydrogen,[60–63] lithium,[64–68] nitrogen[69–71] and fluorine[72].

1.6.   Recent advances in magneto-ionic research

In recent years, significant advances in magneto-ionics have been reported, especially regarding room temperature operation, switching speed, and reversibility. Tan *et al.*[61,62] demonstrated the powerful role that hydrogen (H) plays in modifying the oxidation state of Co under voltage actuation, and demonstrated that the introduction of H from environmental humidity into the interface of Co/GdO$_x$ stacks accelerated the rate of nondestructive switching of magnetic anisotropy. Meanwhile, Huang *et al.*[73] controlled the ferrimagnetic order of GdCo and switching of magnetic order through hydrogen gating. Yi *et al.*[74] showed reversible and non-volatile control of phase transition in digital complex oxides by voltage-driven dual-ion transfer (both oxygen and hydrogen were moved). Navarro *et al.*[52,75] and Robbennolt *et al.*[76,77] reported dramatic changes in magnetic properties by oxygen-ion voltage actuation of nanoporous, mesoporous and nanostructured materials with high surface-to-volume ratios,

suggesting that the high surface area promotes enhanced magneto-ionics at the interface of heterostructures through redox reactions. These results motivated the study of ferromagnetic metallic thin films, such as Co as target material. However, ultra-thin metal films below 5 nm can become superparamagnetic. Moreover, heat assistance is often needed to aid oxygen motion, [54,59,61,62,78] reducing the energy efficiency of the system. Despite these issues, magneto-ionics beyond the interface of metal films has been also explored. In particular, ion migration from the inner parts of the films can occur along grain boundaries and vacancies, leading to irreversible structural or compositional changes, which unavoidably lead to irreversible redox reactions at the interface.[59,79–81] One possibility is to use the migrating ions in Fe/FeO$_x$[82,83] and Co/CoO$_x$ structures, as examples of metal/oxide heterostructures in thin film and island configurations, allowing the reversible extraction and introduction of oxygen to toggle magnetic states. In iron-based hybrid transition metal oxide/metal,[75,84,85] and porous structures,[86] ON-OFF switching of magnetism has been observed, as well as in cobalt-based single metal layer oxide[87] and nitride[70] films. All these systems possess the migrating anions in the as-deposited state and can create a crystal structure with more local vacancies and wider ionic channels which allow ions to enter and leave the target material with low resistance, often at room temperature.

Specifically, Quintana et al.[88] and Rojas et al.[89] electrolyte-gated 100 nm-thick Co$_3$O$_4$ films with propylene carbonate (PC) with solvated Na$^+$

and OH$^-$ ions at ppm level, and demonstrated non-volatile ON-OFF control of ferromagnetism at room temperate. Paramagnetic as-grown Co_3O_4 films presented a ferromagnetic response (ON) after biasing under -10V for 60 min and became paramagnetic again (OFF) by subsequently applying a bias of +20 V for 60 min. Additionally, M_S increased with the increasing voltage. A sequence of biases (-10, -25, and -50 V) showed an increase of voltage-driven ion motion and further reduction of Co_3O_4 to metallic Co phase, with the possibility to switch the magnetic state in 10^2 s without thermal assistance. Under high voltage actuation (-200 V) the magneto-ionic effect deepened into the film by introducing compositional and structural defects in the entire layer thickness, promoting oxygen intercalation through O-rich diffusion channels. To further understand the effect of the gating configuration, identical films of Co_3O_4 were biased in transistor-like and condenser-like configuration.[89] COMSOL simulations showed a sharp difference in voltage distribution along the films between both configurations while biased, and the magneto-ionic effect was the highest (6 times larger) when the electric field was applied using the capacitor configuration with an underlying conducting buffer layer. The magneto-ionic rate improved 36 times (from 9 to 325 memu cm^{-3} s^{-1}), demonstrating that the magneto-ionic performance of structural ion films is largely affected by the biasing configuration.

1.7.   Limitations of magneto-ionics in oxygen-based systems

Magneto-ionic systems relying on oxygen motion are far to be competitive with existing magnetic memories. Important limitations have been detected: (i) low magneto-ionic rate; (ii) too large applied electric field; (iii) low cyclability. To achieve speeds of 1 ms or faster in magneto-ionic switching, further work needs to be done. For example, the microstructure could be further tuned through defect engineering using ion irradiation[90] and/or miniaturization through micro/nanofabrication in order to favor surface diffusion over bulk diffusion because the latter results in faster ion mobility. Additionally, the nature of the dielectric layer utilized to bias the films should be taken into consideration to broaden technical applications, since in previous works high applied voltages, of the order of −50 V, were necessary to induce a notable change in the magnetic characteristics of cobalt oxide.[89]

Advanced magneto-ionic materials have exhibited good repeatability (*i.e.*, durability) over 1000 cycles[62,91], whereas systems relying on oxygen motion, including structural ions, have shown 50 cycles or fewer. This is partially explained by the deformation or modifications brought about when ionic motion is induced outside of the interface, and it may indicate that three-dimensional, high surface-to-volume ratio designs

that accumulate lots of interfacial defects could be a more feasible choice.

## 1.8. Applications of magneto-ionics. Neuromorphic Computing

It has already been proven that magneto-ionic systems can be used in several applications. Magneto-ionic materials are interesting candidates to be used in neuromorphic or stochastic computing, magnetic random-access memory, domain-wall computing, and lab-on-a-chip devices.[92–94] They may require low energy to actuate ($\approx$10 aJ/bit)[95,96] than conventional current-using methods ($\approx$10 fJ/bit),[97] no voltage to maintain a set state (non-volatile), and they offer the possibility of functional plasticity (*i.e.,* the ability to undergo non-volatile changes in its structure and properties in response to an external stimulus). Microelectromechanical systems rely heavily on magnetic actuation,[98–101] and magneto-ionics may be useful in creating materials that can serve several purposes for robotics. In typical structures for MRAM,[50,102] as well as in Pt/Co(Fe)/MgO, Ta/CoFeB/MgO, and Pt/Co/Ni/HfO$_2$ stacks[56,103,104] the use of ionic transport to control magnetic properties has already been noted. This mechanism is expected to enable low-power tunability of the switching elements via the insulating tunnel barrier. The Dzyaloshinskii-Moriya interaction (DMI), which has been demonstrated to be tunable via magneto-ionics,[60,79,105] stabilizes spin

spirals such as skyrmions,[106,107] chiral domain walls,[108,109] and may have applicability in spin-orbitronics.

1.9.   Magneto-ionic system under study

Voltage-driven oxygen motion through a paramagnetic film of Co-oxide in capacitor configuration was optimized along this thesis. Our magneto-ionic system is a home-made electrolyte cell composed of a buffer layer of titanium (Ti) and copper (Cu) used as working electrode (WE), with a Co-oxide layer deposited on top of the Cu, and a platinum (Pt) wire as counter electrode (CE) immersed in a liquid electrolyte (see Figure 8). For some studies, a second Pt wire was implemented as a pseudo-reference electrode (Ref) to decrease the voltage drop across the system.

a   b
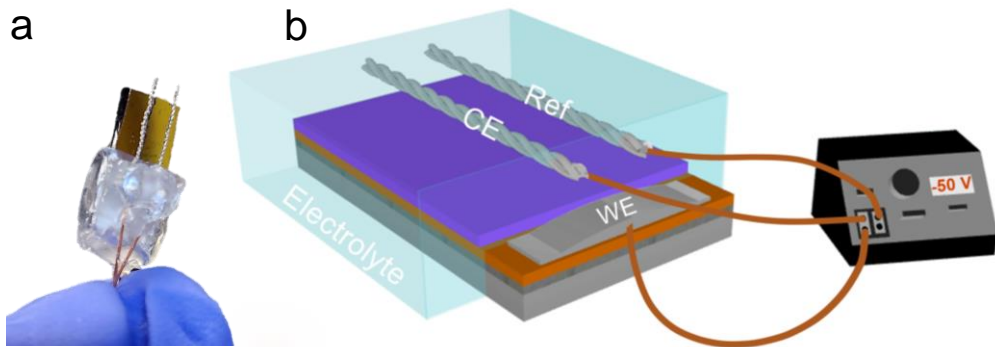
Figure 8: (a) Picture of the sample with contacts prepared for magneto-ionic experiments. (b) Schematic of electrolyte-gate process under voltage actuation.

Bibliography

1.   Hu, J. M., Li, Z., Chen, L. Q. & Nan, C. W. High-density magnetoresistive random access memory operating at ultralow voltage at room temperature. *Nat. Commun.* **2**, 553 (2011).

2.   Urazhdin, S. *et al.* Nanomagnonic devices based on the spin-transfer torque. *Nat. Nanotechnol.* **9**, 509–513 (2014).

3.   Dieny, B. *et al.* Spin-transfer effect and its use in spintronic components. *Int. J. Nanotechnol.* **7**, 591–614 (2010).

4.   Jones, N. How to stop data centres from gobbling up the world's electricity. *Nature* **561**, 163–166 (2018).

5.   Dayarathna, M., Wen, Y. & Fan, R. Data center energy consumption modeling: A survey. *IEEE Commun. Surv. Tutorials* **18**, 732–794 (2016).

6.   Shiota, Y. *et al.* Induction of coherent magnetization switching in a few atomic layers of FeCo using voltage pulses. *Nat. Mater.* **11**, NMAT3172 (2012).

7.   Coey, J. M. D. Magnetism and magnetic materials. Cambridge University Press (2009).

8.   Soshin Chikazumi. *Physics of Ferromagnetism*. (1997).

9.   Cullity, B. D. & Graham, C. D. Introduction to Magnetic Materials. John Wiley & Sons, inc. (2009).

10.   Astrov, D. N. The Magnetoelectric effect in antiferromagnets. *Sov. Phyics JETP* **11**, 708–709 (1960).

11.   Curie, P. Sur la symétrie dans les phénomènes physiques , symétrie d ' un champ électrique et d ' un champ magnétique. *J. Phys. Theor. Appl.* **3**, 393–415 (1894).

12.   Debye, P. Bemerkung zu einigen neuen Versuchen über einen magneto-elektrischen Richteffekt. *Zeitschrift für Phys.* **36**, 300–301 (1926).

13.   Rado, G. T. & Folen, V. J. Magnetoelectric effects in antiferromagnetics. *J. Appl. Phys.* **33**, 1126–1132 (1962).

14.   Molinari, A., Hahn, H. & Kruk, R. Voltage-Control of Magnetism in All-Solid-State and Solid/Liquid Magnetoelectric Composites. *Adv. Mater.* **31**, 1806662 (2019).

15.   Schmid, H. Multi-ferroic Magnetoelectrics. *Ferroelectrics* **162**, 317–338 (1992).

16.   N. Astrov, D. Magnetoelectric Effect in chromium oxide. *Sov. Phys. JETP* **13**, 729–733 (1961).

17.   Folen, V. J., Rado, G. T. & Stalder, E. W. Anisotropy of the magnetoelectric effect in Cr2O3. *Phys. Rev. Lett.* **6**, 607–608 (1961).

18.   Catalan, G. & Scott, J. F. Physics and applications of bismuth ferrite. *Adv. Mater.* **21**, 2463–2485 (2009).

19.   Matsubara, M. *et al.* Magnetoelectric domain control in multiferroic $TbMnO_3$. *Science (80-.).* **348**, 1112–1115 (2015).

20.   Pascual-Gonzalez, C., Schileo, G. & Feteira, A. Single-phase, composite and laminate multiferroics. Magnetic, Ferroelectric, and Multiferroic Metal Oxides (Elsevier Inc., 2018).

21.   O'Handley, R. C. Modern Magnetic Materials. John Wiley & Sons, inc. vol. 13 (1999).

22.   Reports, P. R. Product properties: a new application of composite materials. **27**, 28–37 (1972).

23.   Chaudhuri, A. & Mandal, K. Large magnetoelectric properties in $CoFe_2O_4$:$BaTiO_3$ core-shell nanocomposites. *J. Magn. Magn. Mater.* **377**, 441–445 (2015).

24.   Islam, R. A., Bedekar, V., Poudyal, N., Liu, J. P. & Priya, S. Magnetoelectric properties of core-shell particulate nanocomposites. *J. Appl. Phys.* **104**, 8–12 (2008).

25.   Lee, M. K., Nath, T. K., Eom, C. B., Smoak, M. C. & Tsui, F. Strain modification of epitaxial perovskite oxide thin films using structural transitions of ferroelectric $BaTiO_3$ substrate. *Appl. Phys. Lett.* **77**, 3547–3549 (2000).

26.   Sheng, Z. G., Gao, J. & Sun, Y. P. Coaction of electric field induced strain and polarization effects in $La_{0.7} Ca_{0.3} MnO_3$ /PMN-PT structures. *Phys. Rev. B - Condens. Matter Mater. Phys.* **79**, 1–6 (2009).

27.   Thiele, C., Dörr, K., Bilani, O., Rödel, J. & Schultz, L. Influence of strain on the magnetization and magnetoelectric effect in $La_{0.7} A_{0.3} Mn O_3$ PMN-PT (001) (A=Sr,Ca). *Phys. Rev. B - Condens. Matter Mater. Phys.* **75**, 1–8 (2007).

28.   Qi Guo , Xiaoguang Xu, Fang Wang, Yunhao Lu, Jikun Chen, Yanjun Wu, Kangkang Meng, Yong Wu, Jun Miao, Y. J. In-plane electric field controlled ferromagnetism and anisotropic magnetoresistance in a LSMO/PMN-PT heterostructure. *Nanotechnology* **22**, 224003 (2019).

29.   Geprägs, S., Mannix, D., Opel, M., Goennenwein, S. T. B. & Gross, R. Converse magnetoelectric effects in $Fe_3O_4/BaTiO_3$ multiferroic hybrids. *Phys. Rev. B - Condens. Matter Mater. Phys.* **88**, 054412 (2013).

30.   Brivio, S., Petti, D., Bertacco, R. & Cezar, J. C. Electric field control of magnetic anisotropies and magnetic coercivity in Fe/BaTiO3 (001) heterostructures. *Appl. Phys. Lett.* **98**, (2011).

31. Venkataiah, G., Shirahata, Y., Itoh, M. & Taniyama, T. Manipulation of magnetic coercivity of Fe film in $Fe/BaTiO_3$ heterostructure by electric field. *Appl. Phys. Lett.* **99**, 102506 (2011).

32. Sahoo, S. *et al.* Ferroelectric control of magnetism in $BaTi\ O_3$ Fe heterostructures via interface strain coupling. *Phys. Rev. B - Condens. Matter Mater. Phys.* **76**, 092108 (2007).

33. Lou, J., Liu, M., Reed, D., Ren, Y. & Sun, N. X. Giant electric field tuning of magnetism in novel multiferroic FeGaB/Lead zinc niobate-lead titanate (PZN-PT) heterostructures. *Adv. Mater.* **21**, 4711–4715 (2009).

34. Lee, J. W., Shin, S. C. & Kim, S. K. Spin engineering of CoPd alloy films via the inverse piezoelectric effect. *Appl. Phys. Lett.* **82**, 2458–2460 (2003).

35. Laletsin, U., Padubnaya, N., Srinivasan, G. & Devreugd, C. P. Frequency dependence of magnetoelectric interactions in layered structures of ferromagnetic alloys and piezoelectric oxides. *Appl. Phys. A Mater. Sci. Process.* **78**, 33–36 (2004).

36. Ryu, J., Carazo, A. V., Uchino, K. & Kim, H. E. Magnetoelectric properties in piezoelectric and magnetostrictive laminate composites. *Japanese J. Appl. Physics, Part 1 Regul. Pap. Short Notes Rev. Pap.* **40**, 4948–4951 (2001).

37.   Ghidini, M. *et al.* Non-volatile electrically-driven repeatable magnetization reversal with no applied magnetic field. *Nat. Commun.* **4**, 4:1453 (2013).

38.   Shirahata, Y. *et al.* Electric-field switching of perpendicularly magnetized multilayers. *NPG Asia Mater.* **7**, e198 (2015).

39.   Lei, N. *et al.* Magnetization reversal assisted by the inverse piezoelectric effect in Co-Fe-B/ferroelectric multilayers. *Phys. Rev. B - Condens. Matter Mater. Phys.* **84**, 4–7 (2011).

40.   Ahn, C. H. *et al.* Electrostatic modification of novel materials. *Rev. Mod. Phys.* **78**, 1185–1212 (2006).

41.   Coey, J. M. D., Viret, M. & Von Molnár, S. Mixed-valence manganites. *Adv. Phys.* **58**, 571–697 (2009).

42.   Ohno, H. *et al.* Electric-field control of ferromagnetism. *Nature* **408**, 944–946 (2000).

43.   Chiba, D., Yamanouchi, H., Hatsukura, F. & Ohno, H. Electrical manipulation of magnetization reversal in a ferromagnetic semiconductor. *Science* **301**, 943–945 (2003).

44.   Liu, X. *et al.* Perpendicular magnetization reversal, magnetic anisotropy, multistep spin switching, and domain nucleation and expansion in $Ga_{1-x}Mn_xAs$ films. *J. Appl. Phys.* **98**, 063904 (2005).

45.   Xiu, F. *et al.* Electric-field-controlled ferromagnetism in high-Curie-temperature $Mn_{0.05}Ge_{0.95}$ quantum dots. *Nat. Mater.* **9**, 337–344 (2010).

46.   Tu, N. T., Hai, P. N., Anh, L. D. & Tanaka, M. Electrical control of ferromagnetism in the n -type ferromagnetic semiconductor (In,Fe)Sb with high Curie temperature. *Appl. Phys. Lett.* **112**, 122409 (2018).

47.   Yamada, Y. *et al.* Electrically induced ferromagnetism at room temperature in cobalt-doped titanium dioxide. *Science* **332**, 1065–1067 (2011).

48.   Duan, C. G. *et al.* Surface magnetoelectric effect in ferromagnetic metal films. *Phys. Rev. Lett.* **101**, 137201 (2008).

49.   Weisheit, M. *et al.* Electric field-induced modification of magnetism in thin-film ferromagnets. *Science* **315**, 349–351 (2007).

50.   Maruyama, T. *et al.* Large voltage-induced magnetic anisotropy change in a few atomic layers of iron. *Nat. Nanotechnol.* **4**, 158–161 (2009).

51.   Quintana, A. *et al.* Voltage-Induced Coercivity Reduction in Nanoporous Alloy Films: A Boost toward Energy-Efficient Magnetic Actuation. *Adv. Funct. Mater.* **27**, 1–8 (2017).

52.   Navarro-Senent, C. *et al.* Enhancing Magneto-Ionic Effects in Magnetic Nanostructured Films via Conformal Deposition of

Nanolayers with Oxygen Acceptor/Donor Capabilities. *ACS Appl. Mater. Interfaces* **12**, 14484–14494 (2020).

53.   De Rojas, J. *et al.* Voltage control of magnetism with magneto-ionic approaches: Beyond voltage-driven oxygen ion migration. *Appl. Phys. Lett.* **120**, 070501 (2022).

54.   Bauer, U. *et al.* Magneto-ionic control of interfacial magnetism. *Nat. Mater.* **14**, 174–181 (2015).

55.   Bi, C. *et al.* Reversible control of Co magnetism by voltage-induced oxidation. *Phys. Rev. Lett.* **113**, (2014).

56.   Yan, Y. N. *et al.* Electrical control of Co/Ni magnetism adjacent to gate oxides with low oxygen ion mobility. *Appl. Phys. Lett.* **107**, 122407 (2015).

57.   Zhou, X. *et al.* Role of oxygen ion migration in the electrical control of magnetism in Pt/Co/Ni/HfO$_2$ films. *J. Phys. Chem. C* **120**, 1633–1639 (2016).

58.   Diez, L. H. *et al.* Non-volatile ionic modification of the Dzyaloshinskii Moriya Interaction. *Phys. Rev. Appl.* **12**, 034005 (2019).

59.   Gilbert, D. A. *et al.* Structural and magnetic depth profiles of magneto-ionic heterostructures beyond the interface limit. *Nat. Commun.* **7**, 12264 (2016).

60. Chen, G. *et al.* Observation of Hydrogen-Induced Dzyaloshinskii-Moriya Interaction and Reversible Switching of Magnetic Chirality. *Phys. Rev. X* **11**, 021015 (2021).

61. Tan, A. J. *et al.* Hydration of gadolinium oxide (Gd Ox) and its effect on voltage-induced Co oxidation in a Pt/Co/Gd Ox/Au heterostructure. *Phys. Rev. Mater.* **3**, 064408 (2019).

62. Tan, A. J. *et al.* Magneto-ionic control of magnetism using a solid-state proton pump. *Nat. Mater.* **18**, 35–41 (2019).

63. Zehner, J. *et al.* Magnetoionic control of perpendicular exchange bias. *Phys. Rev. Mater.* **5**, L061401 (2021).

64. Zhu, X. *et al.* In Situ Nanoscale Electric Field Control of Magnetism by Nanoionics. *Adv. Mater.* **28**, 7658–7665 (2016).

65. Zhang, Q. *et al.* Lithium-Ion Battery Cycling for Magnetism Control. *Nano Lett.* **16**, 583–587 (2016).

66. Dasgupta, S. *et al.* Toward On-and-Off Magnetism: Reversible Electrochemistry to Control Magnetic Phase Transitions in Spinel Ferrites. *Adv. Funct. Mater.* **26**, 7507–7515 (2016).

67. Dasgupta, S. *et al.* Intercalation-driven reversible control of magnetism in bulk ferromagnets. *Adv. Mater.* **26**, 4639–4644 (2014).

68.   Wei, G. *et al.* Reversible control of magnetization of Fe_3O_4 by a solid-state film lithium battery. *Appl. Phys. Lett.* **110**, (2017).

69.   De Rojas, J. *et al.* Critical Role of Electrical Resistivity in Magnetoionics. *Phys. Rev. Appl.* **16**, 034042 (2021).

70.   De Rojas, J. *et al.* Magneto-Ionics in Single-Layer Transition Metal Nitrides. *ACS Appl. Mater. Interfaces* **13**, 30826–30834 (2021).

71.   de Rojas, J. *et al.* Voltage-driven motion of nitrogen ions: a new paradigm for magneto-ionics. *Nat. Commun.* **11**, 5871 (2020).

72.   Vasala, S. *et al.* Reversible Tuning of Magnetization in a Ferromagnetic Ruddlesden–Popper-Type Manganite by Electrochemical Fluoride-Ion Intercalation. *Adv. Electron. Mater.* **6**, 1900974 (2019).

73.   Huang, M. *et al.* Voltage control of ferrimagnetic order and voltage-assisted writing of ferrimagnetic spin textures. *Nat. Nanotechnol.* **16**, 981–988 (2021).

74.   Yi, D. *et al.* Emergent electric field control of phase transformation in oxide superlattices. *Nat. Commun.* **11**, 902 (2020).

75.   Navarro-Senent, C. *et al.* Large Magnetoelectric Effects in Electrodeposited Nanoporous Microdisks Driven by Effective Surface Charging and Magneto-Ionics. *ACS Appl. Mater. Interfaces* **10**, 44897–44905 (2018).

76.   Robbennolt, S. *et al.* Magneto-ionic control of magnetism in two-oxide nanocomposite thin films comprising mesoporous cobalt ferrite conformally nanocoated with HfO_2. *Nanoscale* **12**, 5987–5994 (2020).

77.   Robbennolt, S. *et al.* Reversible, Electric-Field Induced Magneto-Ionic Control of Magnetism in Mesoporous Cobalt Ferrite Thin Films. *Sci. Rep.* **9**, 10804 (2019).

78.   Gilbert, D. A. *et al.* Controllable positive exchange bias via redox-driven oxygen migration. *Nat. Commun.* **7**, 11050 (2016).

79.   Chen, G. *et al.* Large Dzyaloshinskii-Moriya interaction induced by chemisorbed oxygen on a ferromagnet surface. *Sci. Adv.* **6**, eaba4924 (2020).

80.   Duschek, K., Uhlemann, M., Schlörb, H., Nielsch, K. & Leistner, K. Electrochemical and in situ magnetic study of iron/iron oxide films oxidized and reduced in KOH solution for magneto-ionic switching. *Electrochem. commun.* **72**, 153–156 (2016).

81.   Grutter, A. J. *et al.* Reversible control of magnetism in La0.67Sr0.33MnO3 through chemically-induced oxygen migration. *Appl. Phys. Lett.* **108**, 082405 (2016).

82.   Duschek, K., Pohl, D., Fähler, S., Nielsch, K. & Leistner, K. Research Update: Magnetoionic control of magnetization and anisotropy in layered oxide/metal heterostructures. *APL Mater.* **4**, 032301 (2016).

83.   Duschek, K., Petr, A., Zehner, J., Nielsch, K. & Leistner, K. All-electrochemical voltage-control of magnetization in metal oxide/metal nanoislands. *J. Mater. Chem. C* **6**, 8411–8417 (2018).

84.   Voltage-Controlled Deblocking of Magnetization Reversal in Thin Films by Tunable. *Adv. Electron. Mater.* **6**, 2000406 (2020).

85.   Zehner, J. *et al.* Robust Magneto-Ionic Effect in Fe/FeOx Thin Films in Electrolytes With Different Cations. *IEEE Trans. Magn.* **58**, 6000108 (2022).

86.   Robbennolt, S. *et al.* Electric Field Control of Magnetism in Iron Oxide Nanoporous Thin Films. *ACS Appl. Mater. Interfaces* **11**, 37338–37346 (2019).

87.   Tsuchiya, T. *et al.* In situ tuning of magnetization and magnetoresistance in Fe_3O_4 thin film achieved with all-solid-state redox device. *ACS Nano* **10**, 1655–1661 (2016).

88.   Quintana, A. *et al.* Voltage-Controlled ON-OFF Ferromagnetism at Room Temperature in a Single Metal Oxide Film. *ACS Nano* **12**, 10291–10300 (2018).

89.   de Rojas, J. *et al.* Boosting Room-Temperature Magneto-Ionics in a Non-Magnetic Oxide Semiconductor. *Adv. Funct. Mater.* **30**, 2003704 (2020).

90.   Nastasi, M. & Mayer, J. W. Ion Implantation and Synthesis of Materials. Management (2006).

91.   Lee, K. Y. *et al.* Fast magneto-ionic switching of interface anisotropy using yttria-stabilized zirconia gate oxide. *Nano Lett.* **20**, 3435–3441 (2020).

92.   Lee, J. & Lu, W. D. On-Demand Reconfiguration of Nanomaterials: When Electronics Meets Ionics. *Adv. Mater.* **30**, 1702770 (2017).

93.   Luo, Z. *et al.* Reconfigurable Magnetic Logic Combined with Nonvolatile Memory Writing. *Adv. Mater.* **29**, 201605027 (2016).

94.   Navau, C. & Sort, J. Exploiting random phenomena in magnetic materials for data security, logics, and neuromorphic computing: Challenges and prospects. *APL Mater.* **9**, 070903 (2021).

95.   D'Souza, N., Salehi Fashami, M., Bandyopadhyay, S. & Atulasimha, J. Experimental Clocking of Nanomagnets with Strain for Ultralow Power Boolean Logic. *Nano Lett.* **16**, 1069–1075 (2016).

96.   Manipatruni, S. *et al.* Scalable energy-efficient magnetoelectric spin–orbit logic. *Nature* **565**, 35–42 (2019).

97.   Li, X., Lee, A., Razavi, S. A., Wu, H. & Wang, K. L. Voltage-controlled magnetoelectric memory and logic devices. *MRS Bull.* **43**, 970–977 (2018).

98.   Sundaram, S., Skouras, M., Kim, D. S., van den Heuvel, L. & Matusik, W. Topology optimization and 3D printing of multimaterial magnetic actuators and displays. *Sci. Adv.* **5**, eaaw1160 (2019).

99.   Rahmer, J., Stehning, C. & Gleich, B. Spatially selective remote magnetic actuation of identical helical micromachines. *Sci. Robot.* **2**, eaal2845 (2017).

100.   Kim, J. *et al.* Programming magnetic anisotropy in polymeric microactuators. *Nat. Mater.* **10**, 747–752 (2011).

101.   Dubraja, L. A. *et al.* Electrochemical Tuning of Magnetism in Ordered Mesoporous Transition-Metal Ferrite Films for Micromagnetic Actuation. *ACS Appl. Nano Mater.* **1**, 65–72 (2018).

102.   Ikeda, S. *et al.* A perpendicular-anisotropy CoFeB-MgO magnetic tunnel junction. *Nat. Mater.* **9**, 721–724 (2010).

103.   Yan, Y. *et al.* Strong Electrical Manipulation of Spin–Orbit Torque in Ferromagnetic Heterostructures. *Adv. Electron. Mater.* **2**, 1600219 (2016).

104.   Chen, X. *et al.* Interfacial oxygen migration and its effect on the magnetic anisotropy in Pt/Co/MgO/Pt films. *Appl. Phys. Lett.* **104**, 052413 (2014).

105.   Koyama, T., Nakatani, Y., Ieda, J. & Chiba, D. Electric field control of magnetic domain wall motion via modulation of the Dzyaloshinskii-Moriya interaction. *Sci. Adv.* **4**, eaav0265 (2018).

106.   Gilbert, D. A. *et al.* Realization of ground-state artificial skyrmion lattices at room temperature. *Nat. Commun.* **6**, 8462 (2015).

107.   Rosch, A. Skyrmion Lattice in a Chiral Magnet. *Science (80-.).* **323**, 915–919 (2009).

108.   Luo, Z. *et al.* Chirally coupled nanomagnets. *Science (80-.).* **363**, 1435–1439 (2019).

109.   Chen, G. *et al.* Novel chiral magnetic domain wall structure in Fe/Ni/Cu(001) Films. *Phys. Rev. Lett.* **110**, 177204 (2013).

OBJECTIVES
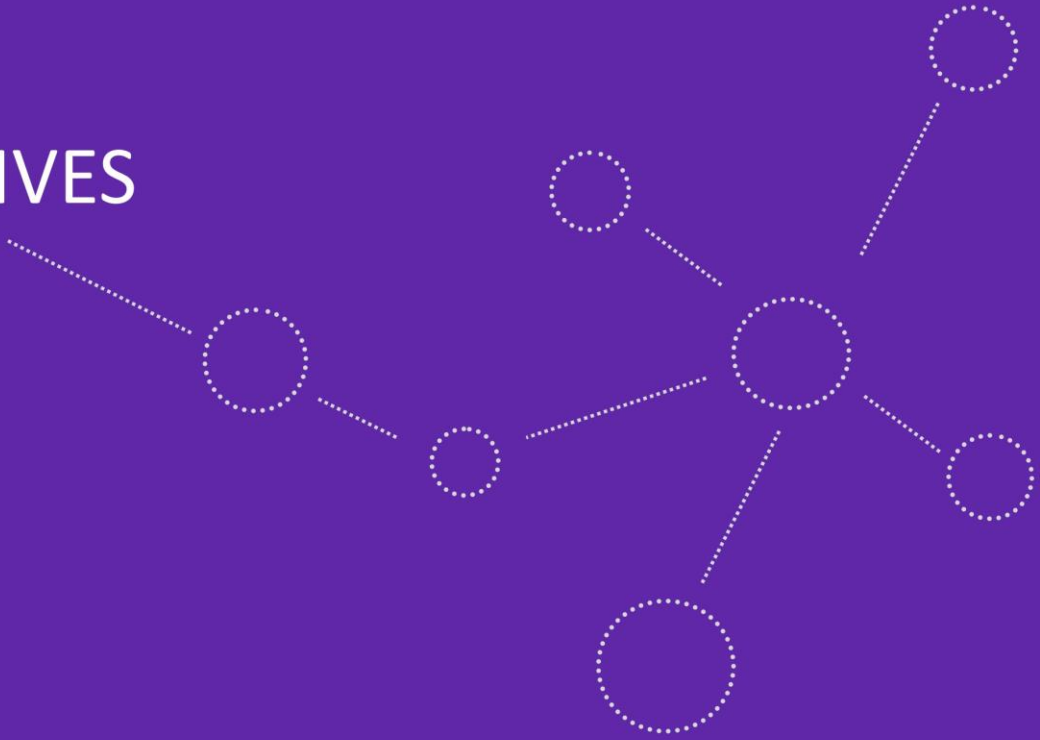
This work is mostly aimed at boosting oxygen motion in electrolyte-gated paramagnetic cobalt oxide (Co-oxide) films using three different approaches:

- By decreasing film thickness from >200 nm to 5 nm

For this purpose, Co-oxide films of varying thickness were grown by reactive sputtering to study the impact of film thickness on the magneto-ionic ON-OFF transition rate. A protocol based on pulsed voltages was developed and implemented to mimic neuromorphic functionalities.

- By adding salts to the PC electrolyte to increase the EDL strength (electrolyte engineering)

We aim to investigate the effect that different salts dissolved in PC (and their concentrations) have on the magneto-ionic performance of 15 nm-thick Co-oxide films, in order to determine the optimum condition for the fastest magneto-ionic response.

- By engineering the microstructure in terms of depth-resolved defect type and density by light-ion implantation

We will exploit the potential of ion implantation to engineer structural defects along depth to enhance voltage-driven O ion transport.

RESULTS AND DISCUSSION
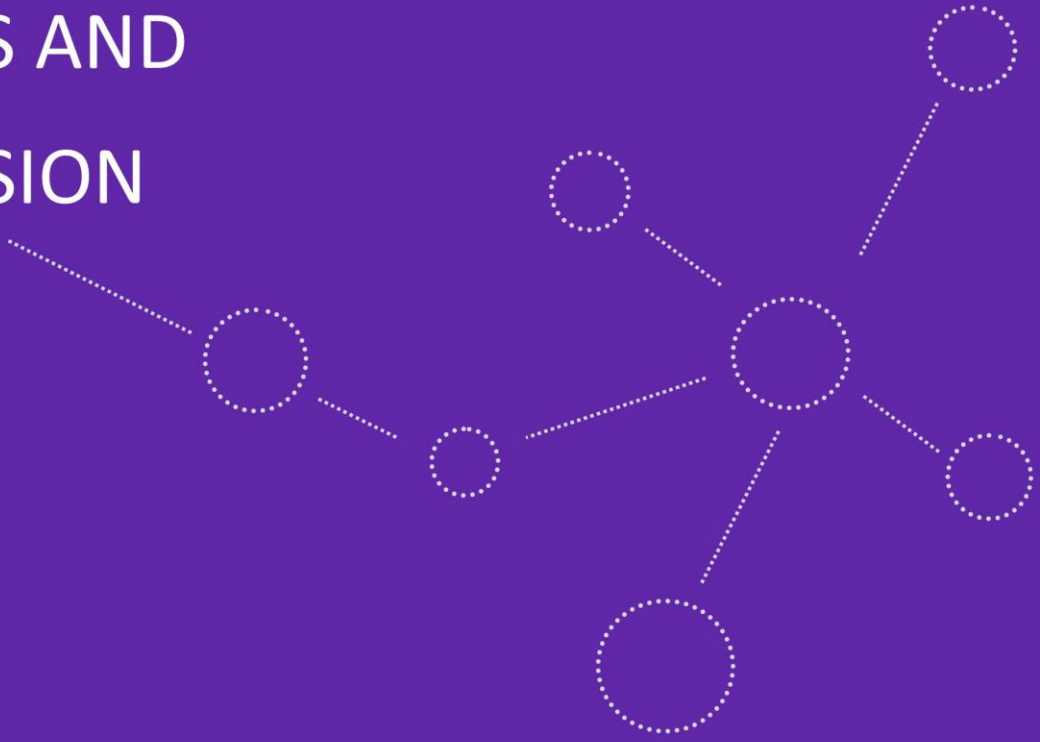
In this chapter, the results derived from this Thesis are organized in the 'compilation of articles' format. Specifically, two peer-review research papers are included:

3.1) Dynamic electric-field-induced magnetic effects in cobalt oxide thin films: towards magneto-ionic synapsis

3.2) Enhancing magneto-ionic effects in cobalt oxide films by electrolyte engineering

3.3) Controlling magneto-ionics by defect engineering through light ion implantation

A brief summary to highlight the main outcomes of the study precedes each publication, while a comprehensive discussion of the results can be found in the articles themselves. For an overall, general discussion of the results of the Thesis, please refer to chapter 4.

3.1.   Dynamic electric-field-induced magnetic effects in cobalt oxide thin films: towards magneto-ionic synapsis

Sofia Martins,[a] Julius de Rojas,[a] Zhengwei Tan,[a] Matteo Cialone,[b] Aitor Lopeandia,[c] Javier Herrero-Martín,[d] José L. Costa-Krämer,[e] Enric Menéndez*[a] and Jordi Sort*[a,f]

[a]Departament de Física, Universitat Autònoma de Barcelona, E-08193 Cerdanyola del Vallès, Spain. E-mail: Enric.Menendez@uab.cat, Jordi.Sort@uab.cat
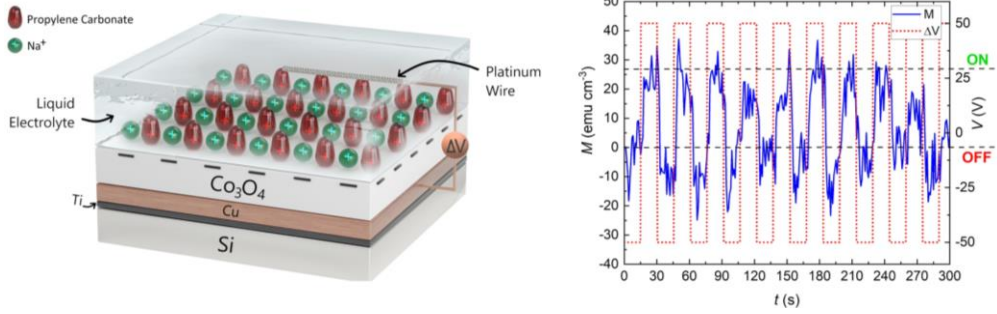
[b]CNR-SPIN Genova, C.so F. M. Perrone 24, Genova, 16152, Italy

[c]Catalan Institute of Nanoscience and Nanotechnology (ICN2), CSIC and BIST, Campus UAB, Cerdanyola del Vallès, E-08193 Barcelona, Spain

[d]ALBA Synchrotron Light Source, 08290 Cerdanyola del Vallès, Spain

[e]IMN-Instituto de Micro y Nanotecnología (CNM-CSIC), Isaac Newton 8, PTM, 28760 Tres Cantos, Madrid, Spain

[f]Institució Catalana de Recerca i Estudis Avançats (ICREA), Pg. Lluís Companys 23, E-08010 Barcelona, Spain

In this study, we show that by drastically decreasing film thickness from > 200 nm down to 5 nm, sub-second ON-OFF transitions in electrolyte-gated paramagnetic cobalt oxide films can be accomplished. Interestingly, applying voltage pulses at frequency as high as 100 Hz can also promote cumulative magneto-ionic effects. These frequencies exhibit neuromorphic-like dynamic effects, such as potentiation (cumulative increase in magnetization), depression (*i.e.*, partial recovery of magnetization with time), threshold activation, and spike time-dependent magnetic plasticity (learning and forgetting abilities). These effects mimic many of the primary biological synapse functions. As a result, the systems under study exhibit characteristics, such as operational dynamic range, that could be helpful for the development of artificial neural networks whose magnetic properties would be controlled by applied voltage (*i.e.*, magneto-ionic synapses).

Nanoscale

rsc.li/nanoscale
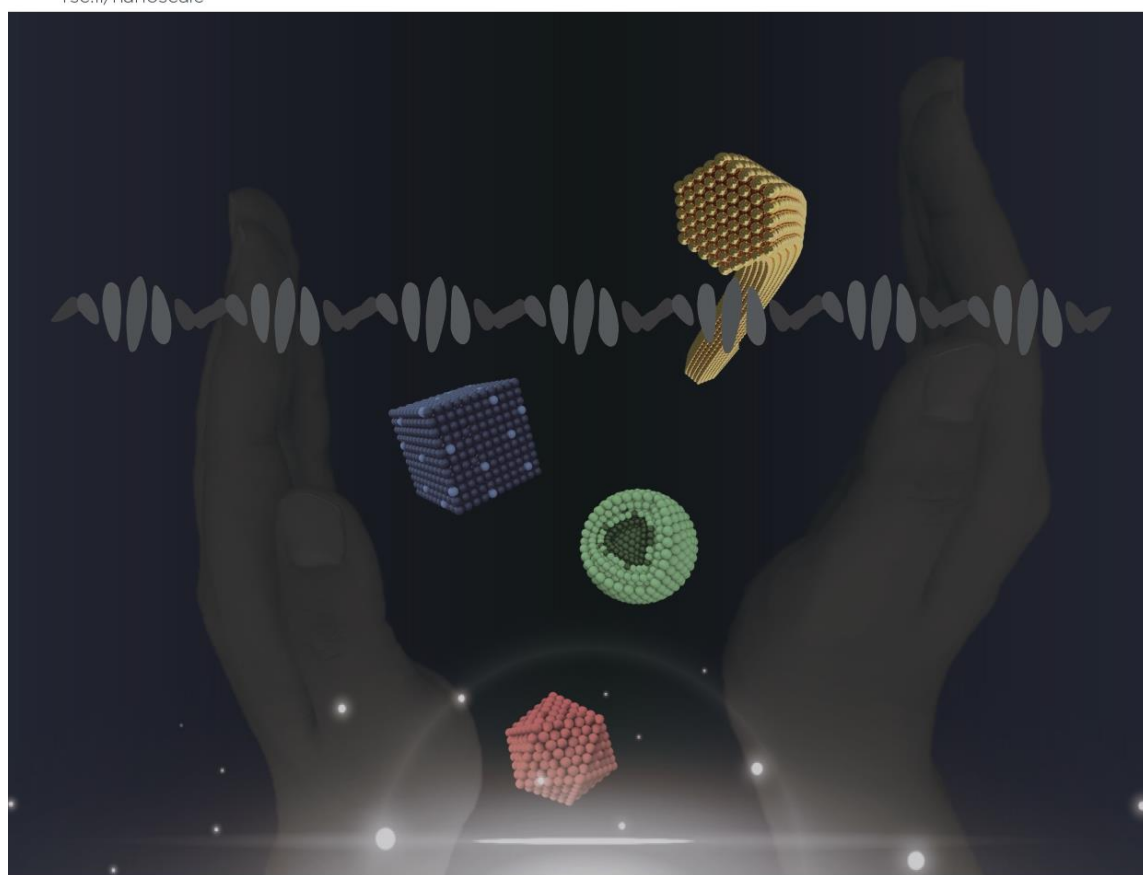
ROYAL SOCIETY
OF CHEMISTRY

MINIREVIEW
Taotao Zhuang *et al.*
Amplifying inorganic chirality using liquid crystals

NCNST

PAPER

Dynamic electric-field-induced magnetic effects in cobalt oxide thin films: towards magneto-ionic synapses†

Sofia Martins, [a] Julius de Rojas,[a] Zhengwei Tan, [a,b] Matteo Cialone,[b] Aitor Lopeandia,[c] Javier Herrero-Martín,[d] José L. Costa-Krämer, [e] Enric Menéndez*[a] and Jordi Sort [*a,f]

Voltage control of magnetism *via* electric-field-driven ion migration (magneto-ionics) has generated intense interest due to its potential to greatly reduce heat dissipation in a wide range of information technology devices, such as magnetic memories, spintronic systems or artificial neural networks. Among other effects, oxygen ion migration in transition-metal–oxide thin films can lead to the generation or full suppression of controlled amounts of ferromagnetism ('ON–OFF' magnetic transitions) in a non-volatile and fully reversible manner. However, oxygen magneto-ionic rates at room temperature are generally considered too slow for industrial applications. Here, we demonstrate that sub-second ON–OFF transitions in electrolyte-gated paramagnetic cobalt oxide films can be achieved by drastically reducing the film thickness from >200 nm down to 5 nm. Remarkably, cumulative magneto-ionic effects can be generated by applying voltage pulses at frequencies as high as 100 Hz. Neuromorphic-like dynamic effects occur at these frequencies, including potentiation (cumulative magnetization increase), depression (*i.e.*, partial recovery of magnetization with time), threshold activation, and spike time-dependent magnetic plasticity (learning and forgetting capabilities), mimicking many of the biological synapse functions. The systems under investigation show features that could be useful for the design of artificial neural networks whose magnetic properties would be governed with voltage.

1. Introduction

With the advent of Big Data, current computational architectures are proving to be insufficient.[1] Miniaturization of complementary metal–oxide semiconductor (CMOS) technologies (Moore's law) is starting to show signs of deceleration because of the difficulties in decreasing transistor size below 10 nm,[2] while the areal density in hard disk drives (HDDs) is also limited by the superparamagnetic effect, relying on technologies such as heat assisted magnetic recording (HAMR) to reduce bit sizes.[3] In addition, increasingly complex algorithms

need to be performed in a much faster and energy-efficient manner. This is not easy in the current von Neumann computer architecture, in which the mass storage sub-device (*e.g.*, HDD) is placed separately from the data processing unit and the random-access memory (RAM) that keep data in read-write mode. The shuffling of data between the processing unit and the memories results in large power consumption[4] and computational speeds that are limited by the frequency at which the memory sub-devices can transfer data to the processing unit.[5]

To meet the demands of artificial intelligence and the Internet of Things, a new brain-inspired computation paradigm, neuromorphic computing, has emerged as an alternative. Neuromorphic computing emulates the activity of biological synapses by utilizing artificial neural networks in which synapses are massively interconnected in a dynamic and reconfigurable way to process information in an energy-efficient manner.[6–9] Although the bases of this computation paradigm were formulated in the 1990s,[8,10] a renewed interest has emerged in recent years, jump-started by the discovery and development of advanced materials that might address some of the essential requirements of brain-inspired computing. So far, emulation of artificial synapses has been achieved, to some extent, using phase change materials,[11] superconduc-

[a]Departament de Física, Universitat Autònoma de Barcelona, E-08193 Cerdanyola del Vallès, Spain. E-mail: Enric.Menendez@uab.cat, Jordi.Sort@uab.cat
[b]CNR-SPIN Genova, C.so F. M. Perrone 24, Genova, 16152, Italy
[c]Catalan Institute of Nanoscience and Nanotecnology (ICN2), CSIC and BIST, Campus UAB, Cerdanyola del Vallès, E-08193 Barcelona, Spain
[d]ALBA Synchrotron Light Source, 08290 Cerdanyola del Vallès, Spain
[e]IMN-Instituto de Micro y Nanotecnología (CNM-CSIC), Isaac Newton 8, PTM, 28760 Tres Cantos, Madrid, Spain
[f]Institució Catalana de Recerca i Estudis Avançats (ICREA), Pg. Lluís Companys 23, E-08010 Barcelona, Spain
†Electronic supplementary information (ESI) available. See DOI: 10.1039/d1nr06210g

tors,[12] transistors,[13] spintronic devices[14,15] andmemristors.[16,17] However, meeting technical requirements such as room-temperature operation, high speeds, chip integration/compatibility and low power consumption remains a challenge.[18] Many of the above-mentioned materials are ultimately controlled by electric currents, which involve significant energy loss by heat dissipation through the Joule effect and the associated cooling requirements.

In recent years, voltage control of magnetism has attracted intense research interest because it has the potential to drastically decrease energy consumption, thereby rendering ultralow-power data storage.[19–22] While magnetoelectric actuation protocols have been proposed as an alternative to thermally-assisted magnetic recording and in new designs of random-access memories, research on the use of this effect for neuromorphic computing is promising but still in early stages.[23,24] Yet, two important advantages of magnetoelectric designs over memristor-like materials, besides energy efficiency, are envisioned:[23] the use of different read/write paths (which avoids interference between synapses during the read operation), and the possibility to induce negative synaptic weights, taking advantage of the fact that magnetization is a vector, whereas electrical conductance is a scalar quantity. This allows the synapse to be programmed with either excitatory signals (via a positive weight) or inhibitory signals (via a negative weight), mimicking the brains capability to increase/decrease the membrane potential of postsynaptic neurons under certain conditions. So far, electric-field control of magnetism has primarily relied on the following strategies:[19] (i) the use of single-phase multiferroic materials with intrinsic magnetoelectric coupling,[25,26] (ii) electric charge accumulation in ferromagnetic metals or semiconductors[27,28] and (iii) piezostrain-mediated effects through inverse magnetostriction in ferromagnetic/ferroelectric heterostructures.[29–31] The implementation of these approaches in marketable devices is hampered by several factors. Intrinsic multiferroics are scarce and show relatively weak magnetoelectric coupling at room temperature. The penetration of an applied electric-field (i.e., electronic charging) in metallic or semiconducting ferromagnets is limited to the very outer surface (screening length in metals is around 5 Å), thus imposing strong thickness restrictions on the actuated materials. Finally, artificial multiferroic ferromagnetic/ferroelectric heterostructures suffer from fatigue effects, clamping effects when grown onto a rigid substrate, and high voltage requirements when the ferromagnetic layer is directly grown onto a ferroelectric substrate. Even though clamping effects would be minimized by using flexible polymer-based ferroelectrics, the capacity of piezostrain-mediated effects to modulate magnetic properties is more limited than that of magneto-ionics.

An alternative to the above mechanisms is the use of an applied electric-field to induce ion migration effects that modify the magnetic properties of materials (magneto-ionics).[32–42] Magneto-ionics can extend to the bulk (beyond the outer surface of target films), induces non-volatile (i.e., permanent) changes in the magnetic properties, and has been reported to be highly energy efficient. Magneto-ionics involves write/delete energies per bit lower than 10^{-3} pJ per bit.[43,44] This represents energies several orders of magnitude lower than those required by memristors (10^{-1} pJ per bit), conventional toggle MRAMs (1 pJ per bit), or HDDs ($>10^3$ pJ per bit).[45–47] However, magneto-ionic motion of oxygen at room temperature is usually rather slow, involving several seconds or even minutes to toggle the magnetic state. Since ion migration is a thermally activated process, magneto-ionic rates can be accelerated if the system is heated while voltage is applied, but at the cost of reduced energy efficiency. Recently, via a proton-based approach (i.e., H^+ ion migration),[33,34] 10^{-3} s room-temperature operation has been shown in yttria-stabilized zirconia/Pd/Co heterostructures.[33] This approach is very appealing, but still needs further optimization to increase hydrogen retention and make the system less dependent on environmental humidity.

The use of pristine ferromagnetic layers (e.g., Co, Ni or Fe) as starting materials grown adjacent to ionic conductors (e.g., HfO_2, GdO_x, Al_2O_3) poses some drawbacks. First, it is often difficult to achieve a fully OFF state (i.e., full oxidation) by voltage application; the most frequently reported effect is a voltage-induced reorientation of the magnetic easy axis. Second, when the metal is oxidized, pronounced structural changes (i.e., phase transformations) take place, leading to irreversible structural effects and, thus, poor cyclability and endurance. An alternative approach is to use target materials whose crystal structure already contains the ions to be transported (i.e., magneto-ionic targets such as Co_3O_4[35,37] or CoN[36,48] to transport oxygen or nitrogen, respectively). Such magneto-ionic targets can undergo fully reversible transformations from a non-ferromagnetic (OFF) to a ferromagnetic (ON) state and vice versa, just by the generation of atomic vacancies.[35–37] This has been demonstrated at room temperature in electrolyte-gated paramagnetic Co_3O_4 and CoN films. In our previous works, we investigated relatively thick (≥85 nm) layers, which took several minutes to generate a magnetic moment equal to few % of the saturation magnetization of bulk metallic Co.[35–37]

Here, we show novel results in electrolyte-gated thin cobalt oxide layers at room temperature using static (DC) and pulsed voltage. By reducing the cobalt oxide layer thickness down to 5 nm, sub-second ON–OFF magnetic transformations are demonstrated. Remarkably, through application of pulsed voltage functions, activation times of 10^{-2} s can be inferred. At such frequencies, the investigated material shows some interesting neuromorphic functionalities, such as cumulative (learning) and relaxation (forgetting) time-dependent magnetization dependences, under suitable voltage conditions.

2. Experimental

2.1. Sample preparation

Cobalt oxide films were grown at room temperature on Si/Ti/Cu substrates (i.e., Cu (60 nm)/Ti (20 nm)/⟨100⟩Si (725 μm)) by

55

reactive sputtering using a cobalt target as Co precursor and O_2 plasma as oxygen source. Argon was used as a carrier gas for the Co precursor. The deposition was performed with an AJA International, Inc. Magnetron Sputtering System ATC Orion with a base pressure of 10^{-7} mbar. Sputtering was conducted using a DC gun applying 200 W. The deposition rate was 23 nm min^{-1}. The adhesive (Ti) and seed (Cu) layers were also grown by sputtering using the same experimental setup but in an inert atmosphere. Cu wires were welded to the electrodes using indium. Insulating hot glue spacers were used to avoid short-circuits.

2.2. Structural measurements

θ–2θ X-ray diffraction (XRD) patterns of the different samples were recorded on a Philips XPert Powder diffractometer using Cu Kα radiation. The structural parameters of films, such as crystallite size (i.e., average coherently diffracting domain), lattice parameters or microstrains were evaluated by fitting the XRD patterns using the MAUD Rietveld refinement software. High-resolution transmission electron microscopy (HRTEM) was performed on a TECNAI F20 HRTEM/STEM microscope operated at 200 kV. A cross sectional lamella was prepared by focused ion beam and placed onto a Cu transmission electron microscopy grid.

2.3. Compositional measurements

X-ray absorption spectroscopy (XAS) were investigated at the Co $L_{2,3}$ edges in BL29-BOREAS beamline at ALBA Synchrotron Light Source (Barcelona, Spain).[49] The spectra were measured in total electron yield (TEY) mode, under ultra high vacuum conditions (2×10^{-10} mbar) and at room temperature (300 K). The applied magnetic field (parallel to the X-ray beam) was 6 T, with the magnetic field along in-plane direction forming an angle of 30° with the film surface.
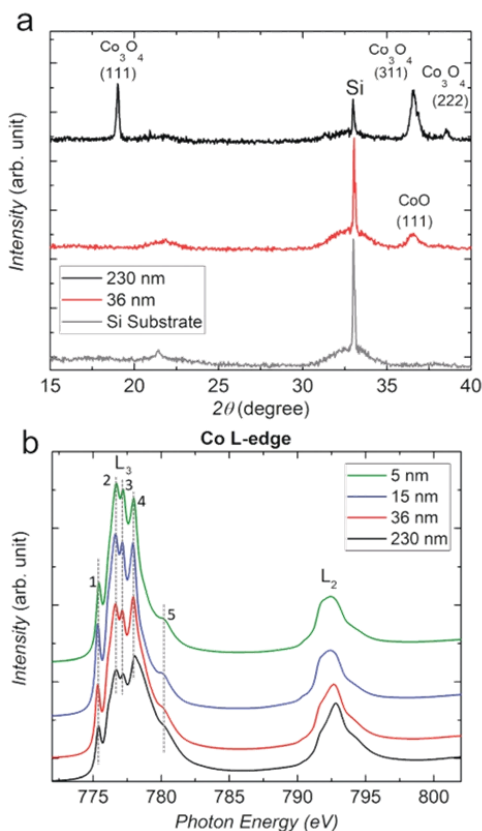
2.4. Magnetoelectric characterization

Magnetic measurements under electrolyte gating were carried out at room temperature in a vibrating sample magnetometer (VSM) from Micro Sense (LOT-Quantum Design), with a maximum in-plane applied magnetic field of 2 T in samples with electrochemical capacitor configuration, where the working electrode is made on the exposure copper beside to the cobalt oxide layer using the experimental setup as illustrated in Fig. S1† and described in the text. The static and time-dependent magnetic measurements by VSM are given as magnetization M (emu cm^{-3}) vs. applied magnetic field H (Oe) and magnetization M (emu cm^{-3}) vs. time t (h), respectively. To give M in T, the M values given in emu cm^{-3} should be first multiplied by 1000 to obtain M in A m^{-1}, and then by μ_0 ($\mu_0 = 4\pi \times 10^{-7}$ N A^{-2}): $\mu_0 M$ (T) $= 4\pi \times 10^{-4}M$ (emu cm^{-3}). Additionally, the applied magnetic field H can also be given in T (or in mT since T is a rather large unit) if the H values given in Oe are transformed to A m^{-1} (by multiplying by 1000/(4π)), and then multiplied by μ_0 ($\mu_0 = 4\pi \times 10^{-7}$ N A^{-2}): $\mu_0 H$ (mT) $= 10^{-1}H$ (Oe). The magnetic properties were recorded both for the pristine as-grown films and after applying voltage for different times, frequencies and magnetic fields. An Agilent B2902A power supply was used to generate the voltage functions. All magnetoelectric measurements were performed by immersing the sample in propylene carbonate (with traces of Na$^+$ dissolved) and using a platinum wire as counter electrode.[21,35] Taking into account that M vs. H measurements start from positive saturation at 20 000 Oe, the coercivity H_C is taken when the magnetization equals 0 for consecutive descending and ascending magnetic field sweeping branches. The saturation magnetization M_S is determined, upon linear contributions are subtracted, as the value of magnetization at applied magnetic fields of 10 000 Oe and 10 000 Oe for each descending and ascending hysteresis loop branches. For the negative parts of the branches, the absolute value of M_S is considered.

3. Results and discussion

Paramagnetic, semiconducting cobalt oxide films were grown by reactive sputtering on [100]-oriented Si substrates previously coated with Ti (20 nm) and Cu (60 nm) as buffer layers to serve as a working electrode for the voltage actuation. To investigate the role of thickness on the resulting magneto-ionic behavior, a series of cobalt oxide film, ranging from 5 to 230 nm in thickness, were prepared (see Experimental section). To assess the crystalline phases present in the films (as well as the crystallite size and microstrains), the as-grown samples were structurally characterized by XRD. XAS at room temperature was used to characterize the elemental composition and oxidation state of the cobalt oxide films.

As shown in Fig. 1a, besides the peaks from the Si substrate (grey curve), the cobalt oxide films give rise to clear additional diffraction peaks. Peaks with angular positions compatible with the (111), (311) and (222) directions of Co$_3$O$_4$ (PDF 00-009-0418) are observed in the XRD patterns corresponding to the thick (e.g., 230 nm) films (black curve), evidencing polycrystallinity. Note that some diffraction peaks (e.g., the (220) peak, which should appear ≈31°) are not observed, indicating some degree of crystallographic texture. This is in agreement with the tendency of Co$_3$O$_4$ to grow with columnar-shaped grains.[35] However, the presence of (111) and (222) XRD peaks unambiguously indicate the formation of Co$_3$O$_4$ rather than CoO. The 36 nm-thick films show only a single XRD peak around $2\theta = 36.5°$ which is compatible with the position of both the (311) Co$_3$O$_4$ and the (111) CoO (PDF 00-001-1227) crystallographic phases. Note that no peak is observed at 42° (which would correspond to (200) CoO) for 230 nm thick sample. As can be seen in Fig. 1b, the XAS spectra of the 5 and 15 nm thick films consists of one multiplet peak near 775 eV, followed by the splitting of the main peak into three subpeaks, along with a shoulder at 780 eV. These first three peaks (labeled 1, 2, 3 in Fig. 1b) can be associated with the Co^{2+} valence state, and it is consistent with CoO.[50,51] For the 36 nm thick film, 2$^+$ and 3$^+$ oxidation states of Co are observed and, for the 230 nm thick film, the contribution of 3$^+$ oxidation
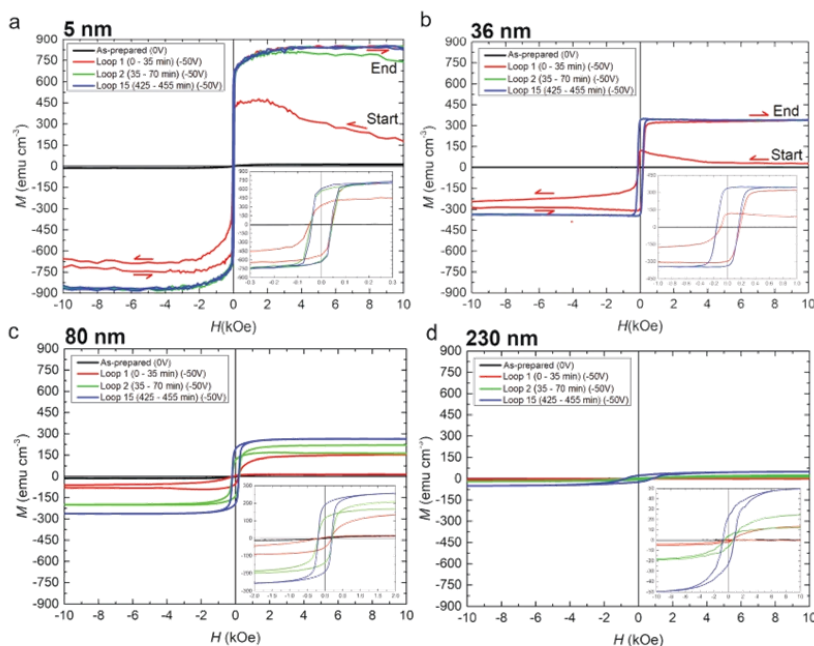
56

Fig. 1 (a) θ–2θ XRD patterns of cobalt oxide films (36 nm and 230 nm thick) and a bare Cu/Ti/Si substrate. (b) Co $L_{2,3}$-edge XAS of the 5, 15, 36 and 230 nm thick cobalt oxide films.

tion of thickness: ranging from CoO to Co_3O_4 for the 5 and 230 nm thick films, respectively. The growth of Co_3O_4 in the thickest films indicates that, while reactive sputtering, the oxygen partial pressure is high enough to grow highly oxidized Co compounds, such as Co_3O_4. Conversely, for the thinnest films, CoO instead of Co_3O_4 is formed, suggesting that the Cu buffer layer might suffer from oxidation, resulting in a decreased effective oxygen partial pressure near the surface, which leads to the formation of a less oxidized cobalt oxide, such as CoO. With increasing thickness, traces of Co^{3+} oxidation state become more pronounced, indicating that coppers role in oxygen capture extends only to the first nm, allowing for more oxidizing conditions as the film continues to grow and, thus, forming Co_3O_4.[52,53] To investigate the role of thickness on the magneto-ionic ion motion and cyclability of cobalt oxide films, samples were magnetoelectrically characterized by VSM during electrolyte-gating (Fig. S1†). Specifically, the heterostructures were immersed in propylene carbonate, which is a aprotic polar anhydrous electrolyte which can dissolve O and, thus, capable of sinking/sourcing O^{2-} ions.[35] A Pt wire was used as counter electrode.

When voltage is applied, an electric double layer (EDL) forms at the interface between cobalt oxide films and the electrolyte which, due to its narrow thickness, allows the generation of large electric-fields perpendicular to the surface of the films (see Fig. S2†).[21]

The samples were subjected to −50 V for several hours and in-plane magnetic hysteresis loops of 35 min duration each were continuously recorded. The first, second and fifteenth hysteresis loops, for four different cobalt oxide thicknesses, together with the hysteresis loops of the as-prepared films, are shown in Fig. 2. Note that the as-prepared cobalt oxide films are virtually non-ferromagnetic, as it corresponds to CoO and Co_3O_4 phases (both are paramagnetic at room temperature). In the thinnest sample (5 nm), M starts to increase immediately after voltage is applied. Because of this progressive increase in M with time, the ascending and descending branches of the loop cross each other. The increase of M is due to the formation of Co clusters resulting from the release of the O^{2-} ions from the magneto-ionic film into the electrolyte.[35,37] Remarkably, the signal reaches a steady-state value after the first M–H loop measurement (i.e., during the first 35 min, red hysteresis loop). A similar result is obtained for the 36 nm thick sample. In contrast, the magnetization of the thicker Co_3O_4 films continues to increase after the first measurement is completed (i.e., for times larger than 35 min). In the case of the thickest sample (230 nm), it takes up to 5 hours to reach a stable saturation magnetization (M_S). From these results it can be inferred that the magneto-ionic rates depend on film thickness (thinner cobalt oxide films result in faster rates), and the amount of generated magnetic signal (normalized per unit volume) is inversely proportional to the film thickness. Comparing the samples after M_S has stabilized, it is observed that the induced M_S increases with decreasing film thickness, while the coercivity (H_C) increases with increasing film thickness.

state increases further, as evidenced by the relative decrease in multiplet peak intensity (1, 2 and 3) relative to the main peak (4) and the broadening of the shoulder (5), consistent with the presence of Co^{3+} in a Co_3O_4 phase.[50] From Rietveld refinements of the XRD patterns, the extracted values of the smallest crystallite size are 33 ± 5 nm and 63 ± 5 nm for the 36 nm and 230 nm thick cobalt oxide films, respectively, revealing that the 36 nm thick films mainly comprise a single layer of crystallites along the thickness of the film, whereas the 230 nm thick films also show polycrystallinity along the film thickness. The microstrains are of the order of 60×10^{-4} and 2×10^{-4} for the thinner and thicker films, respectively, in agreement with a slightly more strained cobalt oxide phase of the 36 nm thick film since the crystallites extend over the whole thickness without dividing and, accumulating certain strain. The XRD and XAS data reveal a transition from CoO to Co_3O_4 as a func-

Fig. 2 Dependence of magneto-ionic effects on the cobalt oxide film thickness. Panels a–d show consecutive hysteresis loops corresponding to cobalt oxide films of 5, 36, 80 and 230 nm thickness, respectively, upon electrolyte gating ($\Delta V = -50$ V) acquired using a vibrating sample magnet-ometer (magnetic field applied in-plane). Note that the hysteresis loops corresponding to the cobalt oxide film of 15 nm thickness are shown in Fig. S4.†

Fig. 3 shows the dependence of the M_S and H_C as function of time, extracted from the ascending and descending branches of the measured hysteresis loops. The magnetization increases with time for all thicknesses, but it does so at a faster rate in thinner cobalt oxide films. In addition, the steady-state M_S value (once taking into account the normaliza-tion by the film thickness) of the 5 nm cobalt oxide film is about 18 times larger than the M_S of the 230 nm film (50 emu cm^{-3} vs. 900 emu cm^{-3}). This corroborates that magneto-ionic effects have a strong dependence on film thickness and are much more pronounced (and occur faster) in thinner tran-sition-metal oxide films. The reason for this is two-fold: first, the generated electric field is larger for thinner cobalt oxide films (by a factor 230/5 = 46); second, in thinner films, O^{2-} ions have to travel shorter distances until they reach the propy-lene carbonate. Additionally, it must be noted that film composition can have some influence on the magneto-ionic per-formance, since thinner films (5 and 15 nm) are mainly CoO (as observed in Fig. 1b), whereas thicker films are a mixture of Co$_3$O$_4$ and CoO phases (36 nm) or predominantly Co$_3$O$_4$ (229 nm). While CoO can readily reduce to metallic Co by applying a negative voltage, the Co$_3$O$_4$ phase (which contains a mixture of Co^{2+} and Co^{3+} cations) can reduce either to metallic

Co (Co^0) or undergo a partial reduction of the oxidation state (from Co^{3+} to Co^{2+}), resulting in a mixture of metallic Co + CoO, as was reported in previous works.[35] This also limits the amount of generated magnetic moment in the thicker films. The slightly weaker Co–O bond in CoO compared with Co$_3$O$_4$ also indicates that, under equivalent applied voltages, O magneto-ionics is faster in CoO than in Co$_3$O$_4$.[54–56]

The coercivity increases with actuation time for all films, reaching a maximum and then slightly decreasing as the actuation time is further increased (Fig. 3b) This is visible for all films except the 230 nm one, where the slight decrease of H_C would pressumably occur at higher actuation times. Interestingly, H_C and also the actuation time at which peak H_C is reached both increase for larger film thickness. This can be explained by the way Co clusters are generated during magneto-ionic actuation (Fig. 4a and b) and the well-known size dependence of coercivity in ferromagnetic particles (i.e., H_C is known to exhibit a maximum as a function of particle size).[57] First, the system is paramagnetic ($t = t_0$). Short actua-tion times generate small Co clusters, sparsely embedded in the paramagnetic oxide matrix after some oxygen is removed. These clusters are likely to be superparamagnetic due to their reduced size, with H_C nearly negligible. As the actuation time
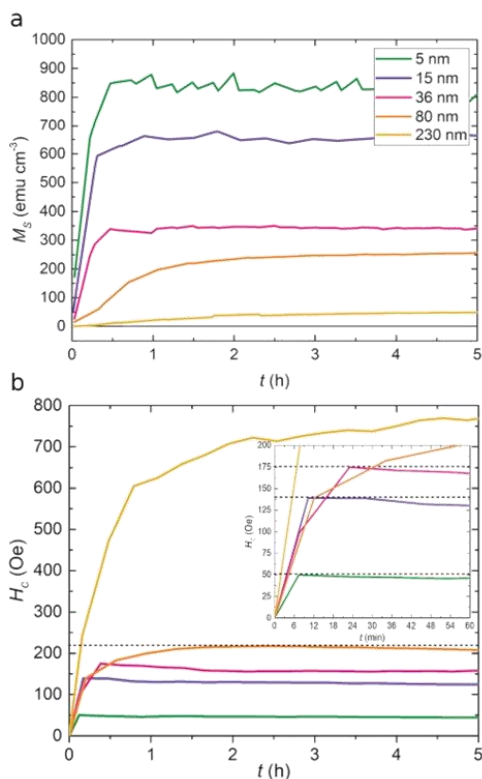
58

Fig. 3 Time evolution of (a) the saturation magnetization (M_S) and (b) the coercivity (H_C) for the various cobalt oxide film thicknesses with a zoom in corresponding to the first hour of time evolution of H_C.
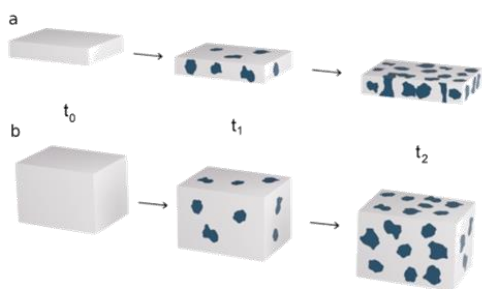

Fig. 4 Schematics of the evolution of the size and density of magneto-ionically generated Co clusters (dark regions) for a thin (a) and a thick (b) cobalt oxide film, respectively.

increases (*e.g.*, $t = t_1$), the Co clusters increase in size and eventually become single-domain ferromagnetic particles (with increasing H_C). For a fixed actuation time, the density of Co clusters is larger in thinner films, as evidenced by the larger M_S (Fig. 4a). For longer times ($t = t_2$), the size of the clusters increases, and they eventually become multi-domain (H_C decreases from the single-domain peak). This is likely to happen faster for thinner films, where the magneto-ionic effects are more pronounced. In thinner films, the inter-cluster distance also decreases (Fig. 4a), thus increasing the strength of dipolar interactions, which also tend to reduce H_C due to the collective switching of the magnetization in these interacting clusters. For Co, the single domain state is expected at 70 nm.[58] For a given ($t = t_2$) (where H_C already decreases in thinner films), Co clusters remain small and isolated (*i.e.*, with weaker dipolar interactions) in thicker films (Fig. 4b – t_2). This allows H_C to still further increase by subjecting the film to the action of voltage for longer times, thus explaining the shift in the maximum of H_C with actuation time shown in Fig. 3b. The analysis of HRTEM images of voltage-actuated thin Co oxide films (around 25 nm) reveals a higher density of Co clusters (Fig. S3†) than in thick (>100 nm) Co oxide films treated in a similar way.[35] The Co cluster size is in both cases in the range 3–6 nm. These observations are in qualitative agreement with the cartoon provided in Fig. 4 which explains the trends in coercivity as a function of film thickness and voltage application time.

To better assess the magneto-ionic effects during the first stages of voltage application, *M vs.* time measurements under −50 V bias were performed while applying a constant magnetic field of 10 kOe (large enough to keep the generated ferromagnetic counterparts in a magnetically saturated state). This allows a more precise calculation of the activation time (*i.e.*, the time required to achieve a measurable generated magnetic moment, which in our setup is around 1 μemu), as well as the real magneto-ionic rate. As seen in Fig. 5a, the M_S reached after 33 minutes is, for all samples, approximately the same as the one at the end of the first loop shown in Fig. 2. However, while M_S increases quickly in the thinner films (the activation time is lower than 1 second for the 5 nm cobalt oxide film), it takes between 10–100 s to reach a measurable M_S value in the thickest films.

Table 1 summarizes the steady-state magnetic properties (H_C, M_R, M_S and M_R/M_S, where M_R is the remanent magnetization and M_R/M_S the squareness ratio) of each film after long-term voltage actuation (as extracted from Fig. 2 and 5). The table also shows the maximum magneto-ionic motion rates obtained from the time derivative of the saturation magnetization (*i.e.*, $(dM_S/dt)_{max}$ from Fig. S5†). The achieved magneto-ionic rates are drastically enhanced when the film thickness is reduced, from 0.5 emu cm^{-3} min^{-1} (for the 230 nm-thick film) to 67 emu cm^{-3} min^{-1} (for the 5 nm-thick film), approximately 3 times faster than that previously observed in 130 nm Co$_3$O$_4$ films.[37]

Taking advantage of their fast magneto-ionic response, the thinnest cobalt oxide films (5 nm) were further investigated under pulsed voltage sequences, revealing remarkable neuro-

59
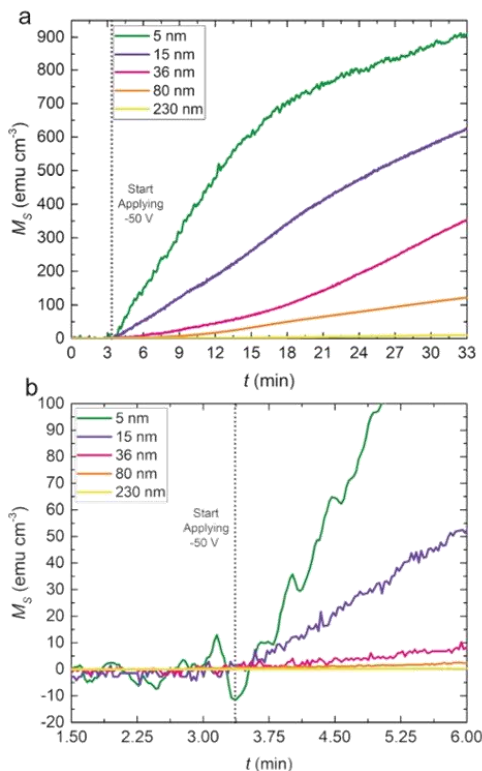
Fig. 5 (a) Time evolution of saturation magnetization (M_S) as a function of time for variable cobalt oxide film thickness, acquired while applying an in-plane magnetic field of 10 kOe. (b) Zoom in of the initial stages of magnetization generation to better illustrate the dissimilar activation times of the films.

($\Delta V = -50$ V). In contrast, the long-term M_S reached under 1 Hz pulsing is significantly lower (Fig. 6a). To understand this effect, the recovery curves (*i.e.*, M_S *vs.* time at $\Delta V = 0$ V acquired after the measurements in Fig. 6a) were also recorded. A tendency for M_S to decrease with time is observed in all samples, akin to a forgetting neuromorphic function (Fig. 6b). However,
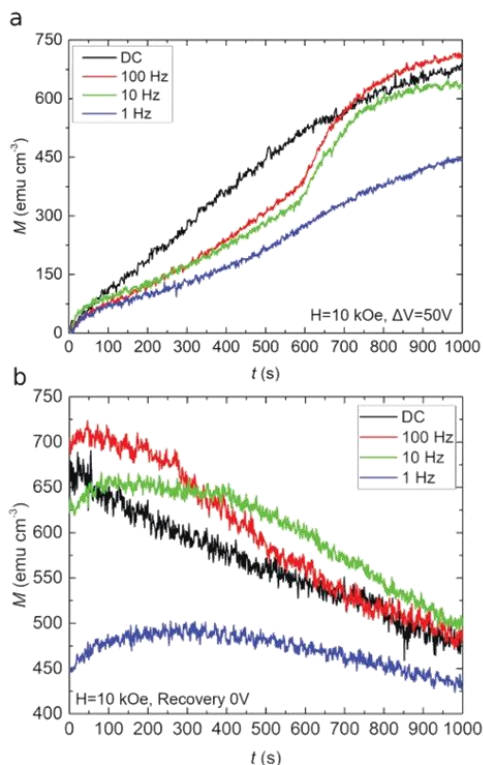
Fig. 6 Time evolution of M_S while applying an in-plane magnetic field of 10 kOe. (a) M_S *vs. t* during static ($\Delta V_{DC} = -50$ V) and dynamic (pulsed) voltage actuation (applying −50 V/0 V at frequencies of 1 Hz, 10 Hz and 100 Hz). (b) shows the recovery experiments, while measuring M_S as a function of time with $\Delta V = 0$ V.

morphic functionalities. In particular, non-linear cumulative magneto-ionic effects (*i.e.*, learning neuromorphic capabilities) were induced in these films by subjecting them to −50 V/0 V pulse waves at frequencies ranging from 1 to 100 Hz. However, these results are not as one would anticipate *a priori*. For example, the M_S values obtained under 10 and 100 Hz pulsing are similar to those obtained using static voltage conditions

Table 1 Steady magnetic properties upon voltage actuation. H_C, M_S and M_R are extracted from Fig. 2, whereas the magneto-ionic rates and activation times are extracted from Fig. 5 and S5†

| Thickness (nm)	H_C (Oe)	M_S (emu cm^{-3})	M_R (emu cm^{-3})	M_R/M_S (%)	Maximum magneto-ionic rate (emu cm^{-3} min^{-1})	Activation time (s)
5 ± 1	47 ± 1	852 ± 9	608 ± 6	71 ± 2	67 ± 2	<10 ± 4
15 ± 1	133 ± 3	660 ± 7	524 ± 5	79 ± 2	27.4 ± 0.8	22 ± 4
36 ± 1	178 ± 5	340 ± 3	337 ± 3	99 ± 2	19.5 ± 0.6	45 ± 4
80 ± 1	218 ± 5	264 ± 3	195 ± 2	74 ± 2	6.3 ± 0.2	52 ± 4
230 ± 1	782 ± 10	50.4 ± 0.5	23.2 ± 0.3	46 ± 1	0.52 ± 0.06	65 ± 4

60

while M_S steadily decreases with time after DC voltage actuation (suggesting a progressive re-oxidation of the magneto-ionically generated Co clusters), more complex dependencies are obtained after pulsed-voltage actuation. After DC voltage actuation, the re-oxidation process (partial recovery) is progressive and tends to stabilize after t = 1000 s; this is also the case when the pulsed voltage actuation is fast (*i.e.*, f = 100 Hz). However, when the actuation frequency is slower (*i.e.*, f = 1 Hz), the decrease of M_S with time is less obvious. This suggests that two-way O^{2-} ion migration effects (from the sample to the electrolyte and *vice versa*) may occur simultaneously once dynamic voltage actuation has stopped. In fact, at f = 1 Hz, partial recovery can also take place during the learning segment, during each of the pulse half-cycles when ΔV = 0. This explains why the increase of M_S under f = 1 Hz pulsing is less than samples treated under DC, 10 Hz pulsing, and 100 Hz pulsing (Fig. 6a), evidencing a trade-off between magnetization generation (ΔV = −50 V, voltage ON) and magnetization depletion due to partial recovery (ΔV = 0 V, voltage OFF) that scales with pulse duration.

Importantly, these experiments reveal that magneto-ionic motion can be induced in cobalt oxide films with pulses of 100 Hz, *i.e.*, with activation times of the order of 10^{-2} s. This is significantly faster than what is reported in most works on magneto-ionics relying on room-temperature O^{2-} ion

migration,[20,21,24,35] and approaches the magneto-ionic rates reported in some H^+ magneto-ionic studies.[33,34]

The effects of recovery are also evident by measuring two consecutive hysteresis loops, under ΔV = 0 V, after actuating the cobalt oxide films for 1000 s under DC and pulsed conditions (Fig. 7). Large recovery effects are observed after DC actuation, where M progressively decreases with time during the first and second hysteresis loops. The recovery decreases with decreasing pulse frequency. However, M reduces to a much lesser extent after actuation using voltage pulses of 1 Hz. This is in agreement with the results of Fig. 6b and can be understood as the result of partial recovery taking place during the OFF periods of magneto-ionic experiments at 1 Hz. For higher frequencies, the trade-off between magnetization generation (voltage ON) and magnetization depletion due to partial recovery (voltage OFF) is shifted towards the former, resulting in a larger 'learning' capacity and a reduced 'forgetting' process.

These results provide evidence that magneto-ionic systems can emulate potentiation or 'learning' functionalities. Similar to the way the human brain works, repeated spiking (*i.e.*, high frequency voltage pulsing) allows for information retention, exhibiting spike-timing-dependent plasticity (*i.e.*, 'learning') analogous to the magneto-ionic generation of magnetization upon dynamic actuation.
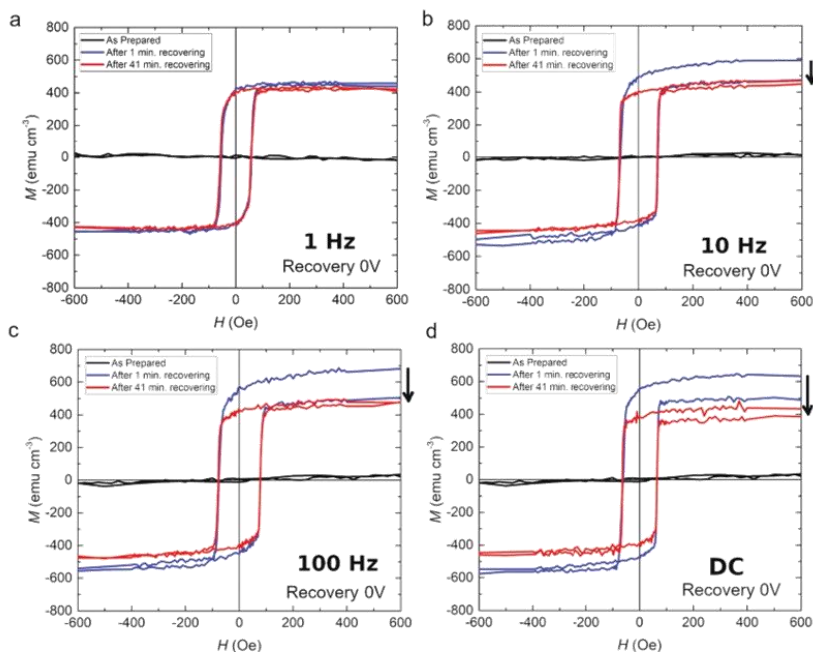
Fig. 7 Magnetic recovery effects evidenced by measuring two consecutive hysteresis loops after having actuated the cobalt oxide films for 1000 s using 50 V/0 V voltage pulses at frequencies of (a) 1 Hz, (b) 10 Hz and (c) 100 Hz. (d) the same recovery experiment after applying a DC voltage of −50 V for 1000 s.
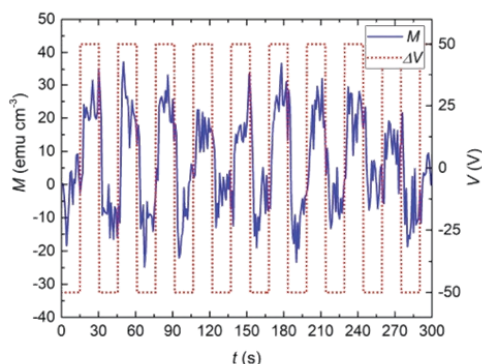
Fig. 8 Magneto-ionic cyclability of the cobalt oxide 5 nm-thick film under −50 V/+50 V voltage pulses of 15 s duration each, assessed from in-plane magnetic measurements while applying a magnetic field of 10 kOe. The superposition of the time evolution of the applied voltage (red discontinuous curve) and the magnetic moment (in blue) for the cobalt oxide film.

To examine the reliability of the observed magneto-ionic effects in terms of endurance and cyclability, voltage pulses of −50 V and +50 V were repeatedly applied to the 5 nm-thick cobalt oxide film, 15 s in duration (sufficient to ensure measurable generation and suppression of the magnetization). The time dependence of the magnetic moment (m) is plotted in Fig. S6† together with the same kind of measurement performed on a reference Si/Ti/Cu sample (without the cobalt oxide film). While clear changes are observed in the cobalt oxide film (blue curve), only non-periodic noise is observed in the reference substrate, thus confirming that the measured changes in M are not an artifact of the experimental setup, but a truly magneto-ionic effect. Remarkably, from the total m generated in the first cycle (4.42×10^{-6} emu), one can calculate the amount of Co generated. This magnetic moment corresponds to a total effective thickness of 0.89 nm of Co is created. In other words, about 18% of the pristine cobalt oxide is transformed to metallic Co during the first voltage pulse. This is much larger than the amount of Co generated in thicker films after long-term voltage application, which was calculated to be 6% in our previous works.[35] Fig. 8 shows the normalized magnetic moment (*i.e.*, M) together with the alternating voltage actuation as function of time. From Fig. 8 we can further resolve the activation time for magneto-ionic effect and it is down to <5 seconds (in agreed with Table 1).

4. Conclusions

Our results reveal that the strength of magneto-ionic effects generated in electrolyte-gated paramagnetic cobalt oxide films exhibit a strong film-thickness dependence. After long-term application of a sufficiently strong DC voltage ($\Delta V = -50$ V),

the generated magnetization in ultra-thin (5 nm) cobalt oxide films is almost 17 times larger than that of thick (230 nm) films. In turn, much faster magneto-ionic rates are obtained in the thinnest films, by a factor 134 times larger in the 5 nm films than for 230 nm films. Remarkably, prominent cumulative magneto-ionic effects (emulating potentiation and plasticity effects of biological synapses) can be obtained by applying pulsed voltages. During dynamic experiments (*i.e.*, using −50 V/0 V square voltage pulses at frequencies in the range 1 Hz–100 Hz), the generated magnetization is smaller for lower frequencies. This can be understood by considering the interplay between potentiation and M depletion effects that occurs during the ON and OFF time periods at sufficiently slow frequencies. Interestingly, for the thin 5 nm cobalt oxide films, transitions from paramagnetic to ferromagnetic states are generated in sub-second time intervals. Cumulative magneto-ionic effects at 100 Hz indicate that activation times are on the order of 10^{-2} s in the thinner films, among the fastest reported so far in magneto-ionic systems relying on O^{2-} ion migration. Our results represent an important contribution towards the applicability of magneto-ionics in practical applications such as neuromorphic computing, which operate at speeds similar to the ones achieved in this work.[59]

Conflicts of interest

There are no conflicts to declare.

Acknowledgements

References

1 M. Skipper, *Nature*, 2018, **554**, 145–146.
2 X. Xu, Y. Ding, S. X. Hu, M. Niemier, J. Cong, Y. Hu and Y. Shi, *Nat. Electron.*, 2018, **1**, 216–222.
3 S. Kasap and P. Capper, *Springer Handbook of Electronic and Photonic Materials*, Springer Handbooks, 2nd edn, 2017, pp. 1–21536.
4 O. Vaughan, *Nat. Electron.*, 2018, **1**, 205.

5 W. A. Wulf and S. A. McKee, *ACM SIGARCH Comput. Archit. News*, 1995, vol. 23, pp. 20–24.

6 D. Ielmini and S. Ambrogio, *Nanotechnology*, 2020, **31**, 092001.

7 R. Islam, H. Li, P.-Y. Chen, W. Wan, H.-Y. Chen, B. Gao, H. Wu, S. Yu, K. Saraswat and H.-S. P. Wong, *J. Phys. D: Appl. Phys.*, 2019, **52**, 113001.

8 J. Park, *Electronics*, 2020, **9**, 1–16.

9 C. D. James, J. B. Aimone, N. E. Miner, C. M. Vineyard, F. H. Rothganger, K. D. Carlson, S. A. Mulder, T. J. Draelos, A. Faust, M. J. Marinella, J. H. Naegle and S. J. Plimpton, *Biol. Inspired Cogn. Archit.*, 2017, **19**, 49–64.

10 R. Douglas, M. Mahowald and C. Mead, *Annu. Rev. Neurosci.*, 1995, **18**, 255–281.

11 W. Zhang, R. Mazzarello, M. Wuttig and E. Ma, *Nat. Rev. Mater.*, 2019, **4**, 150–168.

12 M. A. Galin, E. A. Borodianskyi, V. V. Kurin, I. A. Shereshevskiy, N. K. Vdovicheva, V. M. Krasnov and A. M. Klushin, *Phys. Rev. Appl.*, 2018, **9**, 54032.

13 P. Gkoupidenis, N. Schaefer, B. Garlan and G. G. Malliaras, *Adv. Mater.*, 2015, **27**, 7176–7180.

14 M. Zahedinejad, A. A. Awad, S. Muralidhar, R. Khymyn, H. Fulara, H. Mazraati, M. Dvornik and J. Åkerman, *Nat. Nanotechnol.*, 2020, **15**, 47–52.

15 J. Torrejon, M. Riou, F. A. Araujo, S. Tsunegi, G. Khalsa, D. Querlioz, P. Bortolotti, V. Cros, K. Yakushiji, A. Fukushima, H. Kubota, S. Yuasa, M. D. Stiles and J. Grollier, *Nature*, 2017, **547**, 428–431.

16 V. Milo, C. Zambelli, P. Olivo, E. Pérez, M. K. Mahadevaiah, O. G. Ossorio, C. Wenger and D. Ielmini, *APL Mater.*, 2019, **7**, 081120.

17 D. Ielmini, Z. Wang and Y. Liu, *APL Mater.*, 2021, **9**, 050702.

18 J. Del Valle, J. G. Ramírez, M. J. Rozenberg and I. K. Schuller, *J. Appl. Phys.*, 2018, **124**, 211101.

19 C. Song, B. Cui, F. Li, X. Zhou and F. Pan, *Prog. Mater. Sci.*, 2017, **87**, 33–82.

20 A. Molinari, H. Hahn and R. Kruk, *Adv. Mater.*, 2019, **31**, 1806662.

21 C. Navarro-Senent, A. Quintana, E. Menéndez, E. Pellicer and J. Sort, *APL Mater.*, 2019, **7**, 030701.

22 Y. Cheng, B. Peng, Z. Hu, Z. Zhou and M. Liu, *Phys. Lett. A*, 2018, **382**, 3018–3025.

23 R. Mishra, D. Kumar and H. Yang, *Phys. Rev. Appl.*, 2019, **11**, 054065.

24 M. Nichterwitz, S. Honnali, M. Kutuzau, S. Guo, J. Zehner, K. Nielsch and K. Leistner, *APL Mater.*, 2021, **9**, 030903.

25 W. Kleemann and C. Binek, *Springer Tracts Mod. Phys.*, 2013, **246**, 163–187.

26 J. M. Hu, C. W. Nan and L. Q. Chen, *Natl. Sci. Rev.*, 2019, **6**, 621–624.

27 D. Hayakawa, A. Obinata, K. Miwa, S. Ono, T. Hirai, T. Koyama and D. Chiba, *AIP Adv.*, 2016, **6**, 115305.

28 W. Lin, N. Lei, N. Vernier, G. Agnus, J. P. Adam, S. Eimer, T. Devolder, P. Lecoeur and D. Ravelosona, *Thin Solid Films*, 2013, **533**, 70–74.

29 Z. Hu, X. Wang, T. Nan, Z. Zhou, B. Ma, X. Chen, J. G. Jones, B. M. Howe, G. J. Brown, Y. Gao, H. Lin, Z. Wang, R. Guo, S. Chen, X. Shi, W. Shi, H. Sun, D. Budil, M. Liu and N. X. Sun, *Sci. Rep.*, 2016, **6**, 32408.

30 W. Du, M. Liu, H. Su, H. Zhang, B. Liu, H. Meng, G. Xu, R. Peng and X. Tang, *Appl. Phys. Lett.*, 2020, **117**, 222401.

31 D. A. Links, *Nanoscale*, 2012, **4**, 3218–3227.

32 U. Bauer, L. Yao, A. J. Tan, P. Agrawal, S. Emori, H. L. Tuller, S. Van Dijken and G. S. Beach, *Nat. Mater.*, 2015, **14**, 174–181.

33 A. J. Tan, M. Huang, C. O. Avci, F. Büttner, M. Mann, W. Hu, C. Mazzoli, S. Wilkins, H. L. Tuller and G. S. Beach, *Nat. Mater.*, 2019, **18**, 35–41.

34 K. Y. Lee, S. Jo, A. J. Tan, M. Huang, D. Choi, J. H. Park, H. I. Ji, J. W. Son, J. Chang, G. S. Beach and S. Woo, *Nano Lett.*, 2020, **20**, 3435–3441.

35 A. Quintana, E. Menéndez, M. O. Liedke, M. Butterling, A. Wagner, V. Sireus, P. Torruella, S. Estradé, F. Peiró, J. Dendooven, C. Detavernier, P. D. Murray, D. A. Gilbert, K. Liu, E. Pellicer, J. Nogues and J. Sort, *ACS Nano*, 2018, **12**, 10291–10300.

36 J. de Rojas, A. Quintana, A. Lopeandía, J. Salguero, B. Muñiz, F. Ibrahim, M. Chshiev, A. Nicolenco, M. O. Liedke, M. Butterling, A. Wagner, V. Sireus, L. Abad, C. J. Jensen, K. Liu, J. Nogués, J. L. Costa-Krämer, E. Menéndez and J. Sort, *Nat. Commun.*, 2020, **11**, 5871.

37 J. de Rojas, A. Quintana, A. Lopeandía, J. Salguero, J. L. Costa-Krämer, L. Abad, M. O. Liedke, M. Butterling, A. Wagner, L. Henderick, J. Dendooven, C. Detavernier, J. Sort and E. Menéndez, *Adv. Funct. Mater.*, 2020, **30**, 2003704.

38 L. Herrera Diez, R. Kruk, K. Leistner and J. Sort, *APL Mater.*, 2021, **9**, 050401.

39 K. Zheng, F. Sun, J. Zhu, Y. Ma, X. Li, D. Tang, F. Wang and X. Wang, *ACS Nano*, 2016, **10**, 7792–7798.

40 D. A. Gilbert, A. J. Grutter, E. Arenholz, K. Liu, B. J. Kirby, J. A. Borchers and B. B. Maranville, *Nat. Commun.*, 2016, **7**, 12264.

41 D. A. Gilbert, J. Olamit, R. K. Dumas, B. J. Kirby, A. J. Grutter, B. B. Maranville, E. Arenholz, J. A. Borchers and K. Liu, *Nat. Commun.*, 2016, **7**, 11050.

42 M. Cialone, A. Nicolenco, S. Robbennolt, E. Menéndez, G. Rius and J. Sort, *Adv. Mater. Interfaces*, 2021, **8**, 2001143.

43 J. M. Hu and C. W. Nan, *APL Mater.*, 2019, **7**, 080905.

44 K. L. Wang, H. Lee and P. K. Amiri, *IEEE Trans. Nanotechnol.*, 2015, **14**, 992–997.

45 H. Cai, W. Kang, Y. Wang, L. A. De Barros Naviner, J. Yang and W. Zhao, *Appl. Sci.*, 2017, **7**, 929.

46 K. Jabeur, G. Pendina and G. Prenat, *Electr. Electron. Eng. An Int. J.*, 2017, **6**, 1–9.

47 S. Manipatruni, D. E. Nikonov, C. C. Lin, T. A. Gosavi, H. Liu, B. Prasad, Y. L. Huang, E. Bonturim, R. Ramesh and I. A. Young, *Nature*, 2019, **565**, 35–42.

48 J. de Rojas, J. Salguero, F. Ibrahim, M. Chshiev, A. Quintana, A. Lopeandia, M. O. Liedke, M. Butterling, E. Hirschmann, A. Wagner, L. Abad, J. L. Costa-Krämer, E. Menéndez and J. Sort, *ACS Appl. Mater. Interfaces*, 2021, **13**, 30826–30834.

63

49 A. Barla, J. Nicolás, D. Cocco, S. M. Valvidares, J. Herrero-Martín, P. Gargiani, J. Moldes, C. Ruget, E. Pellegrin and S. Ferrer, *J. Synchrotron Radiat.*, 2016, **23**, 1507–1517.

50 F. C. Wu, S. W. Hsu, H. L. Cheng, W. Y. Chou and F. C. Tang, *J. Phys. Chem. C*, 2013, **117**, 8691–8696.

51 Q. He, Q. Li, S. Khene, X. Ren, F. E. López-Suárez, D. Lozano-Castelló, A. Bueno-López and G. Wu, *J. Phys. Chem. C*, 2013, **117**, 8697–8707.

52 T. Takada, Y. Bando, N. Yamamoto and K. Nagasawa, *Jpn. J. Appl. Phys.*, 1969, **8**, 619–619.

53 K. M. Nam, J. H. Shim, D. W. Han, H. S. Kwon, Y. M. Kang, Y. Li, H. Song, W. S. Seo and J. T. Park, *Chem. Mater.*, 2010, **22**, 4446–4454.

54 R. Robie and B. S. Hemingway, *Thermodynamic Properties of Minerals and Related Substances at 298.15K and 1 Bar*, 1995, pp. 1–461.

55 L. Glasser and D. A. Sheppard, *Inorg. Chem.*, 2016, **55**, 7103–7110.

56 M. W. Chase, *J. Phys. Chem. Ref. Data, Monogr.*, 1998, **4**, 1–1951.

57 E. F. Kneller and F. E. Luborsky, *J. Appl. Phys.*, 1963, **34**, 656–658.

58 D. L. Leslie-Pelecky and R. D. Rieke, *Chem. Mater.*, 1996, **8**, 1770–1783.

59 J. J. Harris, R. Jolivet and D. Attwell, *Neuron*, 2012, **75**, 762–777.

64

Dynamic electric-field-induced magnetic effects in cobalt oxide thin films: towards magneto-ionic synapses

S. Martins,[a] J. de Rojas, [a] Z. Tan, [a] M. Cialone,[b] A. Lopeandia, [c] J. Herrero-Martín, [d] J. L. Costa-Kramer,[e] E. Menéndez,* [a] Jordi Sort* [a,f]

[a.] Departament de Física, Universitat Autònoma de Barcelona, E-08193 Cerdanyola del Vallès, Spai; *Email: Enric.Menendez@uab.cat, Jordi.Sort@uab.cat}
[b.] CNR-SPIN Genova, C.so F. M. Perrone 24, Genova, 16152, Italy
[c.] Catalan Institute of Nanoscience and Nanotechnology (ICN2), CSIC and BIST, Campus UAB, Cerdanyola del Vallès, E-08193 Barcelona, Spain
[d.] ALBA Synchrotron Light Source, 08290 Cerdanyola del Vallès, Spain
[e.] IMN-Instituto de Micro y Nanotecnología (CNM-CSIC), Isaac Newton 8, PTM, 28760 Tres Cantos, Madrid, Spain
[f.] Institució Catalana de Recerca i Estudis Avançats (ICREA), Pg. Lluís Companys 23, E-08010 Barcelona, Spain

A- Experimental Setup
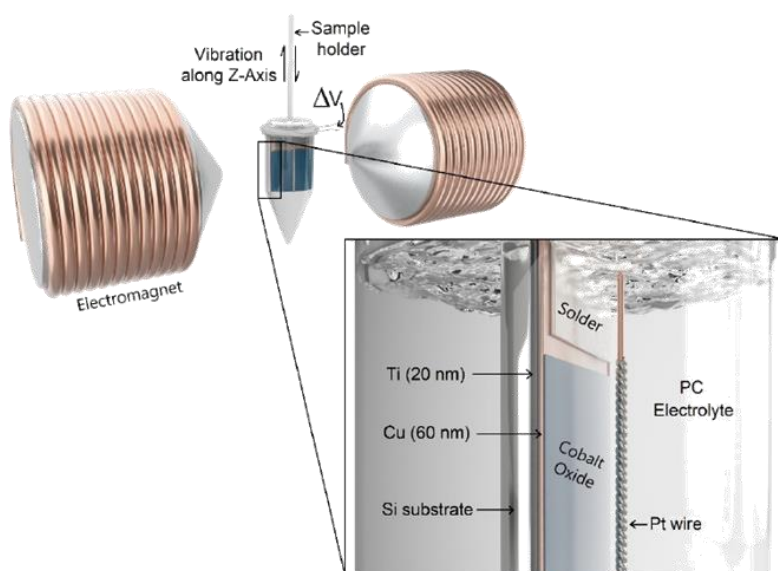
Fig. S1. Schematic showing the home-made electrolytic cell used for the of voltage actuation and magnetoelectric characterization by VSM.

65
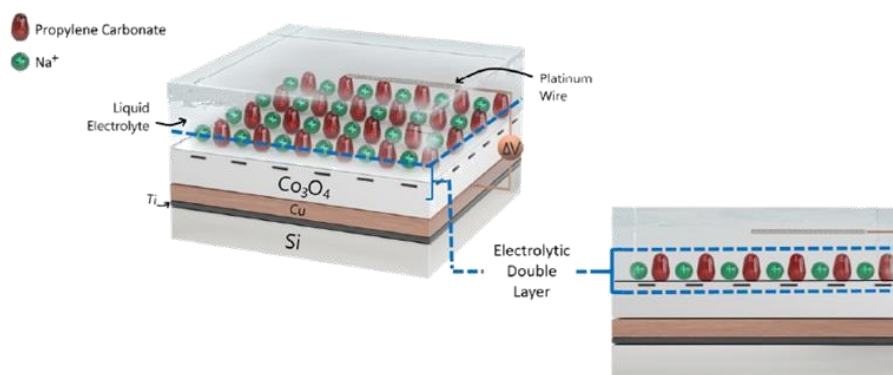
Fig. S2. Schematic of the EDL formation. Note that, for simplicity, the Na$^+$ ions and the propylene carbonate changes are drawn separately although, most likely, Na$^+$ ions become solvated when dissolved in the electrolyte.
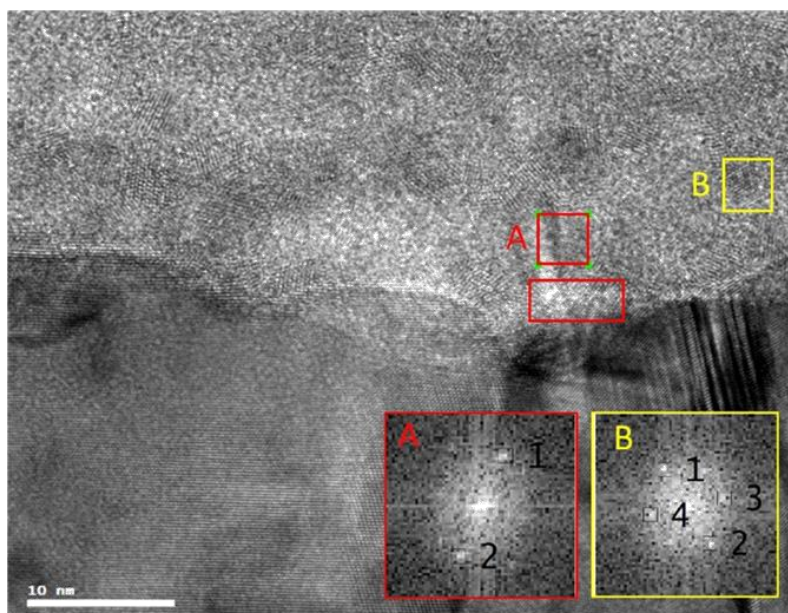
Fig S3. HRTEM image of a thin (25 nm) CoOx film treated with high negative voltage (−50 V) for 30 min. The squares A and B indicate crystallites whose lattice cell parameter matches the position of HCP-Co as evidenced by the fast Fourier transforms presented at the bottom left corner of the image: "1" and "2" represent an interplanar distance of 1.90 Å which matches the (101) direction of HCP-Co and "3" and "4" represent an interplanar distance of 2.15 Å which matches the (100) direction of HCP-Co. The majority of the other crystals seen by HRTEM correspond to either CoO or Co_3O_4.

B- Further Magnetoelectric measurements
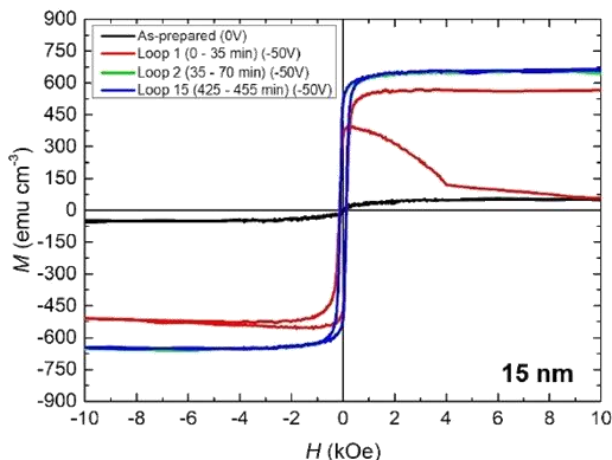
Fig. S4. Dependence of magneto-ionic effects on the cobalt oxide film thickness. Panels a–d show consecutive hysteresis loops corresponding to cobalt oxide films of 15 nm thickness, respectively, upon electrolyte gating ($\Delta V = -50$ V) acquired using a vibrating sample magnetometer (magnetic field applied in-plane).
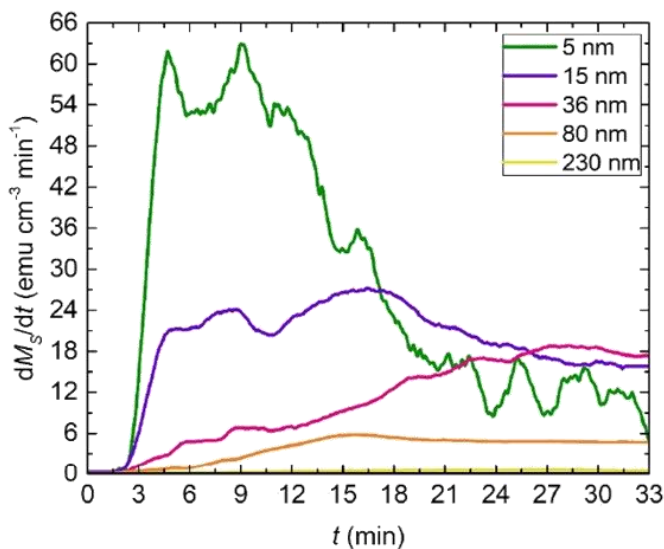
Fig. S5. (a) Time evolution of derivative of the saturation magnetization (dM_S/dt) as a function of the cobalt oxide film thickness, acquired while applying an in-plane magnetic field of 10 kOe.

67
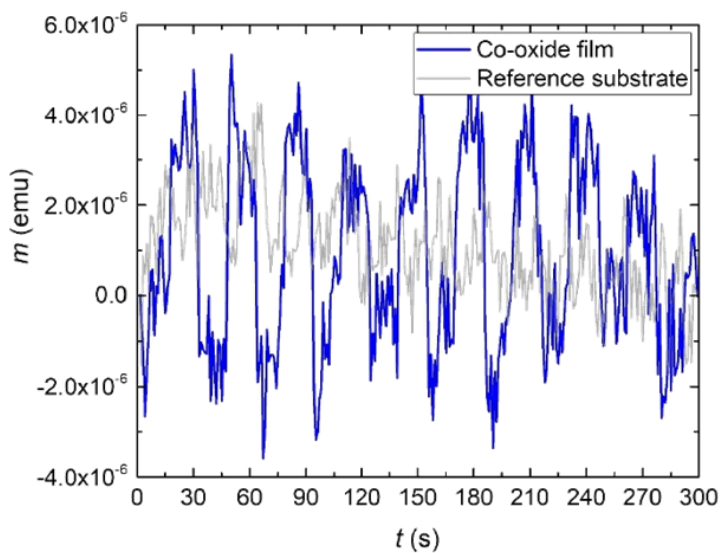
Fig. S6. Magnetic recovery effects evidenced by measuring two consecutive hysteresis loops after having actuated the cobalt oxide films for 1000 s using −50V/0V voltage pulses at frequencies of (a) 1 Hz, (b) 10 Hz and (c) 100 Hz. (d) the same recovery experiment after applying a DC voltage of −50V for 1000 s.

3.2. Enhancing magneto-ionic effects in cobalt oxide films by electrolyte engineering

Sofia Martins, *[a] Zheng Ma,[a] Xavier Solans-Monfort,[b] Mariona Sodupe,[b] Luis Rodriguez-Santiago,[b] Enric Menéndez[a], Eva Pellicer*[a] and Jordi Sort[a,c]

[a]Departament de Física, Universitat Autònoma de Barcelona, E-08193 Cerdanyola del Vallès, Spain. E-mail: Enric.Menendez@uab.cat, Jordi.Sort@uab.cat

[b]Departament de Química, Universitat Autònoma de Barcelona, E-08193 Cerdanyola del Vallès, Spain

[c]Institució Catalana de Recerca i Estudis Avançats (ICREA), Pg. Lluís Companys 23, E-08010 Barcelona, Spain
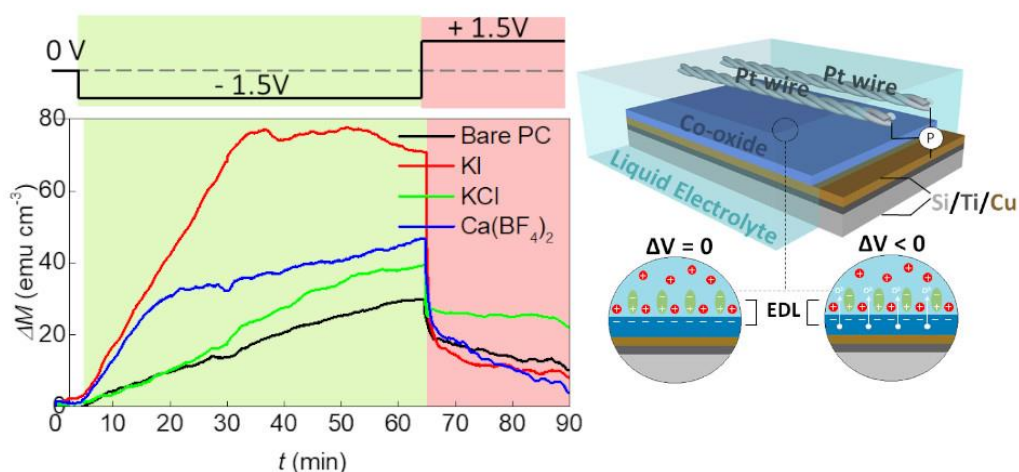
Despite the previous study showed that VCM of Co-oxide films with sub-10 s magneto-ionics response by pulsing voltage is feasible, room temperature magneto-ionics is still too slow for useful applications. Hence, further improvements are required in terms of higher speeds and the need to reduce the applied voltages (which are often as large as −50 V). In this publication, we show that adding inorganic salts to anhydrous PC, such as potassium iodide (KI), potassium chloride (KCl), and calcium tetrafluoroborate ($Ca(BF_4)_2$, improves oxygen motion in 15 nm-thick cobalt oxide films. Specially for KI-containing PC, a 35-fold increase of the magneto-ionic rate was observed as compared to plain PC, and importantly, under a relatively low bias value of −1.5 V. Experimental data is supplemented with *ab initio* molecular dynamics simulations, which help understanding why the effects observed for KI are greater than for KCl, which is a result one would not expect a priori.

Nanoscale Horizons

The home for rapid reports of exceptional significance in nanoscience and nanotechnology

ROYAL SOCIETY
OF CHEMISTRY
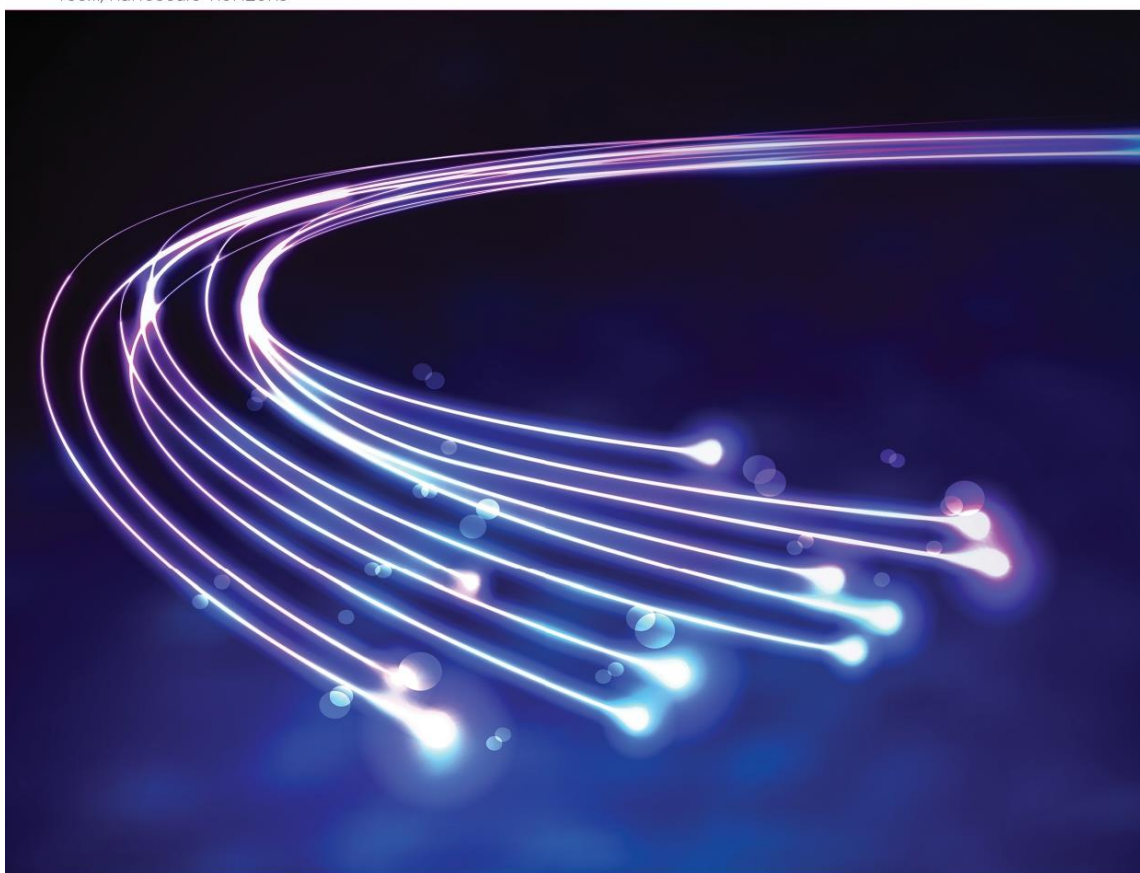
NCNST

© Yienkeat/Shutterstock

71

## COMMUNICATION

Check for updates

Enhancing magneto-ionic effects in cobalt oxide films by electrolyte engineering†

Sofia Martins, [ID] *[a] Zheng Ma, [ID] [a] Xavier Solans-Monfort, [ID] [b] Mariona Sodupe, [ID] [b] Luis Rodriguez-Santiago, [ID] [b] Enric Menéndez, [ID] [a] Eva Pellicer [ID] *[a] and Jordi Sort [ID] [ac]

Electric-field-driven ion motion to tailor magnetic properties of materials (magneto-ionics) offers much promise in the pursuit of voltage-controlled magnetism for highly energy-efficient spintronic devices. Electrolyte gating is a relevant means to create intense electric fields at the interface between magneto-ionic materials and electrolytes through the so-called electric double layer (EDL). Here, improved magneto-ionic performance is achieved in electrolyte-gated cobalt oxide thin films with the addition of inorganic salts (potassium iodide, potassium chloride, and calcium tetrafluoroborate) to anhydrous propylene carbonate (PC) electrolyte. Ab initio molecular dynamics simulations of the EDL structure show that K^+ is preferentially located on the cobalt oxide surface and KI (when compared to KCl) favors the accumulation of positive charge close to the surface. It is demonstrated that room temperature magneto-ionics in cobalt oxide thin films is dramatically enhanced in KI-containing PC electrolyte at an optimum concentration, leading to 11-fold increase of generated magnetization and 35-fold increase of magneto-ionic rate compared to bare PC.

New concepts

Voltage control of magnetism (VCM) through electric field-induced ion motion, referred to as magneto-ionics, is a cutting-edge research topic since it holds the promise to revolutionize current strategies to enhance energy efficiency in magnetically actuated devices (e.g., micro-electro-mechanical systems, magnetic logics, spintronics, or neuromorphic computing). Modifying the film composition/microstructure or the working conditions are the typical approaches followed in the literature to boost magneto-ionics. However, at present, room temperature oxygen magneto-ionics is still too slow for relevant applications. Increased O^{2-} motion speeds and smaller threshold voltages are highly desirable. Here, we demonstrate that O^{2-} motion in electrolyte-gated cobalt oxide films can be significantly enhanced by suitable 'electrolyte engineering' in films of a few nm in thickness. In particular, inorganic salts (e.g., KI, KCl and $(Ca(BF_4)_2)$), have been added to anhydrous propylene carbonate (PC) to modulate the ionic strength and, in turn, the electric field at the cobalt oxide/electrolyte interface by means of the built-in electric double layer. For KI-containing PC, a 35-fold increase of the magneto-ionic rate is observed compared to plain PC and, importantly, under a relatively low bias value (< -1.5 V), much lower than the voltage values needed so far to induce magneto-ionics in this kind of systems.

Introduction

Advancements in further downsizing the next-generation spintronic devices while minimizing their Joule power dissipation have been remarkable in the last decades.[1,2] Voltage control of magnetism (VCM) promises great potential to reduce the energy demands of spintronics. As such, magnetoelectric (ME) effects, related to the coupling between magnetic and electric behaviors in matter, have been proposed as one of the most promising avenues to realize the manipulation of

magnetic properties by an electric field. This can be accomplished, to some extent, in ME multiferroics, where ferroelectricity and magnetism coexist and are usually coupled. Nevertheless, several challenges must be overcome, such as the scarcity of intrinsic single-phase ME materials, the weak coupling between electric polarization and magnetization at room temperature, and the clamping effects in the case of ME composites (or heterostructured multiferroics). Alternatively, voltage-driven ion motion to tune magnetism (i.e., magneto-ionics) has recently attracted great attention thanks to its ability to considerably modulate magnetic properties, in a permanent manner.[3] In recent years, magneto-ionics has been demonstrated in a wide variety of materials, including both, metals and semiconductors.[4]

Electrolyte-gating through the formation of an electric double layer (EDL) has shown to be a very convenient means to

[a] Departament de Física, Universitat Autònoma de Barcelona, E-08193 Cerdanyola del Vallès, Spain. E-mail: CarlaSofia.Martins@uab.cat, Eva.Pellicer@uab.cat

[b] Departament de Química, Universitat Autònoma de Barcelona, E-08193 Cerdanyola del Vallès, Spain

[c] Institució Catalana de Recerca i Estudis Avançats (ICREA), Pg. Lluís Companys 23, E-08010 Barcelona, Spain

tailor the magnetic properties of magneto-ionic systems. These systems work as electrochemical capacitors (EC), *i.e.*, supercapacitors, thereby involving the formation of an EDL between the solid material and the electrolyte. At least three types of ECs can be distinguished, namely electrical double layer capacitors (EDLC), pseudocapacitors, and a combination of both.[5,6] Whatever the type, ECs refer to a system capable to accumulate electrical charges at the surface of an electrode material in contact with an electrolyte. When voltage is applied to a magneto-ionic material, the electric field causes changes in its saturation magnetization (M_S) or coercivity (H_C), among other magnetic properties, which can be finely tuned based on electrostatic and/or electrochemical mechanisms.[7,8]

According to the different models put in place to explain the concept of EDLs formed at the interface between planar solids and aqueous solutions, the simplest theory states that EDLs form to neutralize the surface charge on the solid material by ions of opposite sign (Helmholtz model). The more elaborated Gouy–Chapman–Stern model (GCS) is currently widely used to describe EDLs. It assumes the occurrence of two layers, one fixed layer next to the electrode surface (Stern layer or Helmholtz region) of opposite charge, and a diffuse layer, wherein ions can move freely. The Stern layer, in turn, is divided into the inner Helmholtz plane (IHP) and the outer Helmholtz plane (OHP). The former has approximately one single ion thickness. Compared to aqueous solutions, studies on the structure of EDL in organic solvents are more limited. Feng *et al.* examined a system made of tetraethylammonium tetrafluoroborate (TEABF$_4$) salt in acetonitrile (CH$_3$CN) and found remarkable contact adsorption of TEABF$_4$ ions to the surface of the electrode and strong layering and orientational ordering of acetonitrile molecules until approx. 1.1 nm into the bulk electrolyte.[9] The EC based on interfacial ion-modulation has attracted much interest because of the giant charge-carrier density accumulation achieved because of the large EDL capacitance. Under electrolyte gating, permanent changes at the surface and the bulk of electrode material are possible, whenever chemical reactions are involved.

Materials such as carbon, metal oxides and nitrides, and conducting polymers have been used in an EC.[5,6] Metal oxides/nitrides such as Co$_3$O$_4$[10–12] and CoN[13,14] are very appealing for magneto-ionics, since they not only store energy like electrostatic carbon materials but can also undergo electrochemical reactions under voltage actuation, eventually leading to a fully reversible transformation from a paramagnetic state (OFF) to a ferromagnetic state (ON), and *vice versa*. This is explained by oxygen and nitrogen motion, respectively, under voltage actuation, the concurrent creation of atomic defects, and the consequent generation of magnetic moment arising from metallic Co.[10–14]

The maximum electric field achievable in ECs is limited by the breakdown voltage of the electrolyte. Four primary classes of electrolyte solutions have been used in EC: organic, aqueous, polymeric and ionic liquid electrolytes. Among organic electrolytes, ACN and propylene carbonate (PC) are the most widely used solvents. ACN presents the ability to solvate large amounts of salts but it is toxic, while PC is more environmentally friendly, offers a wide electrochemical window and operating temperature, as well as conductivity of $1–2 \times 10^{-8}$ Ohm^{-1} cm^{-1}.[5,15,16] Indeed, PC is a dipolar protic solvent with high dielectric constant (64.40 at 25 °C) and a large dipole moment (4.81 D) which has been considered an ideal structureless dielectric to solubilize strong electrolytes for a variety of applications. Since PC has a relatively large dielectric constant, dissolved ionic compounds will be extensively dissociated.

In spite of the achievements with VCM of Co oxide films, room temperature magneto-ionics is still too slow for relevant applications. Even though sub-10 s magneto-ionics has recently been demonstrated by reducing the Co oxide thickness down to 5 nm,[12] further improvements are required to enable magneto-ionics in real devices. In addition, the applied voltages required to observe a remarkable change in the magnetic properties of cobalt oxide were rather large, of the order of -50 V. Recently, we showed that magneto-ionics depends on the electrical properties of the target materials.[4] Here we demonstrate that not only the electrical properties of cobalt oxide are important, but also the composition of the electrolyte. More specifically, its ionic strength also plays a key role in magneto-ionics. In the past years, various salts and additives have been added to solvents to increase the ionic strength of electrolytes for a variety of purposes.[17–19] As the salt concentration is increased, more ions can accumulate in the compact layer of the EDL, reducing the presence of free solvent molecules in the vicinity of the electrode. As a result, the performance of energy storage systems improves.[17,20] This strategy could well work for magneto-ionics, paving the way for higher charge accumulation at the surface of the solid material and, hence, more intense electric fields. To date, different electrolytes have been tested for voltage-driven ion migration and, in some cases, salts were added to the solvent (*e.g.* LiPF$_6$ in dimethyl carbonate/ethylene carbonate mixture) to observe the effects.[7,21,22] In spite of the intensive research carried out in the last decade, studies with complex PC formulations are lacking.

Herein, we have investigated the impact of the addition of inorganic salts, namely potassium iodide (KI), potassium chloride (KCl) and calcium tetrafluoroborate (Ca(BF$_4$)$_2$), to anhydrous PC on the magneto-ionic effects induced in 15 nm-thick Co oxide films. The solubility of KI and KCl in PC at room temperature was reported by Peruzzi *et al.*[23] and that of Ca(BF$_4$)$_2$ in PC was investigated by Forero-Saboya *et al.*[17] (see Experimental section). KCl was primarily chosen as it is the electrolyte support of choice in many electrochemical processes taking place in aqueous solutions. KI was selected as it showed higher solubility in PC and simply implied the replacement of Cl$^-$ by I$^-$. Finally, Ca(BF$_4$)$_2$ was chosen since it is typically dissolved in alkyl carbonates like PC in calcium ion batteries.[24] Our work reveals that improvements in oxygen ion motion[25–27] in cobalt oxide are accomplished by adding these salts to PC. Specifically, the fastest magneto-ionic rate is observed when using PC + 2.5×10^{-4} M KI electrolyte, which is 35 times larger than the rate observed for bare PC electrolyte under -1.5 V.

Moreover, upon biasing Co oxide for one hour, the same PC + 2.5×10^{-4} M KI electrolyte results in the largest generation of magnetization. The process is highly reversible for all added salts since the generated magnetism can be reduced after applying a voltage of opposite polarity (*i.e.*, +1.5 V). The magneto-ionic response of the cobalt oxide films was further studied at varying concentrations of KI dissolved in PC. Our results show that improved magneto-ionics can be achieved by conveniently tuning the EDL strength *via* liquid electrolyte engineering.

Results and discussion

To investigate the magneto-ionic behavior of 15 nm thick Co oxide films in different electrolyte solutions, a home-made electrolytic cell, sketched in Fig. 1(a), was used which allowed to externally polarize the material while recording its magnetic response under in-plane configuration on a vibrating sample magnetometer (VSM). As illustrated in Fig. 1(b), an electrokinetic potential is created at the solid/electrolyte interface under no external electric field applied, considering that EDLs form whenever an electronic conducting material is placed in an electrolyte containing mobile ions.[3] This is of course a very simplistic cartoon because the cobalt oxide film is sketched as if it acquires negative charge while positive charges gather together at the solid/electrolyte interface, which is not necessarily the case. Under electrolyte gating (Fig. 1(c)), specifically when cobalt oxide is negatively polarized, positive ions migrate towards the interface and PC molecules reorganize and rearrange, thus strongly causing a modification of the EDL structure.

The magnetic moment of cobalt oxide in different electrolyte solutions was measured at room temperature under a 10 kOe magnetic field, where the generated ferromagnetic response is saturated. The external voltage was applied *in situ* during the magnetic measurements. Fig. 1(d) presents the time evolution of magnetization change ($\Delta M - t$) for the films actuated in bare PC and PC containing 2.5×10^{-5} M KI, KCl and Ca(BF$_4$)$_2$ electrolytes. In the first stage of the measurements, ΔM continuously increases to around 30 emu cm^{-3} for the bare PC electrolyte while $\Delta V = -1.5$ V is applied for 60 min (*i.e.*, $t = 65$ min) (see the green shaded region in Fig. 1(d)). This indicates the appearance of ferromagnetism in the cobalt oxide. In the second stage (*i.e.*, after applying +1.5 V for 25 min), ΔM sharply drops due to the reversal of the bias polarity, and reaches around 10 emu cm^{-3}. The occurrence of a ferromagnetic-paramagnetic (ON–OFF) transition in the oxide films is related to voltage-induced oxygen ion motion.[10] Several observations can be made from the $\Delta M - t$ curves for electrolytes with different inorganic salts. First, for the PC + KCl electrolyte, ΔM increases at a similar rate as the bare PC one until $t = 20$ min, and it then grows faster and approaches 40 emu cm^{-3} at $t = 65$ min, representing a 33% increase compared to bare PC. Importantly, the initial ΔM change is significantly enhanced with the additions of KI and Ca(BF$_4$)$_2$ into PC, as reflected by the larger slopes of the blue and red curves for $t < 20$ min and $t < 35$ min, respectively. Furthermore, the maximum ΔM values at $t = 65$ min are much higher in the electrolytes containing KI and Ca(BF$_4$)$_2$ than for bare PC and PC + KCl. Remarkably, the maximum ΔM for PC + 2.5 $\times$ 10^{-5} M KI electrolyte is twice higher than that for bare PC (70 emu cm^{-3} *versus* 30 emu cm^{-3}). Finally, the sudden decrease of ΔM when applying voltage of opposite polarity is observed for all the electrolytes. In particular, ΔM drops from around 70 emu cm^{-3} to 10 emu cm^{-3} during the time interval from $t = 65$ min to 70 min for the electrolyte made of
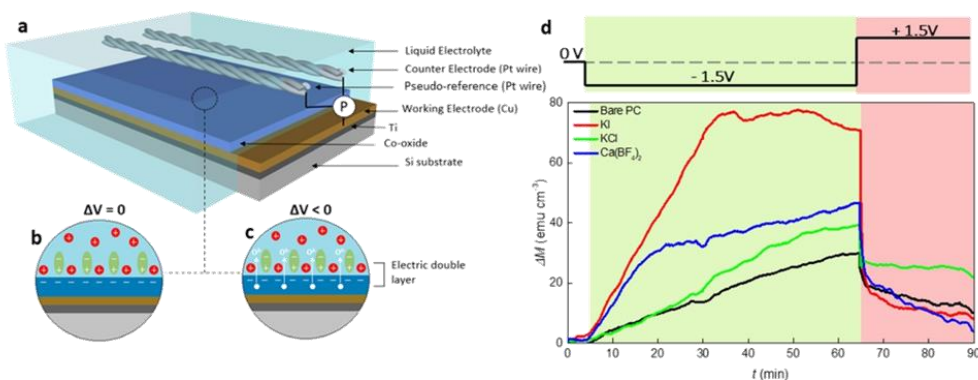
Fig. 1 Magneto-ionic characterization of Co oxide under electrolyte-gating. (a) Schematics of the electrolyte gate process under voltage actuation of a Co oxide film. Possible structure of the EDL under (b) no applied electric field (electrostatic forces), and (c) external polarization (electrochemical reaction). (d) Time evolution of magnetization (ΔM) for bare PC and PC-containing KI, KCl and Ca(BF$_4$)$_2$ salts at equal salt concentration (2.5×10^{-5} M), at -1.5 V for 60 min followed by +1.5 V (as schematically shown in the upper panel). Magnetic measurements were done in-plane while applying an external magnetic field of 10 KOe.

Communication

PC + 2.5 × 10^{-5} M KI. These observations indicate that magneto-ionic effects in cobalt oxide can be substantially improved by electrolyte engineering. It is worth mentioning that the relatively small gating voltage employed in the current study (1.5 V) can produce similar magneto-ionic responses as previous works where we used applied voltages of the order of 25 V or higher for similar Co oxide film thicknesses.[11,12] This decrease in the threshold voltage needed to induce changes in the magnetic properties of the Co oxide can be directly linked to the addition of inorganic salts into PC. Interestingly, although one would expect KCl and KI to yield similar results upon negatively biasing the cobalt oxide film, ΔM was far higher for KI.

To get atomistic insights on the initial cobalt oxide – propylene carbonate + KX (X = Cl, I) interface, *ab initio* molecular dynamics (AIMD) simulations at 300 K were carried out. Co_3O_4 was considered for the simulations. Energies were computed at the PBE-D3+U (U_{eff} = 3.0 eV) without applying any external potential. The statistical analysis was performed on the last 8 (6 depending on the structure) ps of each simulation (see Computational details). We paid attention on the location of KX (X = Cl or I) and thus, two different initial structures were considered for each salt (Fig. S1 of the ESI†). In one case, the two ions were directly interacting with the surface at distances around 2 Å (KX_{Ads}). In the other, the salt was fully solvated by PC molecules (KX_{Sol}). Fig. 2 reports: (a) one representative snapshot of the simulation leading to the most favorable conformation for each salt KCl_{Ads} and KI_{Sol} AIMD, (b) the variation of the surface–ion distances in the simulations leading to the most favorable situation and (c) the energetics of the four AIMD. The variation of the potassium–surface distance, the anion–surface distance and a representative snapshot of the four simulations can be found in Fig. S2, S3 and S4 of the ESI.†

The AIMD simulations starting with the two ions adsorbed on the surface evolved without any relevant variation. All ions remain attached at the surface with average ion⋯surface distances of 2.2, 2.1 and 2.4 Å for K^+, Cl^- and I^-, respectively. In these simulations no significant charge separation is generated, suggesting that almost no positive charge will be accumulated on the Co_3O_4 surface. The simulations starting with the two ions in the solution (KCl_{Sol} and KI_{Sol}) showed a larger reorganization. Regardless of the counter ion, K^+ rapidly becomes adsorbed on the surface with K⋯surface average distances that are only slightly higher than in the KX_{Ads} simulation (2.5–2.6 Å). In contrast, the anions remain in the solution. The Cl^- anion moves around the initial structure with an average surface–Cl^- distance of 6.5 Å. Iodide prefers to move further away from the surface, the resulting surface–anion distances becoming about 9.8 Å. That is, the KX_{Sol} simulations lead to a structure defining an EDL, with a compact positive charge accumulation on Co_3O_4. Comparison between the energetics of the KX_{Ads} and KX_{Sol} simulations rises the different behavior of the anions. For KCl, the configuration in which the two ions are directly adsorbed on the surface is slightly more stable (ΔG = 0.2 eV) than the structure defining the double
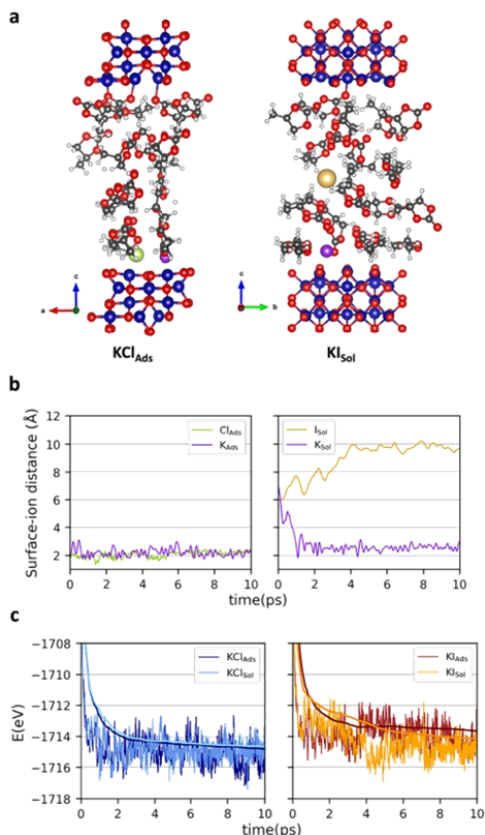

Fig. 2 (a) Representative snapshots of the most favorable KCl_{Ads} and KI_{Sol} AIMD simulations; variation along the AIMD simulation of the (b) surface–ion distance (K, Cl and I) at the most favorable conformation and (c) energy. Label code: Co (blue), O (red), C (black), H (white), K (purple), Cl (green), I (pale orange).

layer. In contrast, for KI, there is a large preference (ΔG = −1.0 eV) for the conformation that accumulates positive charge on the surface. This can be attributed to the largest ionic radius of I^- when compared to Cl^- that makes all electrostatic interactions (and particularly that with the surface) weaker. While the AIMD simulations are carried out without applying an external potential, one can expect that upon externally biasing Co_3O_4 layer with negative voltages, the structure accumulating positive charge on the surface would be favored with respect to that with the two ions close to the surface but without modifying the trends between the two ions. Consequently, simulations shows that KI favors the structure accumulating more positive charge over Co_3O_4 and, in turn, generates a stronger electric field.

In order to further optimize the magneto-ionic response for the KI-containing PC electrolyte, the room temperature
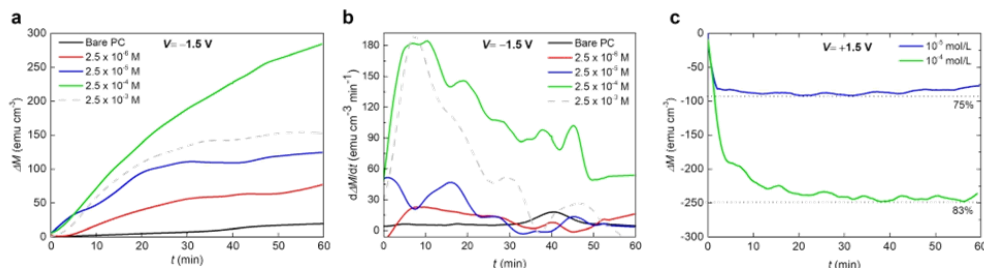
Fig. 3 Impact of KI concentration in PC on Co oxide magneto-ionics. (a) Magnetization (ΔM) as a function of time t for PC with different KI concentrations under electrolyte-gating at −1.5 V, while applying an external in-plane magnetic field of 10 KOe, and (b) the respective magneto-ionic rate, dΔM/dt. (c) Magnetization (ΔM) depletion as a function of time t for the two best performing KI concentrations under an opposite bias (+1.5 V), while applying an external in-plane magnetic field of 10 KOe.

magnetic moment as a function of biasing time were recorded with a 10 kOe field and varying KI concentrations (from 2.5×10^{-6} M to 2.5×10^{-3} M). Upon biasing for 1 hour, the ΔM first increases as the KI concentration increases from 2.5×10^{-6} M to 2.5×10^{-4} M, and then it decreases with further addition of KI. At 2.5×10^{-3} M KI, the oxide film peeled off, possibly because of the strong electrochemical reactions taking place (see the dashed curve in Fig. 3(a)). Indeed, the solution acquired a yellow color, indicating the formation of I_2 gas at the Pt counter electrode, and the subsequent formation of I_3^- according to the reaction:

$$I_{2(g)} + I_{(aq)}^- = I_{(aq)}^{3-} \qquad (1)$$

This further proved the occurrence of electrochemical reactions at the cathode side, *i.e.*, at the cobalt oxide film side. Noteworthily, PC is not susceptible to attack by halogens anodically liberated at a Pt electrode.[16]

Remarkably, after applying −1.5 V for 1 hour, the maximum ΔM for 2.5×10^{-4} M KI electrolyte (≈ 280 emu cm^{-3}) is more than one order of magnitude larger than that for bare PC (≈ 25 emu cm^{-3}). The achieved magneto-ionic rate (*i.e.*, the rate at which the ferromagnetic signal from metallic Co is generated) is drastically enhanced from 5 emu cm^{-3} min^{-1} for bare PC to 184 emu cm^{-3} min^{-1} for PC + 2.5×10^{-4} M KI (see Fig. 3(b)). Moreover, partial recovery under an opposite bias of +1.5 V was observed for the best performing KI concentrations of 2.5×10^{-4} M and 2.5×10^{-5} M (Fig. 3(c)). Room temperature hysteresis loops of the voltage-actuated cobalt oxide films confirm the effect of the KI concentration in PC on the ON–OFF ferromagnetic switching for this system (Fig. 4). This corroborates that magneto-ionic effects have a strong dependence on the KI concentration.

To gain information on the chemical environment of the cobalt oxide film surface, XPS analyses were carried out before and after ME experiments. The Co 2p core-level XPS spectra of as-prepared sample, and samples treated using bare PC and PC + 2.5×10^{-4} M KI are shown in Fig. 5. For the as-prepared sample (see Fig. 5(a)), the two major peaks at 780.1 eV and 795.9 eV match Co 2p$_{3/2}$ and Co 2p$_{1/2}$ binding energies,

respectively, of CoO and/or Co$_3$O$_4$ phases.[12,28,29] The satellite structure at higher binding energies can be ascribed to the shake-up process of the Co^{2+} species in the high-spin state. Aside from these four peaks, Fig. 5(b) clearly shows two shoulders (indicated by the downward arrows) on the lower binding energy side of the major peaks for bare PC-treated sample. The best fitting of the spectrum results in two additional XPS peaks located at 778.3 eV and 793.3 eV, which are the characteristic binding energies of Co 2p$_{3/2}$ and Co 2p$_{1/2}$, respectively, for metallic Co.[2] This unambiguously confirms the reduction of cobalt oxides into Co upon voltage negative actuation in bare PC electrolyte. Interestingly, the relative intensities of these additional peaks and, importantly, at the expense of the oxide Co 2p peaks, become dominant in the case of the film electrolyte-gated in PC + 2.5×10^{-4} M KI. This indicates the formation of significant amounts of metallic Co and, accordingly, higher ΔM as seen in ME experiments. Moreover, it is instructive to point out that there are no observable traces of iodine in the survey spectrum on PC + 2.5×10^{-4} M KI-treated sample (not shown), ruling out the possibility of formation of magnetic iodine-containing compounds. Overall, the formation of metallic Co upon voltage application can be written as:

$$CoO \rightarrow Co + V_{\ddot{O}} \qquad (2)$$

$$Co_3O_4 \rightarrow 3Co + 4V_{\ddot{O}} \qquad (3)$$

where $V_{\ddot{O}}$ stands for O^{2-} vacancy. Note that, while voltage-driven O^{2-} ion motion is likely to be the main origin for the observed magneto-ionic effects, a redox reaction between I$^-$ (a strong reducing agent) and Co^{3+} (with oxidative character) could also partially occur at the surface of the Co oxide films upon voltage actuation.

To further examine the reversibility of the magneto-ionic effects of the cobalt oxide film in the PC + 2.5×10^{-4} M KI electrolyte, voltage pulses of −1.35 V and +1.35 V (of 10 min each) were alternated, and clear changes are observed in ΔM running in parallel to voltage actuation (Fig. 6). Note that up to 5 magneto-ionic cycles could be obtained with these applied voltage pulses.
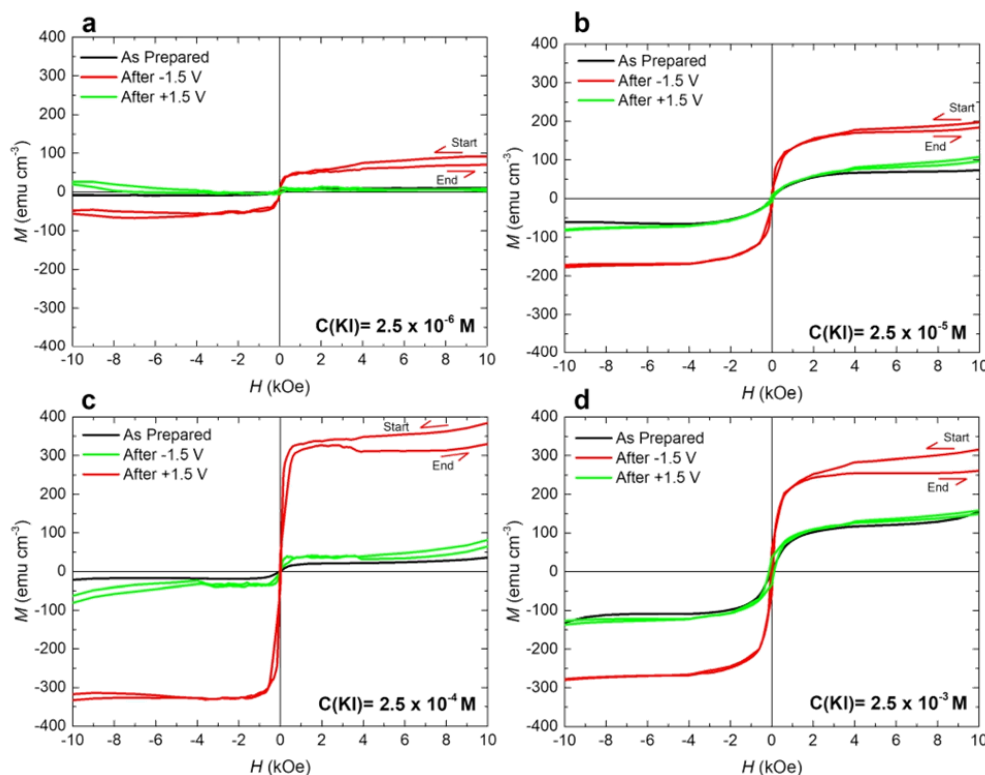
Fig. 4 Magnetization (*M*) *vs.* applied magnetic field (*H*) loops of the investigated cobalt oxide films actuated using different concentrations of KI dissolved in PC. Panels a–d show hysteresis loops corresponding to as-grown states (in black), after applying $\Delta V = -1.5$ V for 1 h (in red) and after subsequently applying +1.5 V (in green). All loops were acquired using a vibrating sample magnetometer with magnetic field applied in-plane. Note that the red and green loops were recorded at 0 V just after switching off the negative or positive voltage, respectively. The red loops are open at the high magnetic field region (at positive saturation) because the system exhibits a slight recovery (slight decrease of M with time) once electrolyte gating is stopped.

Conclusions

Here we have shown that magneto-ionic motion in 15 nm-thick Co oxide films can be dramatically enhanced by proper electrolyte engineering. Faster magneto-ionic rates and larger generation of magnetization are achieved upon the addition of inorganic salts (KI, KCl, and $Ca_2(BF_4)_2$) to PC. In this way, the ionic strength of the medium is increased, thereby causing a higher electric field strength at the Co oxide/electrolyte interface upon biasing. As a result, oxygen motion within the material is favored, thereby enabling the rapid and more extensive formation of metallic cobalt. In particular, potassium iodide at a concentration of 2.5×10^{-4} M brings about a 35-fold increase of magneto-ionic rate and one order of magnitude larger variation in magnetization than for bare PC under -1.5 V biasing for 1 h. AIMD simulations suggest that a more effective EDL would build up for KI compared to KCl. More importantly, the onset potential at which significant changes in the magnetic properties are observed is dramatically decreased when salts are added to PC. Changes are partially reversible under the application of voltage of opposite polarity for 1 hour, and cyclability was observed under voltage pulses of 10 min.

Experimental

Sample preparation

15 nm-thick cobalt oxide films were grown by reactive sputtering at room temperature on B-doped [100]-oriented Si wafers (0.75 mm thick), previously sputtered with an adhesion/seed layer of 20 nm Ti/60 nm Cu. The depositions were performed with an AJA International, Inc. Magnetron Sputtering System ATC Orion with a base pressure of 5×10^{-8} Torr. Argon was used as carrier gas for the Co precursor and O_2 plasma as oxygen source. The target to substrate distance was around 10 cm and the sputtering rate about 23 nm min^{-1}. Co oxide was
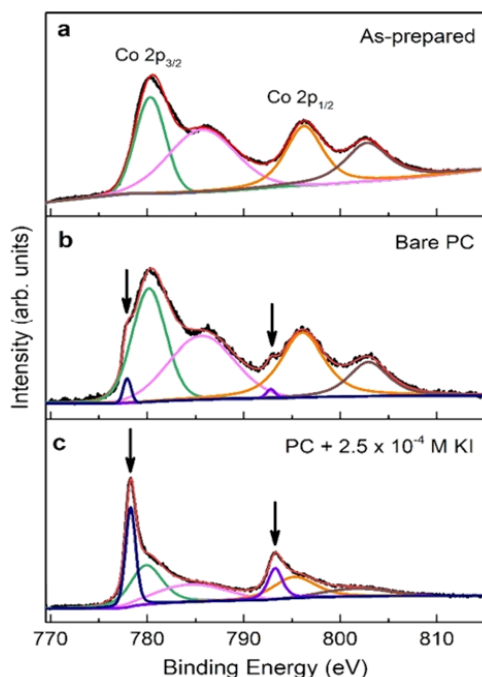
Fig. 5 X-ray photoelectron spectra of Co $2p_{1/2}$ and Co $2p_{3/2}$ for (a) as-prepared, (b) treated in bare PC and (c) PC + 2.5 × 10^{-4} M KI samples. The downward arrows point to the Co $2p_{3/2}$ and Co $2p_{1/2}$ peaks of metallic Co (in blue and purple in (b) and (c)). Additionally, green and orange correspond to Co^{2+}, and pink and brown to Co^{3+}. Solid black lines are experimental data, whereas solid red lines refer to fitting spectra.

Fig. 6 Magneto-ionic cyclability of the 15 nm-thick cobalt oxide film in PC with 2.5 × 10^{-4} M KI under −1.35 V/+1.35 V voltage pulses of 10 min duration each, assessed from in-plane magnetic measurements while applying a magnetic field of 10 kOe.

Compositional measurements

X-ray photoelectron spectroscopy (XPS). XPS analysis were carried out on both the as-prepared sample and the samples subject to magnetoelectric actuation in PC and 2.5 × 10^{-4} M KI-containing PC. A PHI 5500 Multitechnique System spectrometer from Physical Electronics was used, which was equipped with a monochromatic Al K_{α} X-ray source (1486.6 eV) at a power of 350 W. The survey and Co 2p core-level XPS spectra were taken both before and after sputtering the surface with Ar ions for 1 min. All XPS spectra were corrected using the C 1s line at 284.6 eV. Background subtraction and peak fitting were performed with XPSPEAK41 software.

Inductively coupled plasma mass spectrometry (ICP-MS)

The concentration of the salts dissolved in PC were determined by ICP-MS. Specifically, the K^+ concentration (for KI and KCl dissolved in PC) and Ca^{2+} concentration (for $Ca_2(BF_4)_2$ dissolved in PC) were determined on an Agilent (7900 model) spectrophotometer. Before analysis, the aliquots were diluted in HNO_3 1% (v/v).

Magnetoelectric characterization

Magnetic measurements were carried out in-plane at room temperature in a vibrating sample magnetometer from Micro Sense (LOT-Quantum Design) under electrolyte gating using an external power supply (Agilent B2902A). Voltages were applied between the Cu seed-layer beneath the Co oxide film, which acted as a working electrode. and a platinum wire which served as a counter electrode (Fig. 1(a)). An additional platinum wire was introduced into the cell to act as a pseudo-reference electrode. The generated magnetization (M) was studied for Na-treated PC to which different salts (KI, KCl, $Ca_2(BF_4)_2$ had been added.

grown in a 9% O_2/91% Ar (% given from flow rates of the different gases) atmosphere under a total pressure of 3 × 10^{-3} Torr. Prior to that, the adhesive (Ti) and seed (Cu) layers were also grown using the same experimental setup but in an inert Ar atmosphere, and then partially masked to use the remaining uncoated surface for electrical connection in subsequent magnetoelectric experiments.

Electrolyte preparation

The electrolyte solutions were prepared from propylene carbonate (from Sigma-Aldrich). PC was initially treated with metallic Na to remove traces of water, leading Na^+ and OH^- ions behind. Later, varying amounts of KI, KCl and $Ca(BF_4)_2$ were added in excess to the PC-based solution taking into account the solubility limits of these salts in PC at room temperature (s(KI) = 0.221 ± 0.020 mol kg^{-1},[23] s(KCl) = (3.67 ± 0.40) × 10^{-4} mol kg^{-1} [23] and way larger for $Ca(BF_4)_2$ (ca. 0.1 M)).[17] The corresponding supernatants were analyzed by ICP and further diluted with PC-based solution to the final concentrations considered in this study.
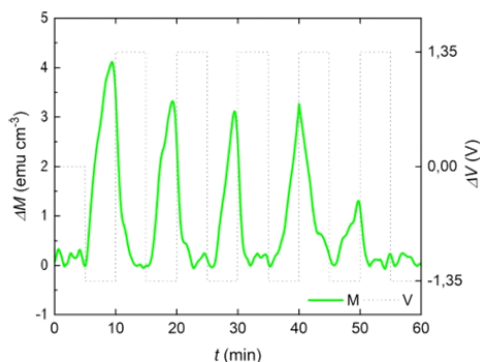
Computational details

The *ab initio* molecular dynamics (AIMD) were performed at 0 V potential using the PBE density functional level of theory[30] with the Hubbard-like term (U), as defined by Dudarev *et al.*[31] The U_{eff} value was fixed to 3.0 eV based on test calculations reported in Table S1 (ESI†). Moreover, the empirical D3 correction[32] was also included to account for dispersion forces. The ionic cores were described with the PAW pseudopotentials and the valence electrons were represented with a plane-wave basis set with an energy cutoff of 500 eV. The first Brillouin zone was sampled with a (2,2,1) Monkhorst–Pack K-point mesh. The simulations were carried out within the *NVT* ensemble (T = 300 K), using the Nosé–Hoover thermostat.[33,34] The time step was set to 1fs, and the simulations were allowed to evolve until 10 ps were achieved. All calculations were performed with the spin polarized formalism as implemented in VASP 5.4 package.[35,36]

The Co_3O_4-propylene interface was represented with a 4-layers thick slab model of the (110) facet where 13 propylene carbonate molecules were added in the vacuum space between images to reproduce the solvent density at room temperature (r = 1.2 g cm^{-3}). Furthermore, a KX (X = Cl or I) unit was included to represent the dissolved salt. Two initial starting configurations were considered for each salt (Fig. S2, ESI†): (a) the two ions are initially located on the surface, directly interacting with Co_3O_4, and (b) the ions are solvated by propylene carbonate molecules and thus located at about 6 Å from the surface. Further details can be found in the supporting information.

Author contributions

E. P., J. S. and E. M. had the original idea and led the investigation. S. M., E. P. and J. S. designed the experiments. S. M. and Z. M. synthesized the cobalt oxide layers. S. M. and Z. M. carried out the magnetoelectric measurements and S. M., E. P., J. S. and E. M. analyzed the data. X. S.-M., M. S. and L. R.-S. carried out the AIMD simulations. Z. M performed and analyzed the XPS measurements. All authors discussed the results and commented on the article. The article was written by S. M., E. P., J. S and E. M.

Conflicts of interest

There are no conflicts to declare.

Acknowledgements

References

1 Y. Shiota, T. Nozaki, F. Bonell, S. Murakami, T. Shinjo and Y. Suzuki, *Nat. Mater.*, 2012, **11**, 39–43.

2 C. Song, B. Cui, F. Li, X. Zhou and F. Pan, *Prog. Mater. Sci.*, 2017, **87**, 33–82.

3 C. Leighton, *Nat. Mater.*, 2019, **18**, 13–18.

4 J. De Rojas, J. Salguero, A. Quintana, A. Lopeandia, M. O. Liedke, M. Butterling, A. G. Attallah, E. Hirschman, A. Wagner, L. Abad, J. L. Costa-Krämer, J. Sort and E. Menéndez, *Phys. Rev. Appl.*, 2021, **16**, 034042.

5 G. Wang, L. Zhang and J. Zhang, *Chem. Soc. Rev.*, 2012, **41**, 797–828.

6 P. Sharma and T. S. Bhatti, *Energy Convers. Manage.*, 2010, **51**, 2901–2912.

7 C. Navarro-Senent, A. Quintana, E. Menéndez, E. Pellicer and J. Sort, *APL Mater.*, 2019, 7, 030701.

8 M. Nichterwitz, S. Honnali, M. Kutuzau, S. Guo, J. Zehner, K. Nielsch and K. Leistner, *APL Mater.*, 2021, **9**, 030903.

9 G. Feng, J. Huang, B. G. Sumpter, V. Meunier and R. Qiao, *Phys. Chem. Chem. Phys.*, 2010, **12**, 5468–5479.

10 A. Quintana, E. Menéndez, M. O. Liedke, M. Butterling, A. Wagner, V. Sireus, P. Torruella, S. Estradé, F. Peiró, J. Dendooven, C. Detavernier, P. D. Murray, D. A. Gilbert, K. Liu, E. Pellicer, J. Nogues and J. Sort, *ACS Nano*, 2018, **12**, 10291–10300.

11 J. de Rojas, A. Quintana, A. Lopeandía, J. Salguero, J. L. Costa-Krämer, L. Abad, M. O. Liedke, M. Butterling, A. Wagner, L. Henderick, J. Dendooven, C. Detavernier, J. Sort and E. Menéndez, *Adv. Funct. Mater.*, 2020, **30**, 2003704.

12 S. Martins, J. de Rojas, Z. Tan, M. Cialone, A. F. Lopeandía, J. Herrero-Martín, J. Costa-Kramer, E. Menéndez and J. Sort, *Nanoscale*, 2022, **14**, 842–852.

13 J. de Rojas, A. Quintana, A. Lopeandía, J. Salguero, B. Muñiz, F. Ibrahim, M. Chshiev, A. Nicolenco, M. O. Liedke, M. Butterling, A. Wagner, V. Sireus, L. Abad, C. J. Jensen, K. Liu, J. Nogués, J. L. Costa-Krämer, E. Menéndez and J. Sort, *Nat. Commun.*, 2020, **11**, 5871.

14 J. De Rojas, J. Salguero, F. Ibrahim, M. Chshiev, A. Quintana, A. Lopeandia, M. O. Liedke, M. Butterling, E. Hirschmann, A. Wagner, L. Abad, J. L. Costa-Krämer, E. Menéndez and J. Sort, *ACS Appl. Mater. Interfaces*, 2021, **13**, 30826–30834.

15 A. González, E. Goikolea, J. A. Barrena and R. Mysyk, *Renewable Sustainable Energy Rev.*, 2016, **58**, 1189–1206.

16 B. Worths, *Int. Union Pure Appl. Chem.*, 1977, **49**, 885–892.

17 J. D. Forero-Saboya, E. Marchante, R. B. Araujo, D. Monti, P. Johansson and A. Ponrouch, *J. Phys. Chem. C*, 2019, **123**, 29524–29532.

18 X. Chen, X. Shen, T. Z. Hou, R. Zhang, H. J. Peng and Q. Zhang, *Chem*, 2020, **6**, 2242–2256.

19 L. Zhang and Y. Chen, *Energy Mater.*, 2021, 1–9.

20 J. Zheng, J. A. Lochala, A. Kwok and Z. D. Deng, *Adv. Sci. News*, 2017, 1700032.

21 A. Molinari, H. Hahn and R. Kruk, *Adv. Mater.*, 2019, **31**, 1806662.

22 K. Leistner, *Curr. Opin. Electrochem.*, 2020, **25**, 100636.

23 N. Peruzzi, P. Lo Nostro, B. W. Ninham and P. Baglioni, *J. Solution Chem.*, 2015, **44**, 1224–1239.

24 A. M. Melemed, A. Khurram and B. M. Gallant, *Batteries Supercaps*, 2020, **3**, 570–580.

25 L. Cao, O. Petracic, X.-K. Wei, H. Zhang, T. Duchoň, F. Gunkel, A. Koutsioubas, K. Zhernenkov, K. Z. Rushchanskii, H. Hartmann, M. Wilhelm, Z. Li, Y. Xie, S. He, M. L. Weber, K. Veltruská, A. Stellhorn, J. Mayer, S. Zhou and T. Brückell, *Small*, 2021, 2104356.

26 Q. Wang, Y. Gu, S. Yin, Y. Sun, W. Liu, Z. Zhang, F. Pan and C. Song, *Nanoscale*, 2021, **13**, 18256–18266.

27 Q. Wang, Y. Gu, W. Zhu, L. Han, F. Pan and C. Song, *Adv. Funct. Mater.*, 2021, **31**, 2106765.

28 H. Xiong, Y. Zhang, K. Liew and J. Li, *J. Mol. Catal. A: Chem.*, 2005, **231**, 145–151.

29 C. D. Wanger, W. M. Riggs, L. E. Davis and J. F. G. E. M. Moulder, *Handbook of X-ray Photoelectron Spectroscopy*, Perkin-Elmer, John Wiley & Sons, Ltd, Eden Prairie, 1978.

30 J. P. Perdew, K. Burke and M. Ernzerhof, *Phys. Rev. Lett.*, 1996, **77**, 3865–3868.

31 S. Dudarev and G. Botton, *Phys. Rev. B: Condens. Matter Mater. Phys.*, 1998, **57**, 1505–1509.

32 S. Grimme, J. Antony, S. Ehrlich and H. Krieg, *J. Chem. Phys.*, 2010, **132**, 154104.

33 W. G. Hoover, *Phys. Rev. A: At., Mol., Opt. Phys.*, 1985, **31**, 1695–1697.

34 S. Nosé, *J. Chem. Phys.*, 1984, **81**, 511–519.

35 G. Kresse and J. Hafner, *Phys. Rev. B: Condens. Matter Mater. Phys.*, 1993, **47**, 558–561.

36 G. Kresse and J. Furthmüller, *Phys. Rev. B: Condens. Matter Mater. Phys.*, 1996, **54**, 11169–11186.

Enhancing magneto-ionic effects in cobalt oxide films by electrolyte engineering

Sofia Martins,*[a] Zheng Ma,[a] Xavier Solans-Monfort,[b] Mariona Sodupe,[b] Luis Rodriguez-Santiago,[b] Enric Menéndez,[a] Eva Pellicer, *[a] and Jordi Sort [a,c]

[a]Departament de Física, Universitat Autònoma de Barcelona, E-08193 Cerdanyola del Vallès, Spain.

[b]Departament de Química, Universitat Autònoma de Barcelona, E-08193 Cerdanyola del Vallès, Spain

[c]Institució Catalana de Recerca i Estudis Avançats (ICREA), Pg. Lluís Companys 23, E-08010 Barcelona, Spain

Further computational details.

Determination of the Hubbard U_{eff} term

The U_{eff} term of the Hubbard correction was determined by analyzing how this correction to DFT influences the material cell parameters as well as it localizes the unpaired electrons on the Co^{2+} cations. Results reported in Table S1 show that absence of Hubbard correction or low U_{eff} values leads to cell parameters that are closer to the X-ray determined ones. However, in these cases the spin density of Co^{2+} is partially delocalized. Increasing the U_{eff} term localizes the electron density on Co^{2+} but the optimized cell parameters become larger. An U_{eff} value of 3.0 eV appears to be a good compromise between spin density localization and cell parameters reproducibility and thus, it has been applied to all AIMD simulations. Remarkably, U_{eff} = 3.0 eV lies in between those suggested for Co_3O_4 in previous contributions.[4–6]

Table S1. Cell parameters and magnetization on the Co^{2+} tetrahedric sites as function of the applied Hubbard correction. Experimental values are added for comparison.

Method (U_{eff} in eV)	a (Å)	μ (e⁻)
PBE-D3	8.06	2.24
PBE-D3-U (U = 2.0)	8.09	2.52
PBE-D3-U (U = 2.5)	8.09	2.57
PBE-D3-U (U = 3.0)	8.10	2.61
PBE-D3-U (U = 3.5)	8.10	2.64
PBE-D3-U (U = 4.0)	8.11	2.67
Exp.	8.08	3.00

SUPPORTING INFORMATION

Model construction

The Co_3O_4-propylene interface model was constructed through three successive steps. First of all, a slab model of Co_3O_4 was developed. The Co_3O_4 surface used is a (1x1) stoichiometric crystalline slab of the (110) facet. We chose the (110) facet as it has been shown to be the predominant surface in Co_3O_4 nanorods[11] and thus, it can be used as a representative example in the present simulations. The top outermost layer contains O^{2-} anions and Co^{3+} cations and, similarly to other Co_3O_4 slab models reported in the literature, the thickness of the model is around 10 Å and it implies 4 material layers.[6] In a second step, 13 propylene carbonate molecules were added in the vacuum box between images. This leads to a solution with a solvent density of around 1.2 g cm^{-3}, which is in agreement with the propylene carbonate density at room temperature. The initial conformation of the propylene carbonate solvent molecules was obtained with the Packmol software,[12] which creates initial configurations for MD simulations. Finally, a KX (X = Cl or I) unit was added to the model to account for the effect of the dissolved salt. The addition of one KX unit leads to solute concentrations of about 0.9 M. This value is higher than the concentration in experiments, but more dilute models are not feasible due to the required computational resources. Indeed, the final model already contains 283 atoms.
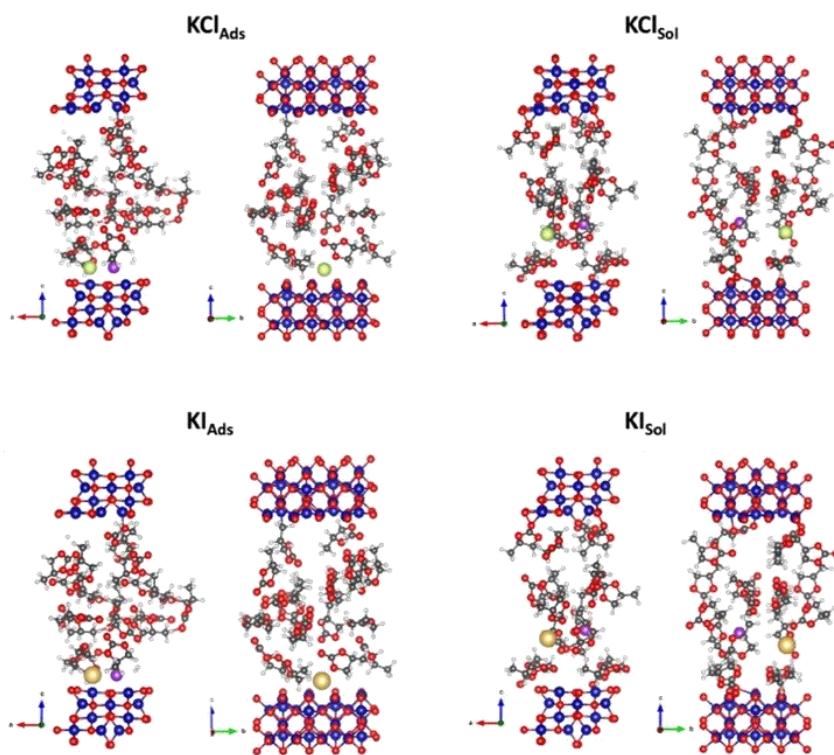
Fig. S1 Initial structures (two views) of the four AIMD simulations carried on. Label code: Co (blue), O (red), C (black), H (white), K (purple), Cl (green), I (pale orange).

Fig. S2 Variation of the K⋯surface distance along the four AIMD simulations performed.
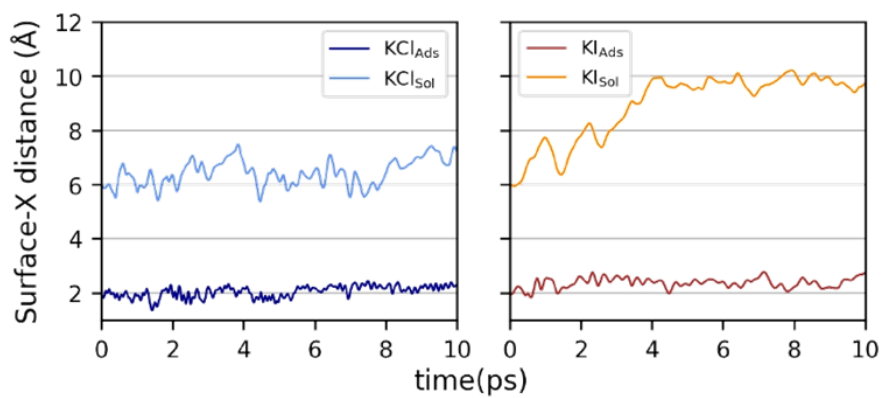
Fig. S3. Variation of the anion⋯surface distance along the four AIMD simulations performed.
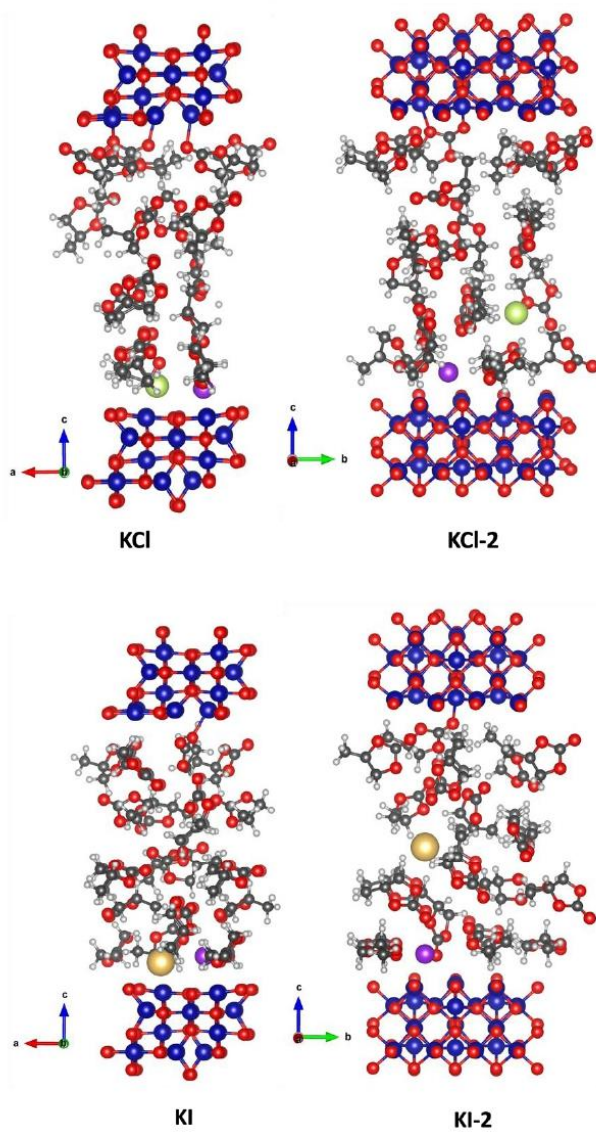
Fig. S4 Representative snapshots the four AIMD simulations. Label code: Co (blue), O (red), C (black), H (white), K (purple), Cl (green), I (pale orange).
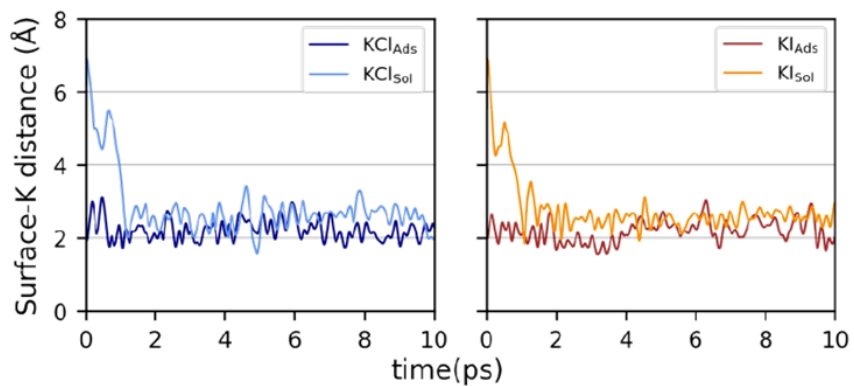
SUPPORTING INFORMATION

References

(1)   J. P. Perdew, K. Burke, M. Ernzerhof, *Phys. Rev. Lett.* 1996, **77**, 3865–3868.

(2)   S. Dudarev and G. Botton, Phys. Rev. B - Condens. Matter Mater. Phys., 1998, **57**, 1505–1509.

(3)   S. Grimme, J. Antony, S. Ehrlich, H. Krieg, *J. Chem. Phys.* 2010, **132**, 154104.

(4)   J. Chen, X. Wu, A. Selloni, *Phys. Rev. B* 2011, **83**, 245204.

(5)   D. Jiang, S. Dai, *Phys. Chem. Chem. Phys.* 2011, **13**, 978–984.

(6)   W. Hu, J. Lan, Y. Guo, X.-M. Cao, P. Hu, *ACS Catal.* 2016, **6**, 5508–5519.

(7)   W. G. Hoover, *Phys. Rev. A* 1985, **31**, 1695–1697.

(8)   S. A . Nosé, *J. Chem. Phys.* 1984, **81**, 511–519.

(9)   G. Kresse, J. Hafner, *Phys. Rev. B* 1993, **47**, 558–561.

(10)   G. Kresse, J. Furthmüller, *Phys. Rev. B* 1996, **54**, 11169–11186.

(11)   X. Xie, Y. Li, Z.-Q. Liu,; M. Haruta, W. Shen, *Nature* 2009, **458**, 746–749.

(12)   L. Martínez, R. Andrade, E. G. Birgin, J. M. Martínez, *J. Comput. Chem.* 2009, **30**, 2157–2164.

3.3. Controlling magneto-ionics by defect engineering through light ion implantation

For consistency with the previous Results section, this chapter is structured as a research article

Abstract

Magneto-ionics relies on the voltage-driven transport of ions to modify magnetic properties. As a diffusion-controlled mechanism, defects play a central role in determining ion motion and, hence, magneto-ionic response. Here we exploit the potential of ion implantation to engineer depth-resolved defect density and type with the aim to control the magneto-ionic behavior of Co_3O_4 thin films. We demonstrate that, by the interplay between the highly nanostructured nature of the magneto-ionic target (*i.e.*, 50 nm thick Co_3O_4 film) and a single implantation process of light ions (He^+) at 5 keV, the magneto-ionic response, in terms of rate and amount of generated magnetization, of the Co_3O_4 film at short-, mid-, and long-term voltage actuation can be controlled by varying the generated collisional damage through ion fluence. This proof-of-principle paves the way to further exploit ion implantation in relation to ion nature, energy, fluence, target temperature and multiple implantations for magneto-ionics.

The increasingly growing demands on data processing and storage, driven by Big Data, are pushing information technology to its performance limits; particularly, from an energy-efficiency viewpoint, which is becoming a major bottle-neck in current computing[1]. Although artificial intelligence is showing successful to tackle Big Data requests, this is mainly achieved by software means, thus at a cost of a large energy consumption. Artificial intelligence is at a turning point and requires low-power technologies to build new computing hardware[2,3]. Voltage control of magnetism (VCM) holds the potential to revolutionize computing from an energy-efficiency standpoint since it allows modifying magnetic properties by electric fields instead of electric currents, decreasing Joule heating effect and, ultimately, resulting in a reduced power consumption[1,4–8]. Among VCM mechanisms[1,4–6], electric-field-induced ion motion to modulate magnetism of a target material (magneto-ionics) stands out since it allows for a voltage-driven modulation of magnetic properties to an extent never reached by any other VCM means[7,8]. Even though mobile ion species of different nature, such as H^{+}[9–12], Li^{+}[13–15], N^{3-} [16–20], O^{2-} [21–26] or F^{-}[27], dissimilar magneto-ionic targets and layered architectures (*e.g.*, the use of adjacent reservoirs to source ions to the target or targets in which the mobile ion is already present in it), and distinct approaches are used to apply electric field (*e.g.*, by solid-state electrolytes[9,22,23] or the formation of an electric double layer through liquid electrolytes[16–20,24–26]), magneto-ionics in the end relies on ion transport[7,8,16,21].

Structural defects may have a strong influence on ion diffusion in solids, generally enhancing ionic motion[8,16,24,28–31]. In fact, not only defect type and density play a role in ion migration but also depth distribution[31]. Thus, magneto-ionic systems could largely benefit from a controlled defect type, density, and distribution along depth. Even though defect manipulation remains challenging, ion implantation at energies below 100 keV turns out to be particularly suitable to modify materials in the sub-100 nm depth range from structural and compositional viewpoints[32]. Ion implantation has already been used to modify magnetic properties[33], such as magnetic anisotropy[34], saturation magnetization by order-disorder transitions[35] or phase transformations[36], ferromagnetic/antiferromagnetic coupling[37], synthesis of composite multiferroics[38] or, more recently, the formation and control of skyrmions[38] and magneto-ionics[39]. However, its potential to engineer defects in terms of size, density, and distribution (*i.e.*, with depth resolution) aimed at enhancing ion motion and generated magnetization in magneto-ionics has been largely overlooked.

Here we show that, by the interplay between the preexisting microstructure of the magneto-ionic target (*i.e.*, 50 nm thick Co_3O_4 film) and a single implantation process of light ions (He^+) at 5 keV, the magneto-ionic response, in terms of rate and amount of generated magnetization, of the Co_3O_4 film at short-, mid-, and long-term voltage actuation can be controlled by varying the generated collisional damage through ion fluence.

Results & Discussion

Growth of the magneto-ionic targets (Co₃O₄ films) by reactive sputtering. 50 nm thick Co_3O_4 films were grown atop [100]-oriented Si substrates, previously coated with 20 nm of Ti and 60 nm of Cu, by reactive sputtering (see Methods for further details). Depositions were carried out while partly masking the Cu/Ti buffer layers to serve afterwards as working electrode for the magnetoelectric characterization. As seen in Fig. 1a, the Co_3O_4 film is highly nanostructured with rather elongated grains along the perpendicular direction to the film plane. This columnar-shaped growth has already been evidenced in thicker Co_3O_4 films grown by atomic layer deposition[24], which is a much slower deposition technique compared to reactive sputtering, thus suggesting the tendency of Co_3O_4 to grow in such form. Fig. 1b is a high-resolution transmission electron microscopy (TEM) image of the bottom region of the cross section of the Co_3O_4 layer, which includes the fast Fourier transform (FFT) of the region marked with an orange square. Spots labelled as "1" and "2" are consistent with (311) Co_3O_4 (PDF® 00-009-0418) and (111) CoO (PDF® 00-001-1227) interplanar distances (0.244 and 0.245 nm, respectively), whereas spots "3" and "4" are unambiguously ascribed to (111) Co_3O_4 (PDF® 00-009-0418) and (200) CoO (PDF® 00-001-1227) interplanar distances (0.467 and 0.212 nm, respectively). This indicates that the as-grown films consist of a mixture of Co_3O_4 and CoO phases in agreement with previously reported results. This is linked to the role of the Cu

buffer layer which also might suffer from oxidation while depositing (as evidenced by the brightness of the Co_3O_4-Cu interface in Fig. 1a), yielding effectively a decreased oxygen partial pressure, which promotes the growth of CoO over Co_3O_4 in the first nm. With thickness, this effect weakens and Co_3O_4 grows then preferentially[26]. For simplicity, the films are denoted as Co_3O_4 along the text.
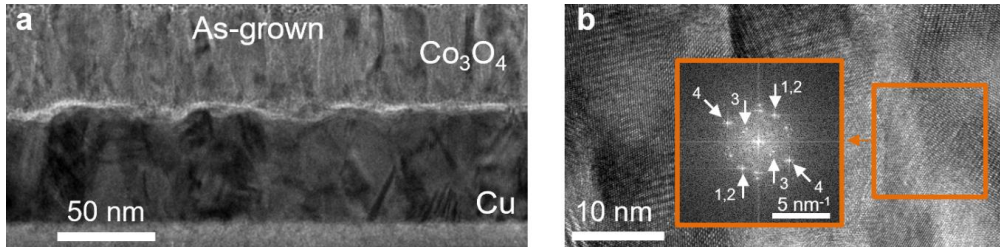
Fig. 1 Structural characterization of the Co_3O_4 films by transmission electron microscopy (TEM). a TEM image of the cross-section of an as-grown Co_3O_4 film. **b** High-resolution TEM image of a bottom region of the cross section of the Co_3O_4 layer imaged in a, which includes the fast Fourier transform of the region marked with an orange square. "1" and "2" spots are consistent with (311) Co_3O_4 (PDF® 00-009-0418) and (111) CoO (PDF® 00-001-1227) interplanar distances (0,244 and 0,245 nm, respectively), while spots "3" and "4" are unambiguously ascribed to (111) Co_3O_4 (PDF® 00-009-0418) and (200) CoO (PDF® 00-001-1227) interplanar distances (0,467 and 0.212 nm, respectively).

Defect characterization at atomic level by means of variable energy positron annihilation lifetime spectroscopy (VEPALS)[41–45] reveals that roughly two "sublayers" with different defect size and density can be distinguished across the as-grown Co_3O_4 films. PALS provides the positron lifetime τ, which is a measure of defect size and, thus, of defect type, as a function of the depth of the investigated material. Three representative size ranges, known as lifetime components τ_i (where i = 1, 2 or 3), can be characterized. The shortest lifetime component τ_1

represents vacancy clusters, the intermediate lifetime component τ_2 accounts for larger vacancy clusters linked to grain boundaries or small pores in case of the largest values, and the longest lifetime component τ_3 is attributed to even larger pores or voids. Each component has a corresponding relative intensity (I_i) which to some extent reflects the concentration of each defect type[41–45]. Fig. 2 shows the depth-dependence of τ_1 and τ_2 and the corresponding relative intensities, I_1 and I_2, respectively. Note that, at each depth, the sum of I_1 and I_2 is very close to 100 %, indicating that τ_3 is virtually negligible, in agreement with the absence of voids in the TEM characterization of the cross-section of the as-grown Co_3O_4 film (Fig. 1). Positron lifetimes might be overestimated along the top part of the Co_3O_4 film due to influence of roughness and surface broken symmetry, becoming negligible at depths above 20 nm (> 2 keV in terms of positron implantation energy, E_P); see Methods for further details[46]. At depths above 20 nm (> 2 keV), positron lifetimes can be considered as fully representative of the Co_3O_4 film and, with depth, τ_1, τ_2 and I_1 decrease, while I_2 increases (all in a monotonic way). However, all suffer from a more pronounced change between 2,6 and 2,8 keV (which represent depths of around 28 and 31 nm, respectively). This could be linked to an interface region amongst two "sublayers" with different defect size and density. Considering the defect size and density at 2,2 keV (21 nm) and 3,2 keV (39 nm) as representative values for the top and bottom "sublayers", respectively, the top region shows τ_1, τ_2, I_1 and I_2 values of 0.2829 ns, 0.4211 ns, 65.7

% and 34.1 %, respectively, whereas the bottom counterpart exhibits τ_1, τ_2, I_1 and I_2 values of 0,2355 ns, 0,3848 ns, 46,5 % and 53,3 %, respectively. Fig. S1 shows the *ab initio* calculations of the positron lifetime in Co_3O_4 as a function of vacancy cluster size[47–49], indicating that mixed vacancy cluster sizes of 10 and 4 vacancies are consistent with the τ_1 values of the top and bottom "sublayers", respectively. This agrees with the highly nanostructured nature of the sputtered Co_3O_4 film. Moreover, the existence of these two regions might be somewhat related to the mixture of Co oxides at the initial stages of the film growth. Remarkably, τ_2 values are not so much larger than τ_1 ones, suggesting that both components might represent the same defect type, *i.e.*, mixed vacancy clusters which could be linked to grain boundaries with different size. This in agreement with the TEM characterization where grain boundaries are clearly observed (Fig. 1).
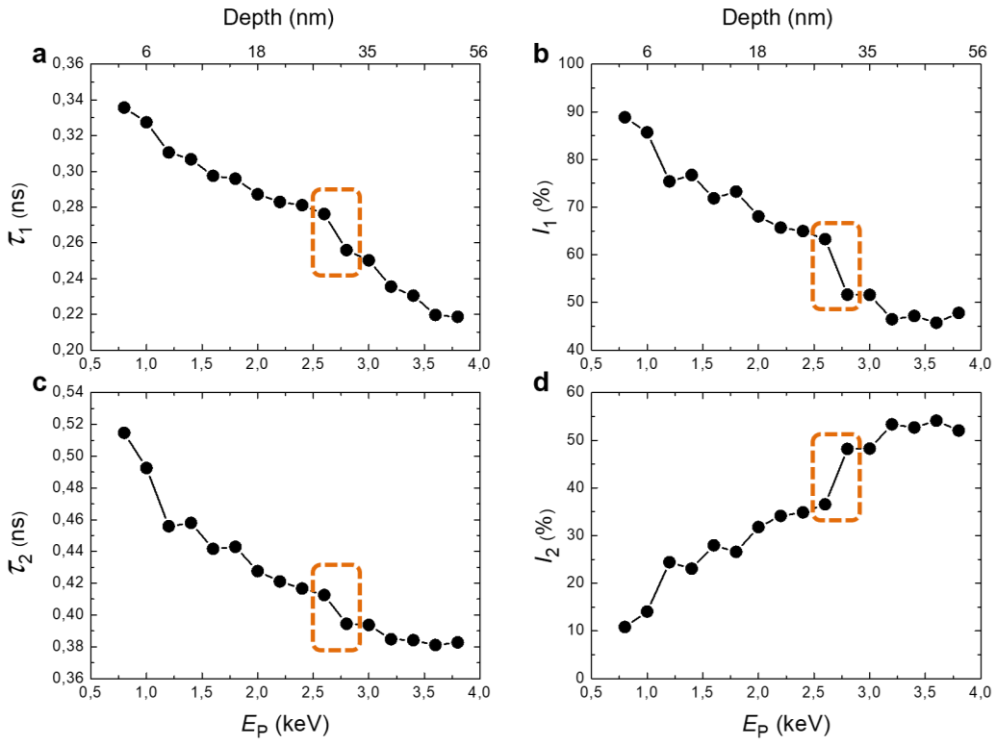
Fig. 2 Depth-resolved defect characterization of the as-grown Co₃O₄ films by variable energy positron annihilation lifetime spectroscopy (VEPALS). a and **b** are the positron lifetime component 1 (τ_1) and the corresponding relative intensity (I_1), respectively, as a function of depth, which can be also given in positron implantation energy (E_P). See Methods for further details. **c** and **d** are the positron lifetime component 2 (τ_2) and the corresponding relative intensity (I_2), respectively, as a function of depth. The orange dashed rectangles indicate the interface region which separates the two "sublayers" that can be distinguished from a defect standpoint. The lines connecting data points are guides to the eye.

Defect engineering through light ion implantation. Controlling defect type (size), density and distribution is central for ion diffusion. Typically, ion transport becomes enhanced with size and density[28–30]. Defect manipulation with depth-resolution remains challenging. The first attempt to tailor defect structure relies on the growth method. For instance, growing Co₃O₄ by reactive sputtering tends to result in larger

defect sizes than Co_3O_4 grown by techniques which involve slower deposition rates, such as atomic layer deposition[24]. However, further control of the microstructure is strongly required to control ion diffusion. Aimed at further tailoring defect type and density along depth, ion implantation at energies of the order of 1–100 keV turns out to be particularly suitable to modify materials in the sub-100 nm depth range from structural and compositional viewpoints[32]. In a first approximation, the penetration of ions is controlled by their energy, while implantation damage (also known as collisional damage) is determined by the fluence[32]. Typically, in ion implantation processes into crystalline materials, impinging ions collide with lattice atoms, displacing them from their equilibrium lattice sites and, for instance, forming vacancies. With fluence, these vacancies may grow forming vacancy clusters, grain boundaries and, eventually, disordered regions[32]. However, a completely different scenario in terms of collisional damage is opened when the implantation target is highly defective, enabling new mechanisms of ion-solid interactions[50–52]. Even though not so much is known about the interaction of preexisting defects with impinging ions[52], theoretical calculations by molecular dynamics report on the role of implantation fluence in determining the size of preexisting defects[51]. In fact, nanopore size reduction has been reported by 3 keV Ar ion implantation at normal incidence into amorphous-like materials[50]. Recently, it has been shown that, with ion fluence leading to collisional damages up to 0,1 dpa, the density of

small vacancy clusters increases while the size of pores reduces significantly in highly defective Fe films upon 2 MeV Fe ion implantation at normal incidence[52]. Inspired by these results and considering the highly defective nature of the as-grown Co_3O_4 films, 5 keV He ion implantation to a fluence of 10^{15} ion/cm^2 was used to achieve a maximum collisional damage of around 0,1 dpa (Fig. 3). The ion energy of 5 keV was adjusted to have the maximum collisional damage located at the first half of the Co_3O_4 film (specifically, at a depth around 18 nm), avoiding a pronounced atomic intermixing at the Co_3O_4/Cu interface which could be detrimental to the conductivity of the Cu buffer layer and, thus, harmful to its role as bottom electrode. He ion implantation to a fluence of 10^{14} ion/cm^2 was also caried out to achieve degrees of collisional damage much below 0,1 dpa: 10^{-2}. The reason to choose such fluence is also motivated by the dynamic recovery process that the induced collisional damage undergoes when impinging light ions since the induced defects are more prone to diffuse than those created by heavy ions[35]. In other words, the simulated collisional damage might be somewhat underestimated. Light noble He ions were chosen to avoid compositional changes in the Co_3O_4 film and minimize film sputtering. Fig. 3 shows how collisional damage evolves across the Co_3O_4 film for the fluences used. This is calculated from the collisional damage profiles given in number of displacements per impinging ion and crossed distance (Fig. S2) simulated by the TRIM (TRansport of Ions in Matter) program[53]. From these results, which depend on the implantation

target, ion nature and energy, dpa at each depth for the used fluences can be obtained by multiplying fluence and the number of displacements per impinging ion and crossed distance, and then dividing the obtained result by the atomic density of the target material. An unit of 1 dpa means that, on average, every atom in the implanted volume has been displaced once from its equilibrium lattice site.
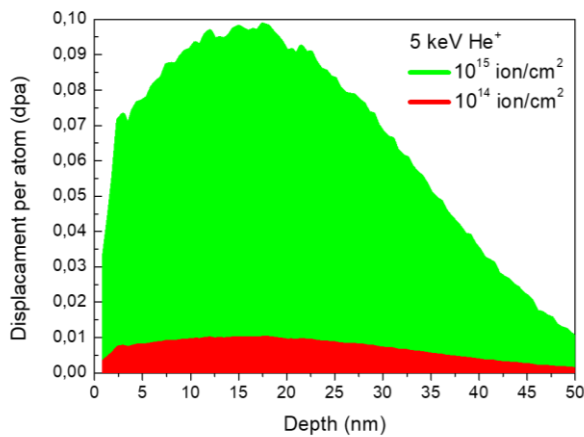
Fig. 3 Depth-resolved collisional damage given as displacement per atom (dpa) caused by 5 keV He ion implantation into Co_3O_4. Depth-resolved collisional damage for the fluences of 10^{14} and 10^{15} ion/cm². These results are obtained from the TRIM simulation presented in Fig. S2[52].

As seen in Fig. 4, 5 keV He ion implantation to a fluence of 10^{15} ion/cm² into 50 nm thick Co_3O_4 layer results in virtually no sputtering of the Co_3O_4 film. Even though no pronounced differences are found at TEM level with the as-grown film (compare Fig. 1 with Fig. 4), boundaries between elongated grains become blurred (*i.e.*, less well-defined) upon implantation to 10^{15} ion/cm², suggesting that they might have thinned down.
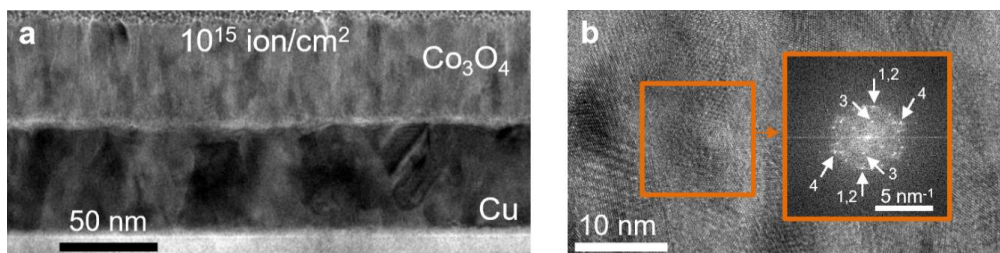
Fig. 4 Structural characterization of a Co₃O₄ film implanted with 5 keV He ions to a fluence of 10¹⁵ ion/cm² by transmission electron microscopy (TEM). **a** TEM image of the cross-section of an as-grown Co_3O_4 film. **b** High-resolution TEM image of a bottom region of the cross section of the implanted Co_3O_4 layer imaged in a, which includes the fast Fourier transform of the region marked with an orange square. "1" and "2" spots are consistent with (311) Co_3O_4 (PDF® 00-009-0418) and (111) CoO (PDF® 00-001-1227) interplanar distances (0.244 and 0.245 nm, respectively), while spots "3" and "4" are unambiguously ascribed to (111) Co_3O_4 (PDF® 00-009-0418) and (200) CoO (PDF® 00-001-1227) interplanar distances (0.467 and 0.212 nm, respectively).

To investigate how the Co_3O_4 microstructure evolves with ion implantation fluence at atomic level, a depth-resolved defect characterization (Fig. 5) was carried out by means of Doppler broadening variable energy positron annihilation spectroscopy (DBVEPAS)[41,42] and VEPALS[41–45]. Fig. 5a shows the evolution of the S parameter with depth, which strongly varies with ion fluence, confirming the role of ion implantation in altering defect size and density. Note that defect size and density cannot be disentangled from S and, thus, compensation effects might occur in systems where defect size varies oppositely to the defect density (*i.e.*, while one increases, the other decreases or *vice versa*). In contrast to DBVEPAS, VEPALS allows determining defect size and to some extent defect density as a function of depth. As seen in Fig. 5b, the depth-resolved evolution of the average lifetime $\tau_{Average}$ follows a well-defined trend with ion fluence.

Remarkably, at a first glance, the average lifetime decreases with fluence regardless depth, indicating that defect size decreases with fluence. After a close look, this trend does not apply to the top 13 nm of Co_3O_4 (1,6 keV) of the film implanted to 10^{14} ion/cm^2 which show a slight increase of the average lifetime. Fig. 5c and 5d show the depth-dependence of the positron lifetime component 1 (τ_1) and the corresponding relative intensity (I_1), respectively, whereas Fig. 5e and 5f exhibit the positron lifetime component 2 (τ_2) and the corresponding relative intensity (I_2), respectively. As seen in Fig. 5c, the depth-resolved evolution of τ_1 of the film implanted to 10^{14} ion/cm^2 overlaps with that one of the as-grown film, indicating that at such fluence mixed vacancy cluster of around 4 vacancies remain unaltered in size. Conversely, upon implanting to 10^{15} ion/cm^2, the size of vacancy clusters decreases. Remarkably, from a depth of around 39 nm (3.2 keV) on, the values of τ_1 overlap for all films, in agreement with the localized implantation damage profile within the top part of the film. Conversely, the relative intensity I_1 follows an opposite behavior: it remains rather unaltered (being τ_1 the dominant defect size since the lower value is above 60 %) with fluence up to depths of around 28 nm (2,6 keV). At further depths, I_1 tends to increase with fluence. With respect to τ_2, the implanted film to 10^{14} ion/cm^2 shows slightly larger values than the as-grown film. Conversely, for the 10^{15}, τ_2 decreases with fluence. As it happens with τ_1, τ_2 values also tend to overlap at a depth of around 39 nm (3.2 keV). As it happens with I_1, I_2 remains rather unchanged with fluence up to

depths of around 28 nm (2,6 keV). At further depths, in contrast to I_1, I_2 tends to decrease with fluence. However, for implanted samples, the density of mixed vacancy clusters with a number of vacancies below 10 is dominant (> 50 %) compared to larger mixed vacancy clusters. This is consistent with narrower columnar grain boundaries upon implantation to 10^{15} ion/cm^2, in agreement with the TEM results which evidence that columnar grain boundaries tend to become less-well defined. Since small mixed vacancy clusters are dominant over large mixed vacancy clusters, a detailed evolution of τ_1 and I_1 with fluence is shown for the two different "sublayers" in Fig. 5g. Here, it can be seen the overall effect of ion implantation, which tends to decrease defect size while keeping the same defect density in the top "sublayer". Conversely, in the bottom "sublayer", the trends become opposite: defect size remains rather unaltered and defect density increases with fluence. Remarkably, given a highly nanostructured film, with a single ion implantation process, depth-resolved defect structure can be largely engineered with a fluence window from 10^{14} ion/cm^2 to 10^{15} ion/cm^2.
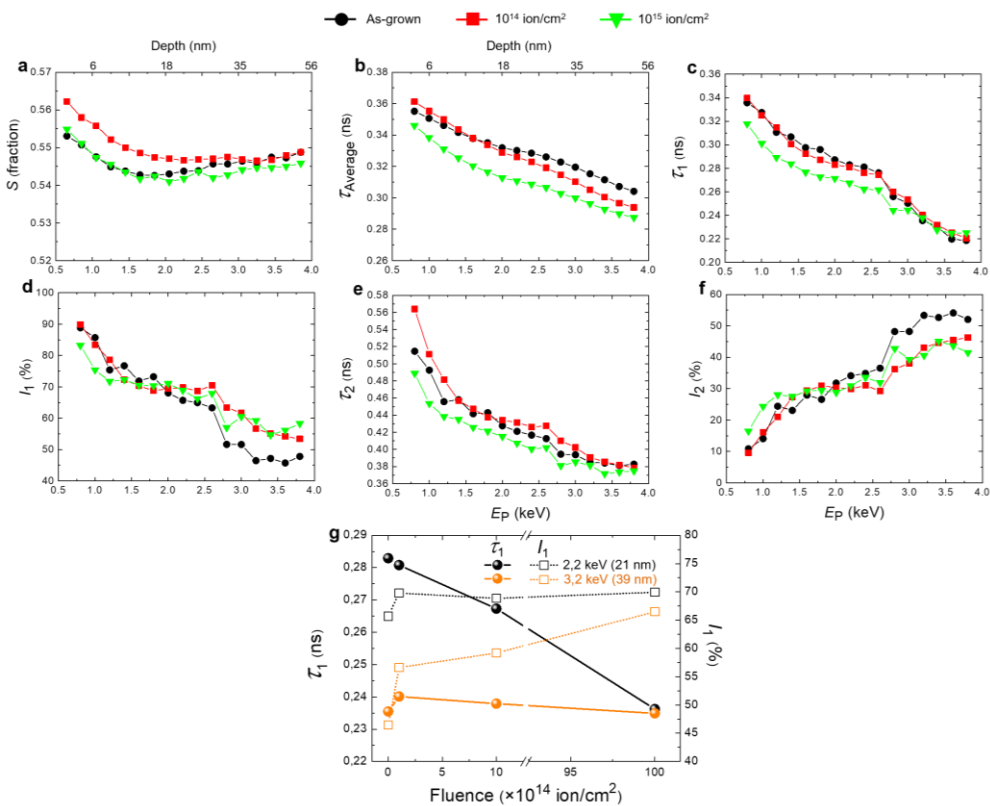
Fig. 5 Depth-resolved defect characterization of as-grown and implanted Co_3O_4 films by Doppler broadening variable energy positron annihilation spectroscopy (DBVEPAS) and variable energy positron annihilation lifetime spectroscopy (VEPALS). a *S* parameter obtained by DBVEPAS characterization as a function of depth which can be also given in positron implantation energy (E_P). See Methods for further details. **b** Average lifetimes obtained by VEPALS as a function of depth. **c** and **d** are the positron lifetime components 1 (τ_1) and the corresponding relative intensities (I_1), respectively, as a function of depth. **e** and **f** are the positron lifetime components 2 (τ_2) and the corresponding relative intensities (I_2), respectively, as a function of depth. **g** represents the evolution of τ_1 and I_1 as a function of ion fluence at two representative Co_3O_4 depths of both top and bottom "sublayers". The lines connecting data points are guides to the eye.

Magneto-ionic behavior. To investigate the magneto-ionic behavior of the films, magnetoelectric measurements were carried by performing vibrating sample magnetometry while electrolyte-gating the films at

−50 V (see Methods for further details)[54,55]. Specifically, the magnetization M as a function of time t was recorded for 30 minutes while applying an external magnetic field high-enough (10000 Oe = 1 T) to ensure that the generated magnetization remains in a saturated state, thus enabling to determine M_S (t) as shown in Fig. 6a. The as-grown film shows a rather typical magneto-ionic response characterized by a gradual increase of saturation magnetization due to both the migration of O ions towards the liquid electrolyte, which acts as ion reservoir, and O ion redistribution within the film, leaving Co-rich areas that account for the generated ferromagnetism. The as-grown and all implanted Co_3O_4 films are overall paramagnetic with traces of ferromagnetism likely ascribed to impurities in the Si substrate (Fig. S3). Interestingly, implantation fluence has a very strong impact in the dependence of M_S vs. t. Using the behavior of the non-implanted film as reference, at an initial stage of voltage actuation ($i.e.$, first two minutes approximately), the film implanted to a fluence of 10^{14} ion/cm^2 shows a larger magneto-ionic rate, whereas that implanted to 10^{15} ion/cm^2 exhibits a much slower one as seen by the slope of the M_S vs. t. After this initial stage, both the as-grown and the film implanted to 10^{14} ion/cm^2 show a rather similar M_S evolution with time up to 8 min of voltage actuation. Conversely, in this time window, the film implanted to 10^{15} ion/cm^2 shows decreased saturation magnetization values but an increased slope, reaching the same M_S at 8 min as the as-grown film and that implanted to 10^{14} ion/cm^2. Beyond, while the as-grown film

tends to saturate, the films implanted to 10^{14} and 10^{15} ion/cm^2 keep on growing without levelling off, thus generating much larger magnetizations. At 30 min of voltage actuation, M_S values of 220, 314 and 465 are reached for the as-grown and films implanted to 10^{14} and 10^{15}, respectively. To summarize, taking the magneto-ionic behavior of the as-grown film as reference, low fluences (*i.e.*, 10^{14} ion/cm^2) result in both larger magneto-ionic rates and generated saturation magnetization at short and long voltage actuation times, respectively. Intermediate fluences (*i.e.*, 10^{15} ion/cm^2) lead to smaller magneto-ionic rates but largest generated saturation magnetization at short and long voltage actuation times, respectively.

Fig. 6b, 6c and 6d show the 2 first consecutive magnetization *vs.* applied magnetic field, M ($H_{applied}$), measurements taken just after switching off the applied voltage of an as-grown, and implanted films to 10^{14} and 10^{15} ion/cm^2, respectively. All films exhibit a slight depletion of the generated magnetization upon switching off the applied voltage, which tends to reach saturation for all samples after the second hysteresis loop measurement (thus, after 1 h since each loops takes 30 min to be recorded). In agreement with previously reported results, this process of magnetization depletion somewhat scales with the amount of generated magnetization by magneto-ionic means[24]. As seen in Fig. S4, although the evolution of coercivity (H_C) and squareness (M_R/M_S) with ion fluence exhibits a complex dependence, the film implanted to 10^{15} ion/cm^2 shows the most square-shaped hysteresis loops and the

second largest coercivity in agreement with the existence of rather uniform ferromagnetic regions immersed in a residual Co_3O_4 matrix[37,56].
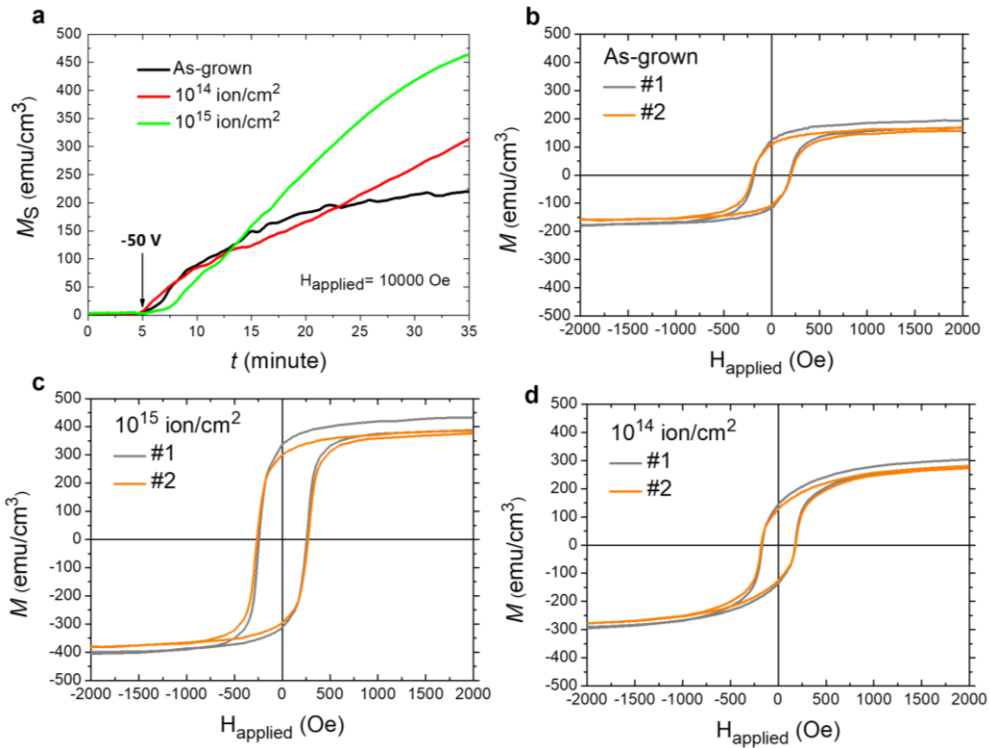
Fig. 6 Magneto-ionic behavior by vibrating sample magnetometry under voltage actuation. a Time t evolution of saturation magnetization M_S under an external magnetic field of 10000 Oe ($H_{applied}$) along the plane of the films while applying a voltage of -50 V. **b, c** and **d** are the 2 first consecutive magnetization vs. applied magnetic field, M ($H_{applied}$), measurements taken just after switching off the applied voltage of an as-grown, and implanted films to 10^{14} and 10^{15} ion/cm², respectively.

To further shed light on the magneto-ionic behavior, structural and compositional measurements of the films upon voltage actuation at -50 V for 30 min have been carried out by high-angle annular dark-field scanning transmission electron microscopy (HAADF-STEM), electron energy loss spectroscopy (EELS) and transmission electron microscopy (TEM). As seen in Fig. 7, upon voltage actuation, in contrast to the as-

grown film, the film implanted to 10^{15} ion/cm^2 clearly exhibits Co-rich areas (compare Fig. 7b with 7f). Moreover, the FFT of the region marked with an orange square corresponding to the high-resolution TEM image of the film implanted to 10^{15} ion/cm^2 yields a spot (number 5) corresponding to metallic Co, while no traces of it are present in the FFT of the region marked with an orange square corresponding to the high-resolution TEM image of the as-grown film. This is consistent with the magnetoelectric measurements, which indicate that, by magneto-ionic means, the film implanted to 10^{15} ion/cm^2 generates a significantly larger magnetization than the as-grown film (465 *vs*. 220 emu cm^{-3}). The distribution of Co-rich regions embedded in a Co oxide matrix (Fig. 7e and 7f) confirms that, on top of O ion migration towards the liquid electrolyte, O ion redistribution takes place within the film.

Furthermore, DBVEPAS and VEPALS measurements were carried out upon voltage actuation (Fig. 8). As seen in Fig. 8a, for all films, the S parameter becomes significantly enlarged upon voltage actuation across the whole depth of the films, indicating that voltage-driven ion motion leads to a different structural scenario from a defect viewpoint. As seen in Fig. 8b, defect size remains slightly increased for the as-grown, whereas the films implanted to 10^{14} and 10^{15} ion/cm^2 exhibit much larger defect sizes upon voltage actuation, suggesting that an enhanced magneto-ionic motion occurred in these films in concordance with magnetoelectric measurements, which reveal that these films yield the maximum values of generated magnetization (Fig.

6a). Upon looking at the evolution of τ_1 and the corresponding intensity I_1 along depth and comparing the curves with those of the films not subjected to voltage (Fig. 8c and 8d), on top of showing in general larger values of defect size (particularly, for the films implanted to 10^{14} and 10^{15} ion/cm^2), the I_1 values of these films become above 95 % across the top 21 nm (2,2 keV). At further depths, I_1 values start to decrease for the film implanted to 10^{15} ion/cm^2, whereas this decrease starts at a depth of around 39 nm (3,2 keV) for the film implanted to 10^{14} ion/cm^2. As seen in Fig. 8e and 8f, the increase in I_1 takes place in detriment to I_2, which becomes significant just at the bottom of the films. Anyhow, small mixed vacancy clusters become the majority defect type upon voltage actuation, suggesting that initial grain boundaries are seeds to initiate diffusion, rapidly transforming into smaller defects with diffusion.
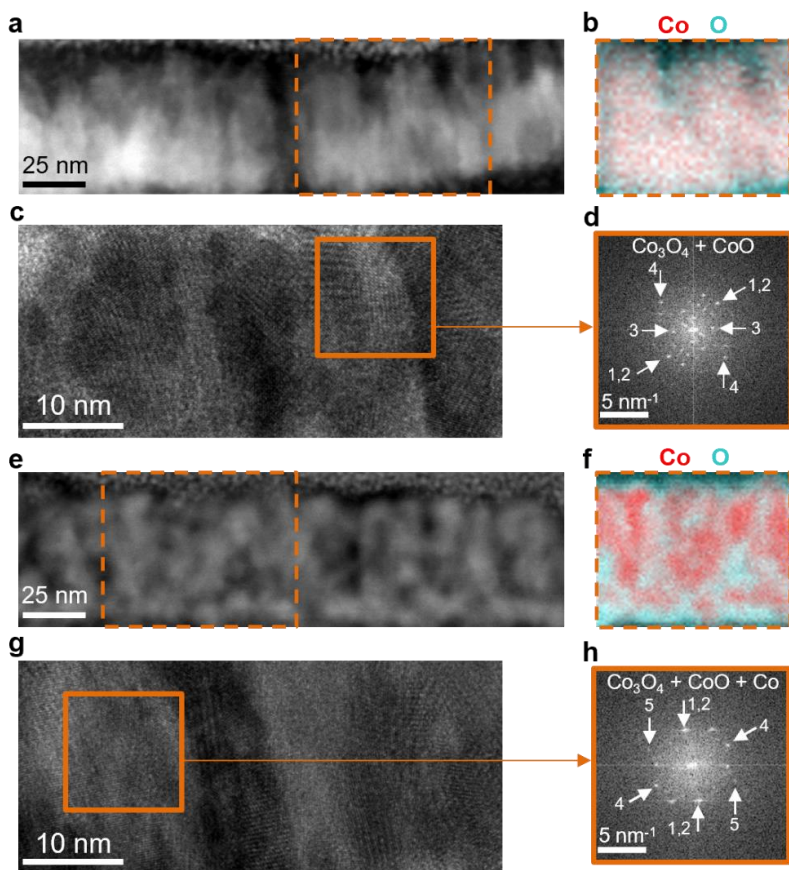
Fig. 7 Structural characterization after voltage actuation (-50 V for 30 min) of an as-grown Co_3O_4 film and a film implanted with 5 keV He ions to a fluence of 10^{15} ion/cm2 by high-angle annular dark-field scanning transmission electron microscopy (HAADF-STEM), electron energy loss spectroscopy (EELS) and transmission electron microscopy (TEM). a HAADF-STEM image of the cross-section of an as-grown Co_3O_4 film upon voltage actuation. **b** Co and O elemental EELS mappings of the region marked with an orange dashed rectangle in a. **c** High resolution TEM image of a top region of the cross section of the Co_3O_4 layer. **d** Fast Fourier transform of the region marked with an orange square in c. **e** HAADF-STEM image of the cross-section of a Co_3O_4 film implanted to 10^{15} ion/cm^2 upon voltage actuation. **f** Co and O elemental EELS mappings of the region marked with an orange dashed rectangle in e. **g** High resolution TEM image of a top region of the cross section of a Co_3O_4 film implanted to 10^{15} ion/cm^2 upon voltage actuation. **h** Fast Fourier transform of the region marked with an orange square in g. For panels d and h, "1" and "2" spots are consistent with (311) Co_3O_4 (PDF® 00-009-0418) and (111) CoO (PDF® 00-001-1227) interplanar distances (0.244 and 0.245 nm, respectively), while spots "3", "4" and "5" are unambiguously ascribed to (111) Co_3O_4 (PDF® 00-009-0418), (200) CoO (PDF® 00-001-1227) and (101) hexagonal close packed Co (PDF® 00-005-0727) interplanar distances (0.467, 0.212 and 0.191 nm, respectively).
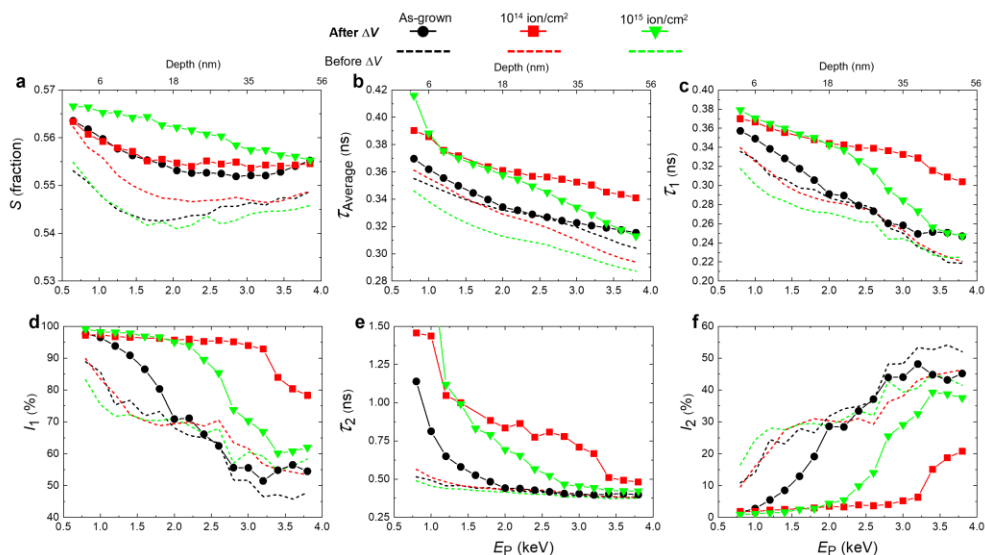
Fig. 8 Depth-resolved defect characterization of as-grown and implanted Co₃O₄ films upon voltage actuation (-50 V for 30 min) by Doppler broadening variable energy positron annihilation spectroscopy (DBVEPAS) and variable energy positron annihilation lifetime spectroscopy (VEPALS). **a** S parameter obtained by DBVEPAS characterization as a function of depth which can be also given in positron implantation energy (E_P). See Methods for further details. **b** Average lifetimes obtained by VEPALS as a function of depth. **c** and **d** are the positron lifetime components 1 (τ_1) and the corresponding relative intensities (I_1), respectively, as a function of depth. **e** and **f** are the positron lifetime components 2 (τ_2) and the corresponding relative intensities (I_2), respectively, as a function of depth. To serve as reference, DBVEPAS and VEPALS characterization of the as-grown and as-implanted films without being subjected to voltage actuation have been also included in panel in dashed lines. The lines connecting data points are guides to the eye.

Conclusions

Magneto-ionic targets consisting of 50 nm thick Co₃O₄ films with a highly nanostructured and defective preexisting microstructure were prepared by reactive sputtering. Specifically, mixed vacancy clusters below 10 vacancies are the majority defect type and decrease with depth in size from clusters of 10 down to 4 vacancies approximately. The as-grown films were then uniformly implanted with 5 keV He ions.

Due to the stochastic nature of ion implantation[32], the implantation results in a Gaussian-like depth profile with the maximum collisional damage located at a depth of around 18 nm, reaching half of this value at a depth of roughly 35 nm, thus leaving the bottom 15 nm of the Co_3O_4 film much less affected than the top counterpart. Here, by the interplay between the preexisting microstructure of the magneto-ionic target and a single implantation process, the magneto-ionic response, in terms of rate and amount of generated magnetization, of the target at short-, mid-, and long-term voltage actuation is controlled by varying the collisional damage along depth through ion fluence. In fact, the defect depth distribution is crucial to determine the time evolution of the magneto-ionic response since the oxygen ions of the magneto-ionic target become gradually available for diffusion with depth. In general, considering the as-grown film as reference, a mild collisional damage, characterized by a maximum displacement per atom (dpa) of around 0.01 (achieved upon implanting to 10^{14} ion/cm^2), tends to result in slightly larger vacancy clusters along the top 35 nm, whereas an intermediate collisional damage with a maximum dpa of roughly 0,1 (achieved upon implanting 10^{15} ion/cm^2) leads to smaller vacancy clusters, thus promoting and hindering ion motion at an early stage of voltage actuation, respectively. Conversely, the density of mixed vacancy clusters increases upon implantation across the bottom 15 nm, leading to a larger number of sites prone to diffuse which become enabled at long-term voltage actuation. This results in an enhanced

generated magnetization. The former hinders ion motion to the pronounced decrease in defect size, while the latter allows for ion intermixing with the Cu buffer layer due to the deeper penetration of He ions caused by the reduction in thickness of the Co_3O_4 film, thus hampering its role as working electrode. This proof-of-principle paves the way to further take advantage of ion implantation in terms of ion nature, energy, fluence, target temperature and multiple implantations for magneto-ionics.

Methods

Sample preparation: growth of the magneto-ionic targets & ion implantation

50 nm thick Co_3O_4 films were grown by reactive sputtering on B-doped, highly conducting [100]-oriented Si wafers (0.5 mm thick), previously coated with 20 nm of Ti and 60 nm of Cu. Depositions were carried always out while partly masking the Cu layer to serve afterwards as working electrode. The Co_3O_4 films were grown at room temperature in an AJA International ATC 2400 sputtering system with a base pressure around 5×10^{-8} Torr. High purity O_2 and Ar gases were used. The target to substrate distance was around 11 cm and the deposition rate of about 3 Å/s. Co_3O_4 was grown using O_2 and Ar flows of 1,7 and 17 sccm, respectively, at a total pressure of 3×10^{-3} Torr, resulting in an O/Ar flow ratio of 9,1 %/90,9%.

Then, the as-grown films were uniformly implanted at room temperature with 5 keV He ions at different fluences using a Helium-S system from Spin-Ion Technologies. The implantations were performed with an ion incidence angle of 7° with respect to the direction perpendicular to the sample surface to avoid ion channeling. The ion energy of 5 keV was adjusted to have the maximum collisional damage located at the first half of the Co_3O_4 film (specifically, at a depth around 18 nm), avoiding a pronounced atomic intermixing at the Co_3O_4/Cu interface which could be detrimental to the conductivity of the Cu buffer layer and, thus, harmful to its role as bottom electrode. Fluences of 10^{14} and 10^{15} ion/cm^2 were used to achieve dissimilar degrees of collisional damage, which expressed as displacement per atom (dpa) was 10^{-2} and 10^{-1}, respectively. Collisional damage profiles were simulated using the TRIM (TRansport of Ions in Matter) program, which is part of the SRIM (Stopping Range of Ions in Matter) package[53].

Magnetoelectric characterization

Magnetoelectric measurements were carried out by performing vibrating sample magnetometry while gating the films at room temperature using a homemade electrolytic cell filled with anhydrous propylene carbonate with solvated Na$^+$ and OH$^-$ ions (in a concentration range of 5–25 ppm with the aim to react with any traces of water) as liquid electrolyte[16,24,55]. A vibrating sample magnetometer from Micro Sense (LOT-Quantum Design) was used. Measurements of magnetic

moment *vs.* time under an external magnetic field of 1 T applied along the film plane (high enough to ensure that the generated magnetic moment remains saturated) were carried while applying -50 V between the Cu buffer layer, acting as working electrode, and a Pt wire, which acts as counter electrode, using an external Agilent B2902A power supply[16,24,55]. The sign of voltage was such that positive charges accumulate at the counter electrode when negative voltage is applied. After 30 min, the voltage was switched off and two consecutive hysteresis loops (*i.e.*, magnetic moment *vs.* applied magnetic field) were measured using a maximum applied magnetic field of 2 T. The loops were taken while sweeping the magnetic field from 2 T to -2 T and then, from -2 T back to 2 T. The magnetic moment is normalized to the initial volume of the Co_3O_4 given by multiplying the area exposed to the electrolyte and the film thickness. In all hysteresis loops, the signal at applied magnetic fields far above saturation fields is subtracted to remove linear contributions.

Structural and compositional measurements

High resolution transmission electron microscopy (HRTEM), high-angle annular dark-field scanning transmission electron microscopy (HAADF-STEM) and electron energy loss spectroscopy (EELS) were performed on a TECNAI F20 HRTEM /STEM microscope operated at 200 kV. Cross sectional lamellae were prepared by focused ion beam.

Defect characterization by Doppler broadening variable energy positron annihilation spectroscopy (DBVEPAS) & variable energy positron annihilation lifetime spectroscopy (VEPALS)

DBVEPAS measurements were conducted at the apparatus for *in-situ* defect analysis AIDA[57] of the slow positron beamline SPONSOR[58]. Positrons are accelerated and monoenergetically implanted into samples in the range between E_P = 0.05−35 keV, allowing for depth profiling. A mean positron implantation depth (given in nm) can be approximated using a simple material density ρ dependent formula as $\text{Depth (nm)} = \frac{36}{\rho\left(\frac{g}{cm^3}\right) \cdot E_P(keV)^{1,62}}$ [57]. This approximation does not account for positron diffusion and gives the best estimation for materials with large defect concentration, which show short positron diffusion lengths. When implanted into a solid, positrons lose their kinetic energy due to thermalization and, after short diffusion, annihilate in delocalized lattice sites or localize in vacancy-like defects and interfaces emitting usually two anti-collinear 511 keV gamma photons upon meeting electrons. Since, at the annihilation site, thermalized positrons have very small momentum compared to electrons, a broadening of the 511 keV line is observed mostly due to the momentum of electrons, which is measured with high-purity Ge detectors (with an energy resolution of 1,09 ± 0,01 keV at 511 keV). This broadening can be divided in three regions: a fraction which embraces the middle part of the annihilation line (510,07−511,93 keV) and two outer fractions (508,21−508,91 keV and

513,09–513,79 keV), which define the so-called S and W parameters, respectively. The S parameter is the fraction of positrons annihilating with low momentum valence electrons and represents vacancy type defects and their concentration. The W parameter accounts for the overlap of the positron wavefunctions with high momentum core electrons. Plotting S as a function of positron implantation energy, $S(E_P)$, provides depth dependent information, whereas S-W plots are used to examine atomic surrounding of the defect site and its size, which determines the type[59]. Positrons implanted into solids may form a hydrogen-like bound state with an electron, giving rise to the so-called positronium[46,60,61]. Positronium is formed on external or internal surfaces of solids by a thermalized positron picking an electron on the surface and escaping from solid into a pore or free space[62]. Depending on the orientation of electron and positron spin in the bound state, positronium decays in two photons (para-positronium, which is a singlet state) or three photons (ortho- positronium, triplet state). In solids, the three-photon decay of ortho-positronium is suppressed due to pick-off annihilation (two photon decay) with an electron with opposite spin from the environment[63,64]. Hence, the ratio of the "3γ2γ" is sensitive to the chemical environment of the positronium atom.

VEPALS measurements were conducted at the Mono-energetic Positron Source (MePS) beamline at Helmholtz-Zentrum Dresden – Rossendorf (Germany)[43] using a digital lifetime $CrBr_3$ scintillator detector, 51 mm in diameter (≈ 2 inch) and 25.4 mm in length (1 inch),

coupled to a Hamamatsu R13089-100 photomultiplier with a μ-metal shield and housed inside a solid Au casing with a homemade software employing a ADQ14DC-2X digitizer from SPDevices with a 14 bit vertical resolution and a 2GS/s (gigasamples per second) horizontal resolution[44] and with a time resolution function down to about 0.240 ns. The resolution function required for spectrum analysis uses two Gaussian functions with different intensities depending on the positron implantation energy, E_P, and appropriate relative shifts. All spectra contained at least 1×10^7 counts. A typical lifetime spectrum $N(t)$ is described by $N(t) = \Sigma(1/\tau_i)I_i \exp(-t/\tau_i)$, where τ_i and I_i are the positron lifetime and intensity of the i-th component, respectively ($\Sigma I_i = 1$). All the spectra were deconvoluted using the non-linearly least-squared based package PALSfit fitting software[45] into 3 discrete lifetime components, which directly evidence delocalized annihilation (i.e., bulk annihilation) and localized annihilation at 2 different defect types (or sizes: τ_1 and τ_2). The corresponding relative intensities reflect to a large extend the concentration of each defect type (size) if the size of compared defects is in the similar range. In general, positron lifetime is directly proportional to defects size, i.e., the larger is the open volume, the lower is the probability and longer it takes for positrons to be annihilated with electrons[41,42]. The positron lifetime and its intensity has been probed in function of positron implantation energy E_P or, in other words, implantation depth (thickness). The average positron lifetime $\tau_{Average}$ is

defined as $\tau_{Average} = \Sigma\tau_i I_i$ and it has a high sensitivity to the defect size (type).

Ab initio calculations of positron lifetimes

Ab initio calculations of positron lifetimes for different possible defect configurations were performed employing the so-called atomic superposition technique ATSUP[47]. The electron-positron correlations were treated according to Boroński-Nieminen[48] and the gradient-correction scheme with $\alpha = 0.22$[49].

References

1. Ramesh, R. & Manipatruni, S. Electric field control of magnetism. *Proc. R. Soc. A.* **477**, 20200942 (2021).

2. Does AI have a hardware problem? [Editorial]. *Nat. Electron.* **1**, 205–205 (2018).

3. Big data needs a hardware revolution [Editorial]. *Nature* **554**, 145–146 (2018).

4. Song, C., Cui, B., Li, F., Zhou, X. & Pan, F. Recent progress in voltage control of magnetism: materials, mechanisms, and performance. *Prog. Mater. Sci.* **87**, 33–82 (2017).

5. Hu, J.-M. & Nan, C.-W. Opportunities and challenges for magnetoelectric devices. *APL Mater.* **7**, 080905 (2019).

6. Molinari, A., Hahn, H. & Kruk, R. Voltage-control of magnetism in all-solid-state and solid/liquid magnetoelectric composites. *Adv. Mater.* **31**, 1806662 (2019).

7. Honnali, S. *et al.* Advances in magneto-ionic materials and perspectives for their application. *APL Mater.* **9**, 030903 (2021).

8. De Rojas, J. *et al.* Voltage control of magnetism with magneto-ionic approaches: beyond voltage-driven oxygen ion migration. *Appl. Phys. Lett.* **120**, 070501 (2022).

9. Tan, A. J. *et al.* Magneto-ionic control of magnetism using a solid-state proton pump. *Nat. Mater.* **18**, 35–41 (2019).

10. Gößler, M. *et al.* Magneto-ionic switching of superparamagnetism. *Small* **15**, 1904523 (2019).

11. Chen, G. *et al*. Reversible writing/deleting of magnetic skyrmions through hydrogen adsorption/desorption. *Nat. Commun.* **13**, 1350 (2022).

12. Lu, N. *et al*. Enhanced low-temperature proton conductivity in hydrogen-intercalated Brownmillerite oxide. *Nat. Energy* **7**, 1208–1216 (2022).

13. Dasgupta, S. *et al*. Intercalation-driven reversible control of magnetism in bulk ferromagnets. *Adv. Mater.* **26**, 4639–4644 (2014).

14. Dasgupta, S. *et al*. Toward on-and-off magnetism: reversible electrochemistry to control magnetic phase transitions in spinel ferrites. *Adv. Funct. Mater.* **26**, 7507–7515 (2016).

15. Zhu, X. *et al*. In situ nanoscale electric field control of magnetism by nanoionics. *Adv. Mater.* **28**, 7658–7665 (2016).

16. de Rojas, J., *et al*. Voltage-driven motion of nitrogen ions: a new paradigm for magneto-ionics. *Nat. Commun.* **11**, 5871 (2020).

17. De Rojas, J. *et al*. Magneto-ionics in single-layer transition metal nitrides. *ACS Appl. Mater. Interfaces* **13**, 30826–30834 (2021).

18. De Rojas, J. *et al*. Critical role of electrical resistivity in magnetoionics. *Phys. Rev. Appl.* **16**, 034042 (2021).

19. Tan, Z. *et al*. From binary to ternary transition-metal nitrides: a boost toward nitrogen magneto-ionics. *ACS Appl. Mater. Interfaces* **14**, 44581–44590 (2022).

20. Tan, Z. *et al*. Frequency-dependent stimulated and post-stimulated voltage control of magnetism in transition metal nitrides: towards brain-inspired magneto-ionics. *Mater. Horiz.* **10**, 88–96 (2023)

21. Bauer, U. *et al*. Magneto-ionic control of interfacial magnetism. *Nat. Mater.* **14**, 174–181 (2015).

22. Gilbert, D. A. *et al*. Structural and magnetic depth profiles of magneto-ionic heterostructures beyond the interface limit. *Nat. Commun.* **7**, 12264 (2016).

23. Ibrahim, F., Hallal, A., Dieny, B. & Chshiev, M. Establishing characteristic behavior of voltage control of magnetic anisotropy by ionic migration. *Phys. Rev. B* **98**, 214441 (2018).

24. Quintana, A. *et al*. Voltage-controlled ON-OFF ferromagnetism at room temperature in a single metal oxide film. *ACS Nano* **12**, 10291–10300 (2018).

25. de Rojas, J., *et al*. Boosting room-temperature magneto-ionics in a non-magnetic oxide semiconductor. *Adv. Funct. Mater.* **30**, 2003704 (2020).

26. Martins, S. *et al*. Dynamic electric-field-induced magnetic effects in cobalt oxide thin films: towards magneto-ionic synapses. *Nanoscale* **14**, 842-852 (2022).

27. Vasala, S. *et al*. Reversible tuning of magnetization in a ferromagnetic Ruddlesde–Popper-type manganite by electrochemical fluoride-ion intercalation. *Adv. Electron. Mater.* **6**, 1900974 (2020).

28. Dabrowski, J. Point defect assisted diffusion in semiconductors. *Solid State Phenom.* **71**, 23–50 (2000).

29. Atkinson, A. & Monty, C. Grain boundary diffusion in ceramics. In: Dufour, L. C., Monty, C. & Petot-Ervas, G. (eds) Surfaces and interfaces of ceramic materials. NATO ASI Series, Vol. 173. Springer (1989).

30. Wang, R., *et al*. Twin boundary defect engineering improves lithium-ion diffusion for fast-charging spinel cathode materials. *Nat. Commun.* **12**, 3085 (2021).

31. Baktash, A., Demir, B. Yuan, Q. & Searles, D. J. Effect of defects and defect distribution on Li-diffusion and elastic properties of anti-perovskite Li_3OCl solid electrolyte. *Energy Storage Mater.* **41**, 614–622 (2021).

32. Nastasi, M. & Mayer, J. W. In: Ion implantation and synthesis of materials. Springer (2006).

33. Fassbender, J., Ravelosona, D. & Samson, Y. Tailoring magnetism by light-ion implantation. *J. Phys. D Appl. Phys.* **37**, R179–R196 (2004).

34. Chappert, C. *et al*. Planar patterned magnetic media obtained by ion implantation. *Science* **280**, 1919–1922, (1998).

35. Fassbender, J. *et al*. Ion mass dependence of implantation-induced local creation of ferromagnetism in $Fe_{60}Al_{40}$ alloys. *Phys. Rev. B* **77**, 174430 (2008).

36. Menéndez, E. *et al*. Out-of-plane magnetic patterning on austenitic stainless steels using plasma nitriding. *Appl. Phys. Lett*. **96**, 242509 (2010).

37. Menéndez, E. *et al*. Improving the magnetic properties of Co-CoO systems by designed oxygen implantation profiles. *ACS Appl. Mater. Interfaces* **5**, 4320–4327 (2013).

38. Modarresi, H. *et al*. Induced ferromagnetism and magnetoelectric coupling in ion-beam synthesized $BiFeO_3$-$CoFe_2O_4$ nanocomposite thin films. *J. Phys. D: Appl. Phys*. **49**, 325302 (2016).

39. Jensen, C. J. *et al*. Ion irradiation and implantation modifications of magneto-ionically induced exchange bias in Gd/NiCoO. J. Magn. Magn. Mater. 540, 168479 (2021).

40. Juge, R. *et al*. Helium ions put magnetic skyrmions on the track. *Nano Lett*. **21**, 2989–2996, (2021).

41. Krause-Rehberg, R. & Leipner, H. In: Positron annihilation in semiconductors: defect studies. Springer (1999).

42. Tuomisto, F. & Makkonen, I. Defect identification in semiconductors with positron annihilation: experiment and theory. *Rev. Mod. Phys*. **85**, 1583–1631 (2013).

43. Wagner, A., Butterling, M., Liedke, M. O., Potzger, K. & Krause-Rehberg, R. Positron annihilation lifetime and Doppler broadening spectroscopy at the ELBE facility. *AIP Conf. Proc*. **1970**, 040003 (2018).

44. Hirschmann, E. *et al.* A new system for real-time data acquisition and pulse parameterization for digital positron annihilation lifetime spectrometers with high repetition rates. *J. Instrum.* **16**, P08001 (2021).

45. Olsen, J. V., Kirkegaard, P., Pedersen, N. J. & Eldrup, M. PALSfit: a new program for the evaluation of positron lifetime spectra. *Phys. Stat. Sol. (c)* **4**, 4004–4006 (2007).

46. Schultz, P. J. & Lynn, K. G. Interaction of positron beams with surfaces, thin films, and interfaces. *Rev. Mod. Phys.* **60**, 701–779 (1988).

47. Puska, M. J. & Nieminen, R. M. Defect spectroscopy with positrons: a general calculational method. *J. Phys. F: Met. Phys.* **13**, 333–346 (1983).

48. Boroński, E. & Nieminen, R. M. Electron-positron density-functional theory. *Phys. Rev. B.* **34**, 3820–3831 (1986).

49. Barbiellini, B., Puska, M. J., Torsti, T. & Nieminen, R. M. Gradient correction for positron states in solids. *Phys. Rev. B.* **51**, 7341–7344 (1995).

50. Bola George, H. *et al.* Ion-sculpting of nanopores in amorphous metals, semiconductors, and insulators. *Appl. Phys. Lett.* **96**, 263111 (2010).

51. Fellman, A., Sand, A. E., Byggmästar, J. & Nordlund, K. Radiation damage in tungsten from cascade overlap with voids and vacancy clusters. *J. Phys.: Condens. Matter* **31**, 405402 (2019).

52. Agarwal, S. *et al*. A new mechanism for void-cascade interaction from nondestructive depth-resolved atomic-scale measurements of ion implantation-induced defects in Fe. *Sci. Adv.* **6**, eaba8437 (2020).

53. http://srim.org/. The TRIM (Transport of Ions in Matter) program is included in the SRIM (Stopping Range of Ions in Matter) package (SRIM-2016).

54. Leighton, C. Electrolyte-based ionic control of functional oxides. *Nat. Mater.* **18**, 13–18 (2019).

55. Navarro-Senent, C., Quintana, A., Menéndez, E., Pellicer, E. & Sort, J. Electrolyte-gated magnetoelectric actuation: phenomenology, materials, mechanisms and prospective applications. *APL Mater.* **7**, 030701 (2019).

56. Leslie-Pelecky, D. L. & Rieke, R. D. Magnetic properties of nanostructured materials. *Chem. Mater.* **8**, 1770–1783 (1996).

57. Liedke, M. O. *et al*. Open volume defects and magnetic phase transition in $Fe_{60}Al_{40}$ transition metal aluminide. *J. Appl. Phys.* **117**, 163908 (2015).

58. Anwand, W., Brauer, G., Butterling, M., Kissener, H. R. & Wagner, A. Design and construction of a slow positron beam for solid and surface investigations. *Defect Diffus. Forum.* **331**, 25–40 (2012).

59. Clement, M., de Nijs, J. M. M., Balk, P., Schut, H. & van Veen, A. Analysis of positron beam data by the combined use of the shape- and wing-parameters. *J. Appl. Phys.* **79**, 9029–9036 (1996).

60. Charlton, M. & Humberston, J. W. Positron Physics. Cambridge University Press (2000).

61. Coleman, P. G., Sharma, S. C. & Diana, L. M. Positronium formation in condensed matter and high-density gases. North-Holland (1982).

62. Hodges, C. H. & Stott, M. J. Work functions for positrons in metals. *Phys. Rev. B.* **7**, 73–79 (1973).

63. Tao, S. J. Positronium annihilation in molecular substances. *J. Chem. Phys.* **56**, 4654 (1972).

64. Eldrup, M., Lightbody, D. & Sherwood, J. N. The temperature dependence of positron lifetimes in solid pivalic acid. *Chem. Phys.* **63**, 51–58 (1981).

Supplementary Information
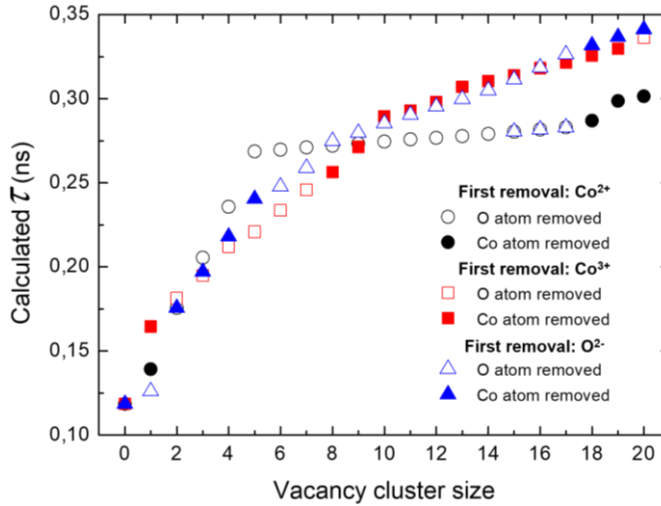
Fig. S1 *Ab initio* calculation of the positron lifetime τ as a function of vacancy cluster (assumed spherical) size in Co_3O_4 depending on the nature of the first removed atom. Co_3O_4 has a spinel crystal structure, in which 2 types of Co atoms (*i.e.*, Co^{2+} and Co^{3+}) can be distinguished due to the different atomic surrounding. Conversely, the environment is always the same for O.
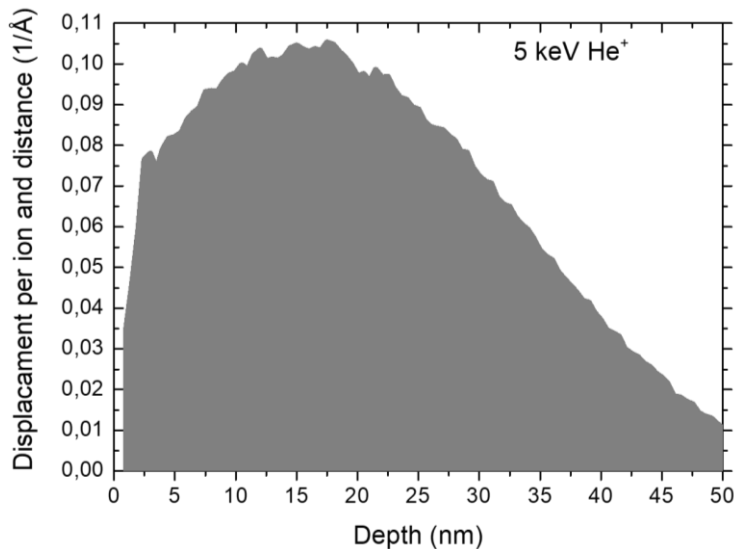
Fig. S2 TRIM (TRansport of Ions in Matter) simulation of the depth-resolved collisional damage, given in number of target displacements per impinging ion and crossed distance, of 5 keV He ions colliding with Co_3O_4.
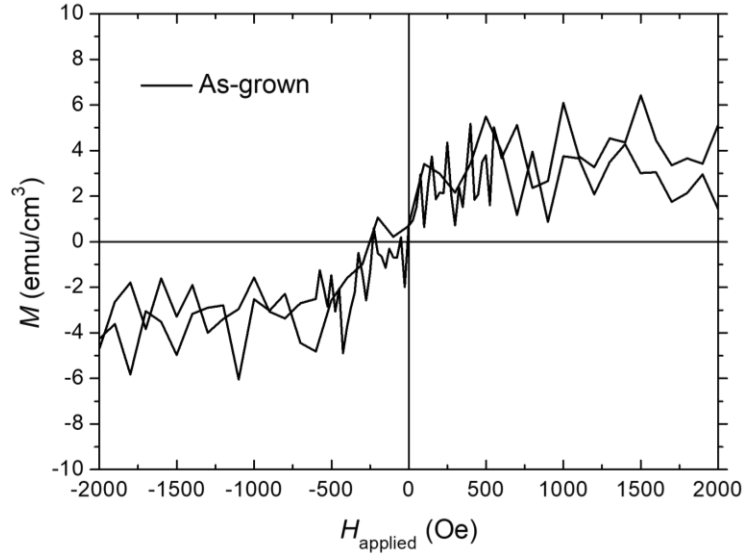
Fig. S3 Magnetization *vs.* applied magnetic field, M ($H_{applied}$), measurements of an as-grown Co_3O_4 film by vibrating sample magnetometry along the plane of the film.
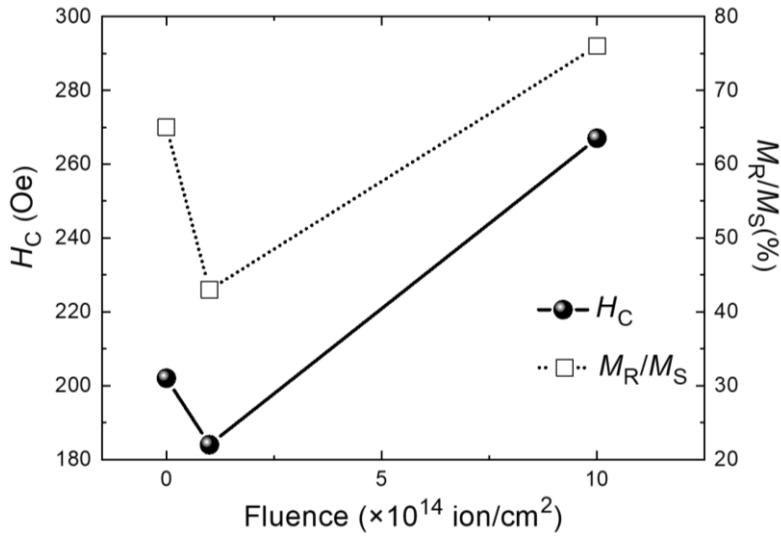
Fig. S4 Evolution of coercivity (H_C) and squareness (M_R/M_S) as a function of ion fluence. Both H_C and M_R/M_S values are extracted from the ascending branch of the 2nd consecutive hysteresis loop measured upon switching the voltage off. In this way, a stable magnetic state magnetization is ensured since magnetization depletion is virtually vanished. Note that hysteresis loops are recorded from positive to negative applied magnetic fields (descending branch) and then, from negative to positive values (ascending branch).

GENERAL

DISCUSSION
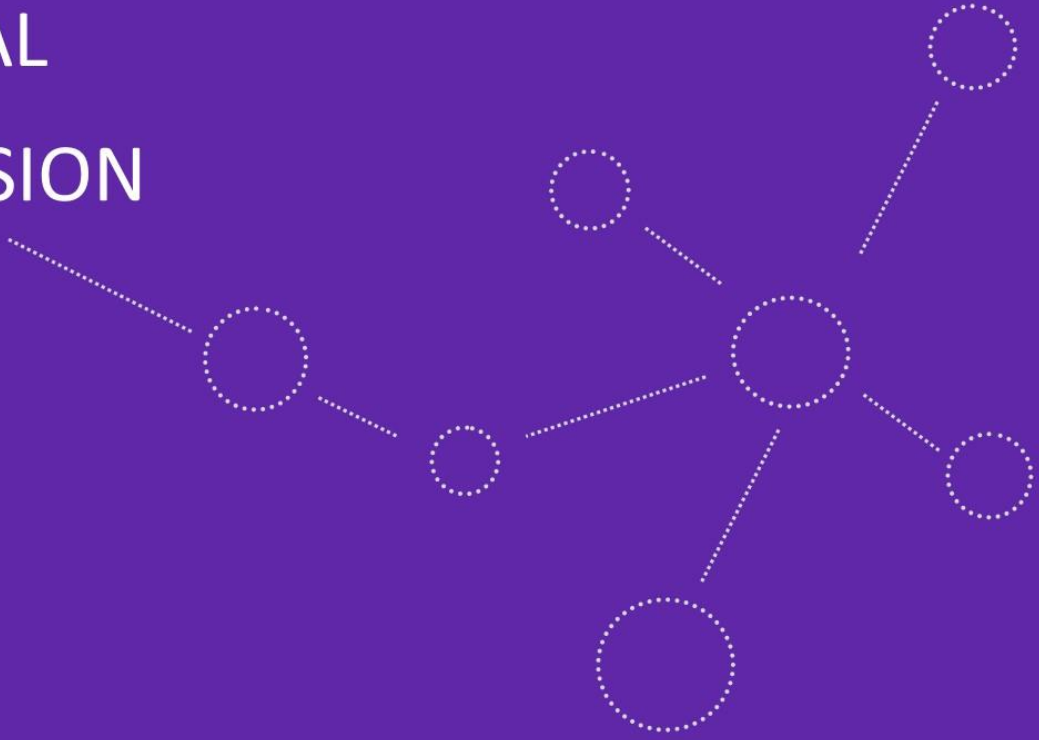
This thesis provides important improvements for magneto-ionic systems relying on oxygen motion in Co-oxide films. Voltage-induced oxygen migration were boosted using three different approaches, solving different challenges one by one, as shown in table 1.

Table 1 Challenges and respective solutions for each identified limitation in magneto–ionics of Co_3O_4 system

	Challenge	Solution	How?	Chapters
1	Low magneto--ionic rate	Increase electric field inside the film	**Decreasing Co-oxide film thickness**	3.1
2	Too large V_G	Increase EDL strength	**Adding salts to PC**	3.2
3	Small generated magnetization	Engineer depth-resolved defect density	**Ion Irradiation**	3.3

By thickness reduction from >200 nm to 5 nm, sub-second ON-OFF transition rates were achieved in electrolyte-gated paramagnetic cobalt oxide films. Our magneto-ionic system displayed interesting features such as operational dynamic range that may be useful for the creation of artificial neural networks whose magnetic

properties would be controlled by applied voltage (*i.e.*, magneto-ionic synapses).

To further enhance the EDL strength, we focused our attention to the composition of the PC electrolyte. In other words, we put the focus to the electrolyte composition instead of actuating on the metal oxide thin film or the working conditions, which are the typical approaches followed in the literature. Inspired by energy storage devices, such as battery electrolytes, we demonstrated that the ionic strength of the electrolyte plays an important role in magneto-ionics. To this end, different inorganic salts were added to PC, namely potassium iodide (KI), potassium chloride (KCl) and calcium tetrafluoroborate (Ca(BF$_4$)$_2$) at concentrations below their corresponding solubility limits.

Finally, since magneto-ionics is a diffusion-controlled mechanism of ions. We exploited the potential of light ion implantation of He$^+$ to engineer depth-resolved defect density we obtained novel results controlling the oxygen mobility though the Co-oxide thickness.

In the following, aspects not covered in chapter 3 are discussed here.

Ideally, the solutions implemented in each work should be combined altogether to achieve a synergistic effect. However, each challenge/solution was applied one by one to investigate its impact on

the magneto-ionic response and to find out optimum experimental conditions (*i.e.,* thickness of the Co-oxide layer, salt type and concentration, best ion irradiation conditions). The three independently optimized solutions could be merged in a final study.

Although in the first paper largest saturation magnetisation and faster magneto-ionic response were observed in the 5 nm-thick Co-oxide films, slightly thicker counterparts were investigated in the second study. There were two main reasons for this selection: (*i*) the two studies were carried out in parallel, and it was not yet clear at the beginning of the second study which thickness worked best, (*ii*) both 5 nm- and 15 nm-thick Co-oxide films had the same phase (*i.e.* mainly CoO). In the third study related to defect engineering, Co_3O_4 films of 50 nm were selected to facilitate the characterization of the defects generated through light ion implantation by DBVEPAS and VEPALS. Note that the simulated collisional damage predicts that the central region of the 50 nm-thick films is affected, while the bottom and upper parts become less damaged (recall the Gaussian profile). This was done in purpose to avoid having an effect at the interface between the Co-oxide film and the Cu seed-layer. The irradiation of 5 nm-thick films would for sure be possible using lower energies which, in principle, would render highly homogeneous damage across the film thickness. However, the Co-oxide / Cu interface would as well become heavily affected (e.g., through an intermixing of phases). To avoid this issue, multiple ion irradiation steps (instead of a single irradiation experiment) could be

performed to have better control on the collisional damage and, hence, on the density and nature of the defects generated. In any case, any of the aforementioned possibilities (irradiation of thinner films and/or the application of multiple irradiation schemes) should be investigated in detail to clarify whether they bring or not a benefit to the magneto-ionic response of the Co-oxide films.

AIMD simulations were consistent with the magneto-ionic response of the Co-oxide films assayed in PC supplemented with different salts. The results suggested the formation of a more effective EDL when KI instead of KCl was dissolved in PC. Although the AIMD simulations were carried out under open circuit conditions (i.e., the Co-oxide film was not externally biased), the application of an electric field would enhance the EDL strength, since a larger amount K^+ ions would be attracted towards the Co-oxide/electrolyte interface and, simultaneously, I^- ions would be repelled more efficiently. The addition of salts clearly improved the magneto-ionic rate but the cyclability could not be extended beyond a few cycles. Chemical reactions between the material and iodide ions were thought to compromise the cyclability of the system. Indeed, signs of delamination were noticed upon cycling. To overcome this issue, different inorganic salts not involving halogen elements, which are highly electronegative, could be tested. On the other hand, an issue which remained unexplored within this Thesis is the characterization of the reactions taking place at the counter electrode, since bubbling was observed in some cases (e.g., when $Ca(BF_4)_2$ dissolved in PC was used

as electrolyte). The electrode set-up configuration also deserves further consideration. If one wishes to determine the exact voltage at the Co-oxide film, a three-electrode configuration (working electrode –the Co-oxide film–, pseudo-reference electrode, and counter electrode) should be used. However, we anticipate that the voltage difference for two and three electrodes is not that large under our experimental conditions (highly resistive electrolyte). In any case, electrolyte engineering in magneto-ionic systems is definitely a novel approach to enhance the energy efficiency in voltage actuation, since much lower voltages are required to switch the magnetization of Co-oxide, thus decreasing Joule heating dissipation.

Remarkably, we demonstrated that the amount of generated magnetization in 50 nm thick Co_3O_4 films can be controlled by modifying the ion fluence-generated collisional damage. An intermediate collisional damage with a maximum displacement per atom (dpa) of 0.1 were achieved upon implantation of 10^{15} ion/cm^2, which generated small vacancy clusters, which in turn promoted or inhibited ion mobility early in the voltage actuation process. Finally, it is worth mentioning that the magneto-ionic rate and the saturation magnetization achieved upon application of -50 V in the irradiated 50 nm-thick Co_3O_4 films were similar to those measured for non-irradiated (i.e., as-grown) 20 – 30 nm thick films. We hypothesize that the irradiation of the latter would enhance their magneto-ionic

performance. However, issues related to the damage induced at the Co-oxide / Cu interface should be considered.

Finally, although 5 nm-thick CoO films were demonstrated to yield faster magneto-ionic response under electrolyte-gating, the stability in air of such films (specially when partially reduced to form CoO_x + Co) is worse than for thicker films. Since these layers are not protected, passivation would be particularly an issue for ultra-thin films (or small metallic Co clusters which could be easily become re-oxidized). So, the interplay between the various factors may render intermediate thicknesses as the most suitable ones.

CONCLUSIONS
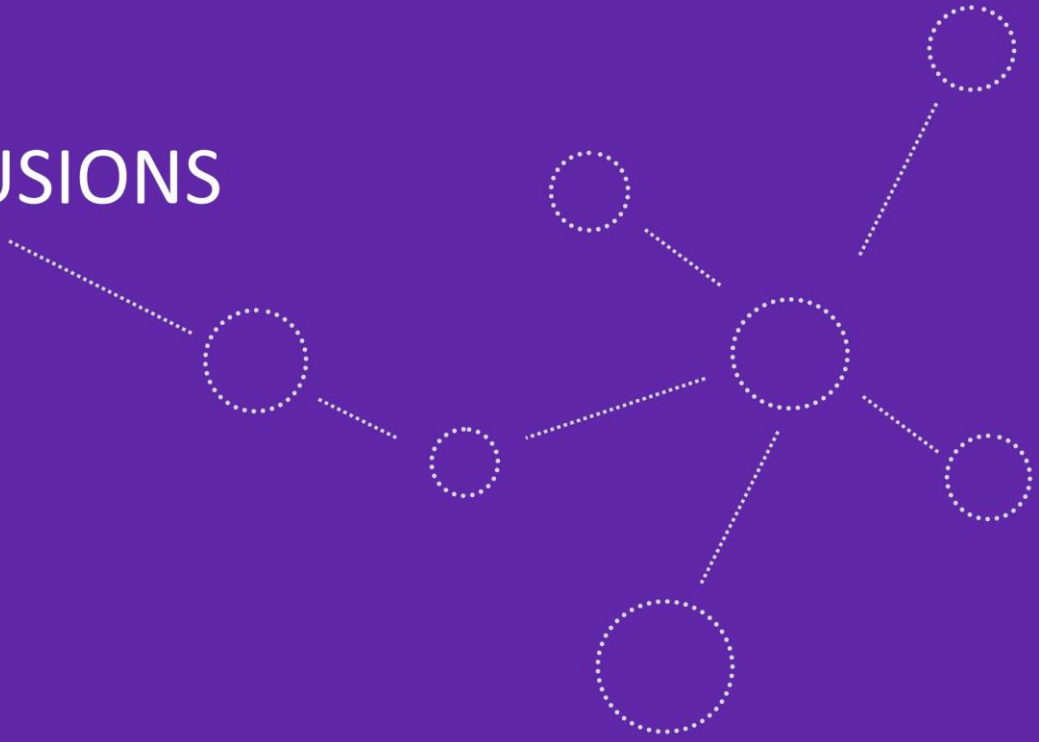
The following list of bullet points provides a summary of the main conclusions drawn from this Thesis:

- Our results demonstrate a strong **film-thickness dependence** of the strength of the magneto-ionic effect in electrolyte-gated paramagnetic cobalt oxide films. Thinner films achieve dramatically higher magneto-ionic rates than thicker ones, by a factor of 134 larger in 5 nm than for 230 nm films. Higher M_S was achieved for the thinner samples of 5 nm by a factor of 18 larger than for 230 nm. Remarkably, pulsed voltages can be used to generate meaningful cumulative magneto-ionic effects that emulate potentiation and plasticity of biological synapses. According to cumulative magneto-ionic effects at 100 Hz, activation times in the 5 nm-thick films are on the order of 10^{-2} s, making these magneto-ionic systems based on oxygen ion migration the fastest reported to date. Our results provide a significant contribution to the usability of magneto-ionics in practical applications like neuromorphic computing, which operates at rates comparable to those attained in this work.

- **By exploiting the electrolyte engineering** approach, we demonstrate a remarkable improvement of the magneto-ionic motion in 15 nm-thick Co oxide films. Inorganic salts were added to PC to produce faster magneto-ionic rates and a higher generation of magnetization. By doing this, the medium's ionic strength is raised, which results in a stronger electric field upon biasing at the

Co oxide/electrolyte interface. As a result, oxygen mobility within the material is promoted, allowing for faster and more abundant formation of metallic cobalt.

- We have exploited the potential of **ion implantation to engineer depth-resolved defect density** and type with the aim to control the magneto-ionic behavior of Co_3O_4 thin films. We demonstrate that, by the interplay between the highly nanostructured nature of the magneto-ionic target (*i.e.*, 50 nm thick Co_3O_4 film) and a single implantation process of light ions (He^+) at 5 keV, the magneto-ionic response, in terms of rate and amount of generated magnetization, of the Co_3O_4 film at short-, mid-, and long-term voltage actuation can be controlled by varying the generated collisional damage through ion fluence. This proof-of-principle paves the way to further exploit ion implantation in relation to ion nature, energy, fluence, target temperature and multiple implantations for magneto-ionics.

FUTURE

PERSPECTIVES

CHAPTER 6

Based on the novelty and significance of this Thesis, several possibilities arise to further boost the studied magneto-ionic system:

- To combine the improvements achieved in this Thesis in the same experiment: 5 nm-thick Co-oxide film irradiated with a single implantation process of He$^+$ at 5 keV for a fluence of 10^{15} ions/cm^2 electrolyte-gated in KI-containing PC at −1.5 V vs. pseudo-reference Pt electrode.

- To test counter-electrode geometries with larger areas (*e.g.*, mesh-like electrode) to increase and homogenize the electric field strength at the target material (*i.e.*, Co-oxide) surface.

- To study the magneto-ionic behavior of Co-oxide films in the presence of ionic liquids (*e.g.*, 1-ethyl-3-methylimidazolium bis(trifluoromethylsulfonyl)imide, EMI-TFSI).

- To replace the liquid electrolyte by a solid-state electrolyte such as HfO$_x$ or GdO$_x$ to move towards device applicability.

- To produce arrays of magneto-ionic dots by lithography to be individually actuated with different voltage protocols.

- To use other ions for implantation in Co-oxide, considering different doses and fluences, for further tuning of the collisional damage.

CURRICULUM VITAE

SOFIA MARTINS
MICRO & NANOTECH ENGINEER

Phone: +34 673811284 | **E-mail**: csg.martins12@gmail.com | **Skype**: cgs.martins12 |
LinkedIn: /in/sofia-martins-1602 | **Address**: Barcelona, Spain | **ORCID**: 0000-0002-1801-1651

Hey! I am currently a predoctoral fellow at UAB funded by the BeMAGIC project, with in-depth knowledge in Microelectronics, Nanofabrication Processes and Smart Materials. I am very passionate about integrated devices and nanomechanics. My **focus** is to increase the early adoption of nanotechnology in everyday life, through the development of more practical applications. I have **research experience** using cleanroom processes to funtionalize surfaces, produce nanofabricate devices and characterize it. Working together with people to achieve an objective has revealed to be a rewarding experience. So driving to work together and seeing a creation / project come to light is job to long for.

Internship CenTI 2014	Graduate Student Researcher 2016	MSc Degree FCT/UNL 2016	Semiconductors Industry Trainee 2017	Cleanroom Engineer 2018	Early Stage Reseacher 2020
Centre for Nanotechnology and Smart Materials, Famalicão, Portugal	Universidade de São Paulo, São Paulo, Brazil	NOVA University of Lisbon, Portugal	AMKOR Technology, Vila do Conde, Porto, Portugal	International Iberian Nanotechnology Lab, Braga, Portugal	Universitat Autónoma de Barcelona, Spain

Professional Experience

Early Stage Researcher in BeMAGIC Project [Mar 2020 - Current]
Group of Smart Nanoengineered Materials, Nanomechanics and Nanomagnetism
Supervisors: Jordi Sort | Enric Menéndez | Eva Pellicer
Doctoral Thesis: Boosting magneto-ionic effects in co-oxide films by electrolyte-gating
Use magneto-ionic effects in Co oxide which allow for voltage-driven on-off ferromagnetism, to implement ultra-secure and energy-efficient spintronic devices
Secondment: 1 month in Aalto University (Helsinki, Finland) and 1 month in Spin-Ion Technologies (Orsay, France)
BeMAGIC Project is a Training Programme on Energy-Efficient Magnetoelectric Nanomaterials for Advanced Information and Healthcare Technologies (https://bemagic-etn.eu/)

Cleanroom Engineer [Feb 2018 - Jan 2020]
Microfabrication and Exploratory Nanotechnology (MeN) Group
Group Leader: João Gaspar | Provide micro and nanofabrications solutions on substrates from 200-mm-diameter wafers throughout all development chain in cleanroom processes: device modelling and design, process integration, device fabrication, characterization and test.

R&D Engineer Trainee [Jun 2017 - Feb2018]
Adviser: André Cardoso | Integration of new processes on production line and development of technoogy for European project about Internet of Things | Lab On Chip | System in package

R&D Master Thesis in Micro & Nanotechnology Engineer [Jan 2016 - Jul 2016]
"Optimization of Printed TIPS-Pentacene Thin-Film Applied on OFET Technology"
Adviser: Prof. Roberto Faria | Jury: Prof. Rodrigo Martins, Prof. Elvira Fortunato, Prof. Luis Pereira. Master thesis project based on the development of a p-OFETs and its respective resistor transistor inverter, using inkjet printing techniques to the fabrication and characterization.

Curricular Internship [Jan 2014 - Fev 2014]
Design and dimensioning of a spin coater in order to optimize thin film printing.

Areas of Expertise

Cleanroom Processes and Characterization
-Thin Film Deposition and Material Growth
-Optical Lithography:
-Etching, Ashing and Micromachining
-Metrology and Inspections Techniques
-Magnetic Characterization Tools

Personal Skills

Curiosity	● ● ● ● ●
Creative	● ● ● ● ○
Initiative	● ● ● ● ○
TeamWork	● ● ● ● ●
Organization	● ● ● ● ●

Languages

Portuguese	● ● ● ● ●
English	● ● ● ● ○
Spanish	● ● ● ● ○

Additional Skills

-AutoCAD
-Adobe Illustrator
-KLayout
-Adobe Photoshop
-Origin
-Conventor Simulator 3D
-Wolfram Mathematica
-LaTeX

SOFIA MARTINS
MICRO & NANOTECH ENGINEER

Phone: +34 673811284 | **E-mail**: csg.martins12@gmail.com | **Skype**: cgs.martins12 |
LinkedIn: /in/sofia-martins-1602 | **Address**: Barcelona, Spain | **ORCID**: 0000-0002-1801-1651

Publications

- Enhancing magneto-ionic efects in cobalt oxide films by electrolyte enginering. S. Martins, Z. Ma, X. S.-Monfort, M. Sodupe, L.R.-Santiago, E. Menéndez, E. Pelicer, J. Sort. Nanoscale Horizons, (2022). **IF=11.684**

- From Binary to Ternary Transition-Metal Nitrides: A Boost toward Nitrogen Magneto-Ionics. Z. Tan, S. Martins, M. Escobar, J. de Rojas, F. Ibrahim, M. Chshiev, A. Quintana, A. Lopeandia, J. L. C-Kramer, E. Menéndenz. ACS Aplied Materials & Interfaces, 14, 44581-4590 (2022). **IF= 9.229**

- Frequency-dependent stimulated and post-stimulated voltage control of magnetism in transition metal nitrides: towards brain-inspired magneto-ionics. Z. Tan, J. de Rojas, S. Martins, A.Lopeandia, A. Quintana, M. Cialone, J. H. -Martín, J. Meersschaut, A. Vantomme, J. L Costa-Krämer, J. Sort, E. Menéndez. Materials Horizons, 2022. **IF=13.266**

- Dynamic electric-field-induced magnetic effects in cobalt oxide thin films: towards magneto-ionic synapses. S. Martins, J. Rojas, Z. Tan, M. Cialone, A. Lopeandia, J. H.-Martín, J. L Costa-Krämer, E.Menéndez, J. Sort. Nanoscale, 14, 842-852 (2022). **IF= 8.307**

- Surface Texture Detection With a New Sub-mm Resolution Flexible Tactile Capacitive Sensor Array for Multimodal Artificial Finger. E. Sotgiu, D. E. Aguiam, C. Calaza, J. Rodrigues, J. Fernandes, B. Pires, E. E. Moreira, F. Alves, H. Fonseca, R. Dias, S. Martins, J. Gaspar. Journal of Microelectromechanical Systems, 29, 629-636 (2020). **IF=2.417**

- An efficient and deterministic photon management using deep subwavelength features.A. Prajapati, J. Llobet, M. Antunes, S. Martins, H. Fonseca, C. Calaza, J. Gaspar, G. Shalev. Nano Energy, 70, 104521(2020). **IF=17.881**

- Opportunities for enhanced omnidirectional broadband absorption of the solar radiation using deep sub-wave length structures. A. Prajapati, J. Llobet, M. Antunes, S. Martins, H. Fonseca, C.Calaza, J. Gaspar, G. Shalev. Nano Energy, 70,104553 (2020). **IF=17.881**
- Automated characterization and analysis of fabricated large arrays of nanostructures on large area wafers. J. Llobet, M. Martins, C. Calaza, M. Antunes, S. Martins, H. Fonseca, B. Pires, J. Gaspar. Precision Engineering, 60, 320-325 (2019). **IF = 3.156**

- Studies of Electromigration Effect in RDL of Wafer-Level Fan-In and Fan-Out Packaging Using a Novel Analysis Approach. A. Cardoso, S. Martins, A. Gouvea. IMAPS 6th Micro/Nano-Electronics packaging and Assembly ,Forum (MiNaPAD), May 2018, Grenoble

- Characterization of Electromigration Effects in RDL of Wafer Level Fan-In and Fan-Out Packaging Using a Novel Analysis Approach. A. Cardoso, S. Martins, A. Gouvea, IEEE 8th Electronic System-Integration Technology Conference (ESTC), September 2018, Dresden.

SOFIA MARTINS
MICRO & NANOTECH ENGINEER

Phone: +34 673811284 | **E-mail**: csg.martins12@gmail.com | **Skype**: cgs.martins12 |
LinkedIn: /in/sofia-martins-1602 | **Address**: Barcelona, Spain | **ORCID**: 0000-0002-1801-1651

Conferences

-**Enhancing magneto-ionic effects in Co oxide films by electrolyte enginering.** S.Martins, Z. Ma, X.S.-Monfort, M. Sodupe, L. Santiago, E. Menéndez, E. Pellicer, Jordi Sort. International Colloquium on Magnetic Films and Surfaces (ICMFS-2022). (Virtual Poster)

-**Dynamic electric-field-induced magnetic effects in cobalt oxide thin films: towards magneto-ionc synapses.** S. Martins, J. de Rojas, Z. Tan, M. Cialone, A. Lopeandia, J. H. -Martín, J. L. Costa-Krämer, E. Menéndez, J. Sort. MMM-Intermag Conference 2022 (Oral Presentation)

-**Thickness dependence of magneto-ionic effects in Co3O4 films.** S. Martins, J. Salgueiro, J. de Rojas, J. C.-Krame, E. Menéndez, J. Sort. Joint European Magnetism Symposia conference(JEMS) 2020, (Virtual Oral Presentation)

- **Fabrication of decorated nanopillar arrays for silicon light trapping enhancement in solar cell applications.**
J Llobet, C Calaza, M Antunes, H Fonseca, S Martins, Y Faingold, S Fadida, A Prajapati, G Shalev and J Gaspar. Micro Nano Engineering (MNE) International Conference, 2019, Greece (Poster)

- **Optimizing a Silicon Etching Process for High Density Light Funnel Arrays.** S. Martins, C. Calaza, J.Lobet, H. Fonseca, M. Antunes, G. Shalev, J. Gaspar. Plasma Etch and Strip in Microtechnology 2019 (PESM 2019), May 2019, Grenoble (Oral Presentation)